博士論文

Ab initio theoretical study of high-harmonic generation from transition metal elements

(第一原理計算による遷移金属元素からの
高次高調波発生の理論的研究)

ワーユータマ　イマム　セティアワン
Wahyutama Imam Setiawan

Abstract

High-harmonic generation (HHG) from transition elements which often exhibits resonance phenomena is addressed in this dissertation from theoretical point of view. Using two methods which are especially devised to tackle time-dependent many-electron quantum processes, namely time-dependent complete active space (TD-CASSCF) and time-dependent occupation restricted multiple active space (TD-ORMAS), we perform theoretical studies on the strong-field response of manganese, indium, and chromium isolated atoms and some of their cations to simulate HHG from the plasma of each of these elements. The experimentally well-known enhancement of the harmonic peak around ~ 50 eV in Mn plasma, ~ 20 eV in In plasma, and ~ 44 eV in Cr plasma are faithfully reproduced in our simulations where the intensity enhancement can reach up to two orders of magnitude compared to the neighboring harmonics in neutral Mn. A portion of the subsequent analyses, based on orbital-resolved dynamics such as orbital transition and population, is devoted to find a conclusive answer as to what drives this enhancement phenomena.

The enhancement disappears when electrons are prevented from leaving $3p$ orbitals

The ground state electronic configurations are $1s^2 2s^2 2p^6 3s^2\ 3p^6 4s^k 3d^5$ where $k = 2, 1, 0$ for Mn, Mn^+, and Mn^{2+}, respectively. Making use of TD-CASSCF's capability to freeze some orbitals, our first orbital-based study finds that when the first five orbitals (i.e. from $1s^2$ to $3p^6$) are frozen, the 50 eV enhancement disappears. On the other hand, when the frozen orbitals are below and do not include $3p$ orbitals, the enhancement is present and the overall HH spectra have a reasonably good agreement. This is a strong hint that $3p$ orbitals must be involved in the 50 eV enhancement mechanism. The same analysis is also performed for indium plasma whose configurations are $1s^2 2s^2 2p^6 3s^2\ 3p^6 3d^{10} 4s^2 4p^6 4d^{10} 5s^2 5p^k$ where $k = 1, 0$ for In and In^+,respectively. It was found that in this case when $4d$ are frozen, the enhancement disappears. The time-frequency spectrograms calculated through Gabor-transform indicate that the onset of this enhancement occurs when the continuum electron wavepacket has return energy close to the resonant one, and then they populate some upper orbitals instead of going back to their initial one along with the emission of a photon. The relaxation from this highly populated, unknown upper orbital is accompanied by the emission of the enhanced radiation.

A successful indentification of the resonantly coupled transitions with the laser field

The next analysis is based on dipole interactions coupling the different ground state orbitals, that is, the orbital-orbital transitions. The mathematical ground of this analysis is derived from the equation for time-dependent acceleration, a quantity whose power spectrum is understood to be the HH spectrum. In this equation, the total acceleration may be written as a superposition of a particular quantity that depends on a pair of orbitals and time. This quantity also vanishes if the pair of orbitals it depends on do not obey the usual dipole selection rules. Therefore, the orbital-orbital transition contribution to the total HH spectrum may be quantified with this quantity. Running the simulations, we identify the $3p \leftrightarrow 3d$ transitions to be the dominant driving mechanism of the enhancement in Mn and Mn^+ at ~ 50 eV and in Cr and Cr^+ at ~ 45 eV.

Whereas for In and In^+, these transitions are the $4d - 5p$ transitions which are responsible for the $\sim$ 23 eV enhancement. Coherently superposing the components of these transitions reveals the constructive nature of the ensuing interference which prompts further increase of the harmonic intensity at the resonant energy. Keeping in mind the preceding result from the time-frequency spectrogram, it may be concluded that the upper state which receives considerable population responsible for the enhanced emission is a state where an electron is excited from $3p$ to $3d$ orbitals in Mn and Cr plasma. For In plasma, this upper state is where an electron has been excited from $4d$ to $5p$ orbitals.

Population exchange between the resonant orbital pair

In our last study, we investigate the signature of resonant enhancement in HHG imprinted in the orbital population from which we find that in Mn plasma, the time-dependent populations of $3p$ and $3d$ orbitals are modulated at the resonant energy 50 eV and that these modulations are out of phase, meaning, in time domain as there is a peak in either orbital populations, at the same time there will be a valley in the population of the other orbital. To put it differently, while the atom is emitting the enhanced radiation as a result of an interaction with the strong laser, an alternating exchange of population between the two orbitals responsible for the enhanced emission is at work in the background. The absence of 50 eV modulation in the total population of virtual orbitals (as can be seen from the Fourier transform of the population) is indicative that the final mechanism leading to the enhanced 50 eV emission involves only bound-bound electron dynamics. We believe this finding is remarkable because, as opposed to ordinary HHG where there is efectively only one essential discrete state (the ground state), resonant HHG shows that the internal core structure of an atom can bear a dramatic change in the feature of the HH spectrum.

Table of Contents

Chapter 1

Introduction

Light-matter interaction is undeniably an important subject of physics that underlies many scientific as well as technological breakthroughs. Since the discovery of photons by Albert Einstein, science has seen major discoveries in this subject - the invention of laser, optical tweezer, synchrotron radiation, and quantum information, to name a few. A new direction of research was opened up when a technique called *chirped pulse amplification* (CPA) was invented by which one can realize generation of ultrashort laser pulses with unprecedented level of intensity [1–3]. With this technique, laser pulses having intensity above 10^{16} W/cm^2 can be routinely produced (check, for example, the European Extreme Light Infrastructure (ELI) [4–8]) . This intensity regime is often referred to as relativistic intensities because above 10^{16} W/cm^2, electrons begin to move at relativistic velocity. Below this range, when the intensity lies in the range 10^{13} – 10^{15} W/cm^2, the interaction is said to be in the strong-field regime within which all electromagnetic processes behave extremely nonlinearly - hundreds multiple of the input laser frequency have been observed at the output - while the relativistic effects are still negligible. High-harmonic generation (HHG), the key topic of the present work, is one example of laser-matter interaction taking place within strong-field intensity regime.

1.1 High-Harmonic Generation

When an intense laser field interacts with matter, one of the possible outcomes is the emission of a secondary radiation whose frequencies are multiples of the the primary radiation frequency. This electromagnetic process, which is referred to as high-harmonic generation (HHG), is in fact the most important outcomes of a strong-field interaction. Compared to the other common strong-field processes such as multiphoton ionization (MPI), tunneling-ionization, and non-sequential double ionization (NSDI), HHG is the closest to practical applications, whether for fundamental researches or commercial products. This fact is not without reason, until today HHG is the only table-top alternative to coherent XUV light sources such as synchrotron facilities [9–11] offering quantum-scale temporal resolution. For this reason, increasing HH pulse energy is still an active research topic that has seen numerous developments in the generation technique, see e.g. Ref. [12–15].

HHG made its first appearance in a laboratory in 1987 when McPherson et al. [16] used an intense 248 nm radiation from an excimer laser to irradiate Ne, Ar, Kr, and Xe gases, and they observed that secondary radiations with wavelength as short as 14.6 nm (17-th harmonic of the excimer used) were generated. One of the well-known features of any high-harmonic (HH) spectra is the decrease in harmonic intensity for the first few orders, which is followed by the so-called *plateau* region spanning over an energy range in which the harmonic intensities stay relatively constant (see Fig. 1.1(a)). The extent of plateau region depends on the laser intensity and wavelength. At the cutoff energy (Fig. 1.1), which marks the end of plateau region, the harmonic intensity decreases again down to the noise level.

HHG is classified as an extreme nonlinear process because it involves generation of harmonics up to tens (Fig. 1.1(b)) [17], and sometimes hundreds (Fig. 1.1(c)) [18], multiple of the fundamental frequency depending on the laser intensity, wavelength, and atomic species [19–25]. The fact that

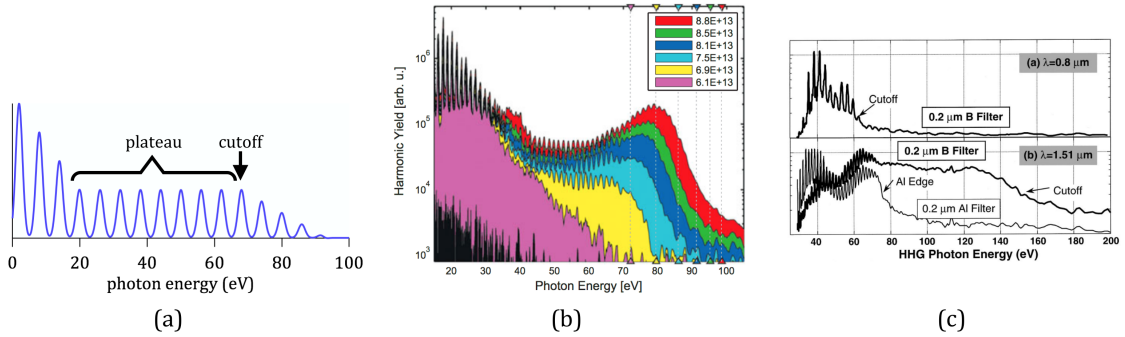

Figure 1.1: (a) HHG spectrum typically consists of a rapidly decreasing low order peaks, followed by plateau region that ends around the cutoff energy. (b) Experimental HHG spectra from Xe gas measured at different laser intensities. Figure adapted from [Shiner, Trallero-Herrero, Kajumba, Schmidt, Bertrand, Kim, Bandulet, Comtois, Kieffer, Rayner, Corkum, Légaré, and Villeneuve, *J. Mod. Optic.* **60**, 1458 (2013)]. (c) Experimental HHG spectra from Ar gas demonstrating significantly high cutoff energy when long wavelength laser is used. Reprinted figure with permission from [B. Shan and Z. Chang, "Dramatic extension of the high-order harmonic cutoff by using a long-wavelength driving field", *Phys. Rev. A* **65**, 011804 (2001)]. Copyright 2001 by the American Physical Society. The lower energy part of the spectra have been filtered which is often done in experiment.

even a few hundreds of harmonic can be reached asserts that conventional nonlinear optics description will not suffice in explaining the phenomenon. To give numerical figures, the ionization energy of Ar gases from which HHG is usually generated is about 15.8 eV, hence for a driving laser at 800 nm there could only be about 10 photons absorbed to make the first ionization happen, implying that the harmonic train in the spectrum should terminate at around the tenth order, instead of more than a hundred as reported in Ref. [18]. These observations strongly suggest that we need to set aside the perturbative nonlinear optics theory and devise a new model.

A semi-classical model was proposed in the early 90's in an attempt to phenomenologically explain HHG [26–28]. This model is referred to as the *three-step model*, or sometimes *simple man model*, because the key idea describes the HH emission as an outcome of three chronological events. Fig. 1.2 provides a visualization of the model. In the first step (Fig. 1.2(a)), an electron is tunnel-ionized by the electric field of the intense laser through a barrier formed by the atomic core's potential and laser's potential. In the second step (Fig. 1.2(b)), the ionized electron emerges in the continuum and is then driven by the laser electric field. During its excursion in the continuum, the driven electron will acquire some kinetic energy from the field. Depending on the time when the first step took place, this electron may or may not come back to the atomic core. The former possibility then leads to the last step (Fig. 1.2(c)) in which this electron recombines to the initial state while emitting a photon whose energy is equal to the sum between the kinetic energy acquired in the second step and the atom's ionization potential.

Within the three-step description, an attempt to estimate the HH cutoff energy has been formulated using Newtonian mechanic [29]. In this classical approach, one starts from Newton's second law of motion for an electron in a sinusoidal electric field $E(t) = E_0 \cos \omega t$ (which can be

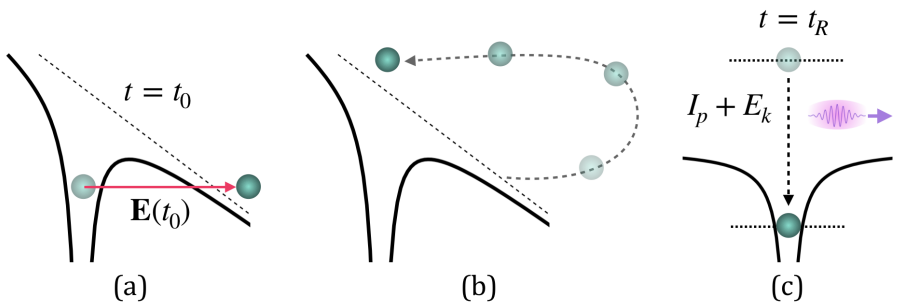

Figure 1.2: (a) The first step consists of tunnel-ionization through a potential barrier. (b) In the second step, the ionized electron undergoes excursion in continuum driven by the laser field. (c) In the last step, this electron recombines to the ground state emitting a HH photon.

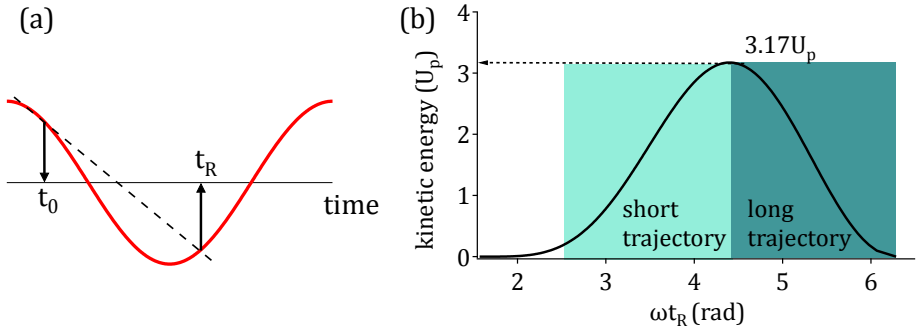

Figure 1.3: (a) Graphical method to calculate return time t_R for a given ionization time t_0. (b) Return kinetic energy curve where for each kinetic energy value, one has two contributing trajectories, long and short ones.

assumed to be z-polarized) that starts the motion at time $t = t_0$ with zero initial velocity from the origin. Integrating this equation twice, one obtains the equation for displacement. The last step, i.e. the moment of return, happens when the displacement equals zero again. Substituting this value into the equation for displacement, one arrives at

$$\cos \omega t_R = \cos \omega t_0 - (t_R - t_0)\omega \sin \omega t_0, \tag{1.1}$$

where ω is the laser angular frequency, t_0 is the ionization time (i.e. the instance when the first step takes place), and t_R is the return time (the time of the last step). Eq. (1.1) tells us that the return time t_R can be calculated at the intersection between the oscillating electric field and a line that is tangent to the field at time $t = t_0$, graphically depicted in Fig. 1.3(a). Knowing the value of t_R for each t_0, it is then possible to calculate the kinetic energy at the time of return, the sum of which with ionization potential will give the emitted photon energy. A typical plot of $E_k(t_R)$ is shown in Fig. 1.3(b) with the vertical axis in unit of *ponderomotive energy* U_p,

$$U_p = \frac{E_0^2}{4\omega^2} \tag{1.2}$$

and the horizontal axis is the return phase. In Eq. (1.2), we have adopted atomic units where $m = \hbar = e = 4\pi\epsilon_0 = 1$. Unless otherwise noted, atomic units prevail throughout this dissertation. Shifting this kinetic energy curve up by the atoms's ionization potential gives us the emitted photon energy within plateau region, that is, the vertical range of this curve predicts the extend of plateau region. The maximum kinetic energy $3.17U_p$, occurring at about $\omega t_R = 4.4$ rad, then corresponds to the harmonic cutoff, hence we have the semi-classical estimate of HH cutoff energy to be

$$E_c = I_p + 3.17U_p. \tag{1.3}$$

Although Eq. (1.3) was derived based on classical mechanical analysis, it actually gives a reasonably accurate estimate of experimental cutoff energies. Throughout this dissertation, Eq. (1.3) will actively be invoked in various analyses such as in deducing which ionic species are present in the simulation as a result of strong-field interaction. From Fig. 1.3(b), one also sees that for each return kinetic energy, the emitted photon energy contains contributions from electrons having short and long trajectories during the continuum excursion. The radiations emitted by these short and long trajectory electrons having the same kinetic energy interfere to give harmonic peaks in the plateau region (see Fig. 1.1.)

Atoms, molecules, as well as solids have been experimentally shown to be able to act as the source medium for such highly nonlinear process. The nature of the generation process of HH radiation that is closely intertwined with electron dynamics inside the generating medium is often exploited by physicists to study those dynamics. In fact a number of quantum scale phenomena have been succesfully identified by devising specialized measurement techniques such as electronic structure detection [30], observation of Rabi flopping [31], multi-channel interference [32], spectroscopy of Cooper minimum [33, 34] and many others.

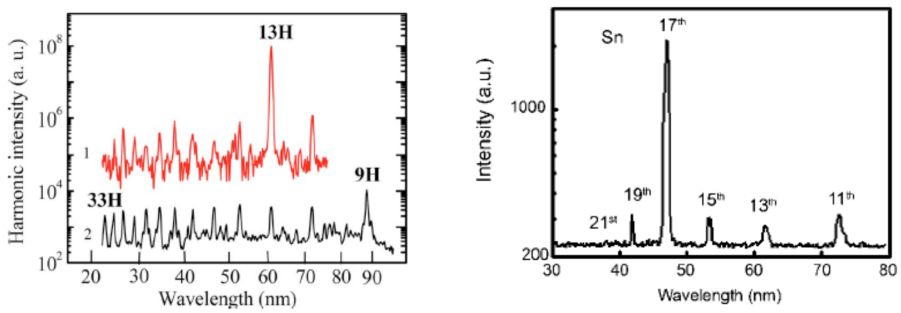

(a) (b)

Figure 1.4: (a) HH spectra from In (red) and Ag (black) plasmas. Figure adapted with permission from Ref. [35], [Optical Society of America] (b) HH spectrum from Sn plasma. Figure adapted from Ref. [36], [Optical Society of America].

1.2 High-Harmonic Generation from Plasma Plumes

The most frequently used atomic elements to generate high harmonic radiations are rare gas atoms. Rare gas atoms are favorable for at least two reasons. First, they are readily available in gas phase and second, their inert nature makes them easy to store which otherwise requires special care to prevent them from reacting with the surrounding substances. Other stable elements occuring naturally in gas phase like nitrogen is also used as HH source thanks to its high ionization potential, ~ 14.5 eV.

In 2006, however, a group of researchers had a different idea in what they should use as the HH source [35] - instead of rare gas, they created plasma plumes through laser ablation on a metallic surface. The primary observation is that, using a 796 nm laser whose intensity is on the order of 10^{14} W/cm^2 to generate HH from indium (Z = 49) plasma, they discovered that the HH spectrum exhibited a strong enhancement of the 13-th harmonic (20.3 eV) of the fundamental laser (see the red line in Fig. 1.4(a)). This peak is enhanced more than hundred times stronger than the neighboring ones. Following this discovery, a pursuit of metallic elements to act as the plasma source that is able to produce similar enhancement phenomena began.

In Ref. [36], tin (Z = 50) plasma was used as the source and a 20× enhancement of the 17-th harmonic (26.5 eV) of a 795 nm and 1×10^{14} W/cm^2 laser was observed (Fig. 1.4(b)). In 2007, Ganeev et al. [37] observed an enhancement in the HH spectrum from Cr plasma following an irradiation of a Cr containing metal by an intense laser at 800 nm center wavelength. The enhancement occurs for the 29-th order of the fundamental, which is about 45.1 eV [37]. Fig. 1.5(a) shows the harmonic spectrum from this experiment. Then in 2012, using 800 nm center wavelength Ti:sapphire laser with intensity of about 6×10^{14} W/cm^2, Ganeev et al. [38] were able to generate an enhanced harmonic at ~ 50 eV (the 31-st harmonic order of the fundamental), the spectrum is shown in Fig. 1.5(b). The other metallic elements such as Cr, Mn, and Sb have also been used as the HH source resulting in the observations of enhancement at 45.4, 50, and 32.6 eV respectively [37–41]. It is worth noting that these elements all have loosely bound unpaired electrons. The properties of the enhanced harmonics from several plasma metals are compiled in Table 1.1 extracted from published sources. It is worth noting that while enhancement of a range of harmonics is known to be a signature of HH spectrum from Xe [42], never was in rare gas HH spectra an enhancement of a single harmonic similar to those in transition metal plasma observed. This might be related to the fact that in rare gas elements all orbitals are fully occupied.

The typical experimental setup for generating HH radiation from a metallic plasma relies on

Table 1.1: The enhanced energy and the largest reported enhancement for In, Sn, Sb, Cr, and Mn plasma HHG.

	In [35]	Sn [36]	Sb [37]	Cr [37]	Mn [38]
Enhanced energy (eV)	20.3	26.5	32.6	45.4	50.0
Largest enhancement (× neighbors)	200	20	20	23	> 10

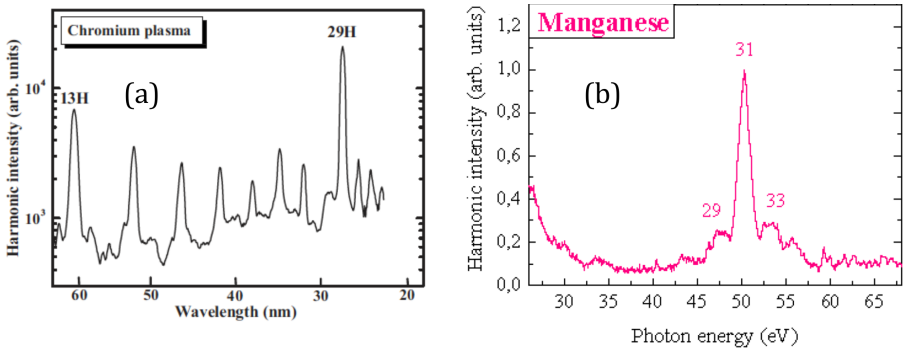

Figure 1.5: HH spectra from (a) Cr plasma (Reprinted figure with permission from [R. A. Ganeev, L. B. E. Bom, J.-C. Kieffer, and T. Ozaki, "Systematic investigation of resonance-induced single-harmonic enhancement in the extreme-ultraviolet range", *Phys. Rev. A* **75**, 063806 (2007)]. Copyright 2007 by the American Physical Society) and (b) Mn plasma (adapted with permission from Ref. [38], [Optical Society of America]) wavelength lasers. The 29-th harmonic in the former and the 31st harmonic in the latter are clearly enhanced.

a technique called dual laser plasma technique [43] employing two pulsed lasers. The first laser, typically having intensity on the order of 10^9 – 10^{10} W/cm^2, impinges on the metallic surface to induce ablation and produce plasma plumes. The second laser, of intensity in the strong-field regime (10^{13} – 10^{15} W/cm^2), then comes at a delay and, upon focusing, irradiates the nascent plasma to generate the HH photons.

1.3 The Objective of The Study

The origin of harmonic enhancement in HH spectra from non-conventional elements mentioned in the previous section has been linked to a resonant process where a giant transition line in the excitation spectrum of the plasma element is in resonant (having close energies) with the enhanced harmonic peak [35, 44]. While the association of a distinctly large peak in the frequency response of a system with a natural frequency in that system is ubiquitous in physics, such as resonance in RLC circuit, in forced pendulum, and in laser's optical cavity, given the complicated nature of multielectron systems, it is difficult to assert whether resonance is really the driving mechanism behind this harmonic enhancement before a proper theoretical account is given. Even if so, there are still open questions as to which transition line is actually responsible for the resonance (different transitions lying very close to each other exist in Mn^+), which ionic species is the dominant source of enhancement, and ultimately, how this transition line manifests its presence in the high-harmonic spectrum, which is a highly nonlinear process. Aimed at answering these questions, in this work we attempt to approach the problems by means of theoretical methods that take into account all electrons present in the atom and solve the time-dependent wavefunction right from the exact Schrödinger equation. The goals of this research are, therefore, (1) to reproduce the experimentally observed resonant enhancement in HHG and (2) to unveil the underlying physical mechanism of this enhancement phenomena.

1.4 Theoretical Approach to High-Harmonic Generation

It comes to be known that the three-step model discussed in Section 1.1 predicts the extent of plateau region with a good qualitative accuracy. This model, however, has nothing to do with the intensity of each harmonic peak and thus a quantum mechanical calculation is necessary to get the correct trend of HH spectrum. One of the early, full quantum mechanical calculations on HHG was performed by Lewenstein et al. [23, 45]. In this method, the wavefunction is assumed to be a superposition of the ground state and many continuum states, with the latter being approximated with Volkov states. Volkov state is an eigenfunction of a free-electron in a laser field. Since atomic core is neglected in calculating Volkov states, this model describes the system as if the laser field is too strong for the core's potential to be considered and hence is often called *strong-field approximation* (SFA) method. A multielectron extension of SFA method was proposed by Smirnova et al. [29, 46] where the multielectron effects on the harmonic emission are

described as an interference of individual three-step processes from multiple ionization channels. A given ionization channel is characterized by a particular final state of the remaining ion after ionization, for example the removal of an electron may leave the ion in its ground state or in one of its excited states, each of which is associated to a different channel [46]. This multichannel method approximates the continuum state with Volkov state too.

Prior to the present work, there have been a number of theoretical efforts on the subject of resonant HHG over the past decade. Milošević in Ref. [47] and [48] studied the effect of coherent superposition in the initial state and found that a three-step process starting from an excited state but returning to the ground one exhibits an enhanced harmonic. In Ref. [49], the line shape of resonant harmonic is discussed in terms of Fano lineshape. A modelling of the autoionizing state which is known to be responsible in most cases for the enhancement is performed in Ref. [50] and [51] using a parametrized potential with barrier. Other reports of varying elaboration have also been published, see e. g. Ref. [52–54]. Most of the above-mentioned attempts use effective-potential-kind-of approach in performing the analysis, that is, these methods are effectively of single active electron type. Consequently, multielectron dynamics, which could possibly hold the important information about the actual driving mechanism, are automatically out of the picture. A few works that take into account multielectron effects are reported in Ref. [55] and Ref. [56]. In Ref. [55], Redkin and Ganeev simulated a fullerene-like model system using MCTDHF method [57, 58] by having only two active electrons, hence making the deeper aspects of the mechanism remain unexplored. While in Ref. [56], Pabst and Santra apply *time-dependent configuration interaction singles* (TDCIS) [59] to study an enhancement around 100 eV in the HH spectrum of Xe. The target system considered in these works, however, is a closed-shell atom where the dynamics of the valence electrons are substantially different from the unpaired electrons in transition metal atoms.

The problem at hand, however, demands a method which can properly treat more than one electron at once during an interaction with laser field because transition elements generally possess multiple loosely bound electrons (typical ionization potential for transition metals is $\sim$ 6 eV). It is also for this reason, other seemingly suitable method, *time-dependent density functional theory* (TDDFT), may actually not be quite so because of the lack of accuracy of this method in calculating ground state wavefunction of transition metals. As will also be discussed later in Chapter 4, in one of the analyses we will look at the different transition contributions to HH spectrum where the off-diagonal matrix elements of density matrix are invoked, something which are not available in TDDFT as it optimizes only the diagonal elements.

In order to enable a direct comparison with experiments and with the deeper understanding of the mechanism underlying resonant HHG, an *ab initio* simulation of realistic three-dimensional (3D) atoms is therefore indispensable. A promising class of methods to investigate intense laser-driven multielectron dynamics in such systems is the *time-dependent multiconfiguration self-consistent-field* (TD-MCSCF) method [60–62], which describes the system wavefunction by a superposition of Slater determinants consisting of time-dependent spin-orbital functions. TD-MCSCF is a general denomination for first-principles methods where the time-dependent orbitals and CI coefficients are obtained variationally. Extensions of TD-MCSCF to allow more freedom in the specification orbital occupations include *time-dependent complete active space self-consistent field* (TD-CASSCF) [63, 64], *time-dependent occupation restricted multiple active space* (TD-ORMAS) [65], and *time-dependent restricted active space self-consistent field* (TD-RASSCF) [66]. The first two methods, TD-CASSCF and TD-ORMAS, are the methods employed in this dissertation. Previously, TD-CASSCF and TD-ORMAS methods have only been applied to either closed-shell systems or systems having a single unpaired electron [64, 65, 67, 68]. In the present work, these methods are extended to enable calculations of general open-shell atoms such as transition metals, having a number of of unpaired valence electrons which can equally participate in the dynamics under a strong laser field. Some of the systems that will be considered in this work, Mn and Cr, as well as their low-charged cations, have 5 or 6 unpaired electrons.

In performing the analysis, we take full advantage of TD-CASSCF and TD-ORMAS as a multiorbital method by studying the dynamics emerging in and between these orbitals [69]. The use of orbital functions for describing the wavefunction of multielectron systems has long been very popular within atomic and molecular physics community. Based on this fact, the analyses employed in this dissertation are set up by emphasizing the response of these orbitals to a laser field with the aim to reveal the physics underpinning resonant HHG in a conventional and straightforward way. As it turns out, our analysis is also able to probe more general strong-field properties such as ionic cutoff position and ionization dynamics.

1.5 Organization of This Dissertation

The rest of this dissertation is organized as follows. In Chapter 2, a review of some of the existing theoretical methods on the subject of resonant HHG is presented. In Chapter 3, the mathematical background of the methods employed in this dissertation, TD-CASSCF and TD-ORMAS, will be discussed. The first result of our study is presented in Chapter 4 where in-depth analyses of resonant HHG from Mn and its cations are performed within the framework of TD-MCSCF method and the answers of important questions about the enhancement mechanism are discussed. Chapter 5 provides results from different types of plasma elements, indium and chromium, and serves as a universality check of the main finding in Chapter 4. The conclusion of the works presented here, given in Chapter 6, brings together all of the key findings in order to construct a general picture of the mechanism behind resonant HHG. Here the future prospects and the impact of the study are also discussed.

Chapter 2

Review of The Existing Studies

Resonant enhancement in HHG is an intriguing phenomena. The quantum mechanical view of HHG was well understood to be a single active electron process for the most part. For instance, SFA stipulates that the predominantly contributing states in HHG are the ground state and continuum states, which are needed to form the continuum wavepacket [29]. The neglect of the other discrete states comes as no surprise since SFA is build upon the phenomenological three-step model. Resonant HHG, however, suggests that there exist another state which is as important as the ground state and this state is most likely not a continuum state as it needs to have a notable overlap with the ground state, otherwise the enhancement will not occur. Various theoretical models which attempt to explain the origin of resonant enhancement in HHG have been proposed throughout the years. In the present chapter, the review of some of these models are presented by emphasizing the key features and the underlying assumptions.

2.1 HHG from superposition of states

In the usual three-step model, the first step comprises a tunnelling event of an electron starting from the ground state. Taking a step further, the model to be discussed proposes that the resonant enhancement is a result of three-step process starting from a superposition of states, instead of just one [47]. According to this model, if the initial state consists of a coherent superposition between ground state and an excited state lying at ΔE above the ground state where ΔE takes the value of the enhanced energy, then the HH spectrum will exhibit strong peaks around the ΔE. In order for this enhancement to occur, the laser frequency ω must be such that one of its odd harmonics be coincident with ΔE, i.e. $\Delta E = (2n_R + 1)\omega$ for some integer n_R.

Graphically, the idea of HHG from superposition of states is depicted in Fig. 2.1. According to this model at first, the HHG process is of the single state type. Then as the atom interacts with an increasingly strong laser field, provided the laser frequency satisfy $\Delta E = (2n_R + 1)\omega$, the second state lying at ΔE above the ground (first) state can be populated by the matching harmonic order $2n_R + 1$. From this point on, the subsequent three-step processes will start from a superposition of the ground and excited states. When the ionized electron returns to the core it will go back to the ground state. In Ref. [47], this process is mathematically described using Lewenstein model [23], which is built upon single active electron (SAE) approximation. Therefore, the wavefunction $\Psi(t)$ is a solution of one-electron time-dependent Schrödinger equation

$$i\frac{\partial}{\partial t}\Psi(t) = \left(-\frac{1}{2}\nabla^2 + z\mathscr{E}(t) + V(\mathbf{r})\right)\Psi(t)$$

where $\mathscr{E}(t)$ is the laser field and $V(\mathbf{r})$ is the effective core potential. Provided we know the state of the system in the beginning which for HHG, is often taken to be the ground state $|g\rangle$, the above

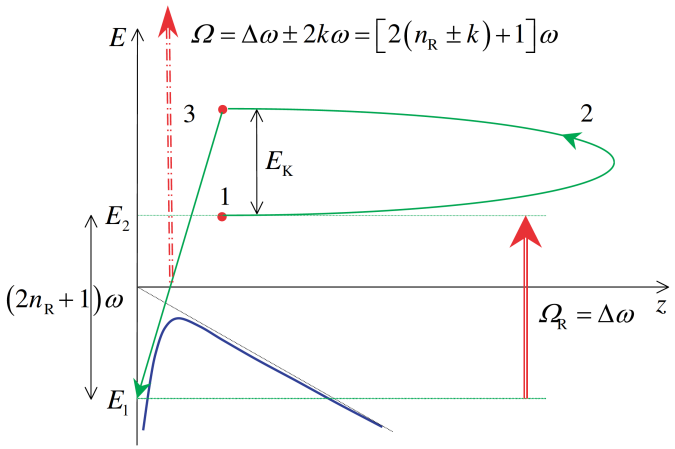

Figure 2.1: In superposition of state model of resonant HHG, the first step consists of an ionization from an excited state. In the second step, the ionized electron is driven in continuum by the field. In the last step, this electron recombines to the ground state by emitting a photon of energy $\Omega = \Delta\omega \pm (2k+1)\omega$. Figure adapted from [Milošević, *J. Phys. B* **40**, 3367 (2007)].

Schrödinger equation can be cast into integral form [29],

$$\begin{aligned} |\Psi(t)\rangle &= -i \int_0^t \mathrm{d}t'\, \hat{U}(t,t')\hat{V}_L(t')U_0(t',0)\,|g\rangle + \hat{U}_0(t,0)\,|g\rangle \\ &\approx -i \int_0^t \mathrm{d}t'\, \hat{U}_V(t,t')\hat{V}_L(t')U_0(t',0)\,|g\rangle + \hat{U}_0(t,0)\,|g\rangle \end{aligned} \tag{2.1}$$

where $V_L = z\mathscr{E}(t)$ the dipole interaction term and $\hat{U}$ and $\hat{U}_0$ are propagators associated with Hamiltonians with and without external field, respectively. The approximate sign is attributed to the replacement $\hat{U} \to \hat{U}_V$ and corresponds to the so-called *strong-field approximation* (refer to Section 1.4). $\hat{U}_V$ is the evolution operator associated with Volkov Hamiltonian, which describes an electron in an external field but without Coulomb potential. With this form of wavefunction, following the steps prescribed by Lewenstein et al. [23, 29, Chap. 7], the expectation value of dipole operator (or in short, time-dependent dipole moment) reads

Dipole moment in Lewenstein model of HHG

$$\begin{aligned} d(t) &= \langle\Psi(t)|\mathbf{r}|\Psi(t)\rangle \\ &= -i \int_0^t \mathrm{d}t' \int \mathrm{d}^3\mathbf{k}\, d_g^*(\mathbf{k} + \hat{\mathbf{z}}\mathscr{A}(t))\, d_g(\mathbf{k} + \hat{\mathbf{z}}\mathscr{A}(t'))\mathscr{E}(t') \exp(iS(\mathbf{k},t,t')) + \text{c.c.} \end{aligned} \tag{2.2}$$

where $\mathscr{E}(t) = -\,\mathrm{d}\mathscr{A}(t)/\mathrm{d}t$,

$$\begin{aligned} S(\mathbf{k},t,t') &= \int_t^{t'} \mathrm{d}\tau \left(\frac{1}{2}(\mathbf{k} + \hat{\mathbf{z}}\mathscr{A}(\tau))^2 + I_p\right), \\ d_j(\mathbf{k}) &= \langle\mathbf{k}|\mathbf{r}|j\rangle, \end{aligned}$$

and $|\mathbf{k}\rangle$ momentum eigenvector. $S(\mathbf{k},t,t')$ reflects the phase accumulated by the electron undergoing excursion in continuum. It contains the kinetic energy of that electron plus ionization potential which will be converted to the energy of high-harmonic photon. The HH spectrum is then calculated to be

$$\mathscr{P}_{\mathrm{HH}}(\omega) = \omega^4 |\tilde{d}(\omega)|^2$$

with $\tilde{d}(\omega)$ being the Fourier transform of $d(t)$,

$$\tilde{d}(\omega) = \int \mathrm{d}t\, d(t) e^{i\omega t} \tag{2.3}$$

and $d(t) = \langle\Psi|z|\Psi\rangle$ is the dipole moment of the system.

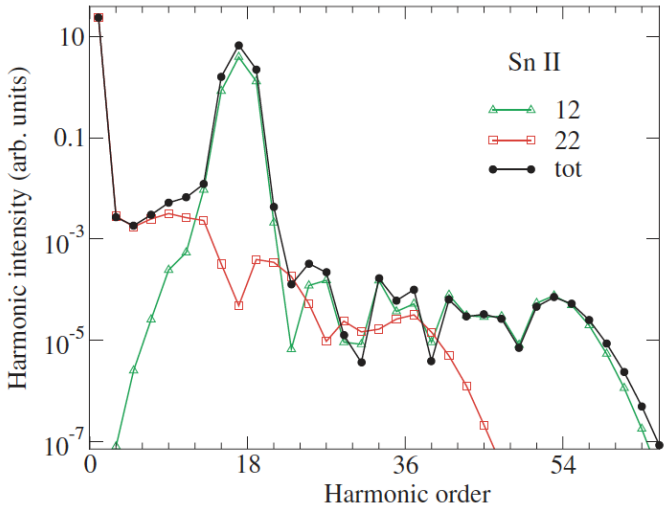

Figure 2.2: The HH intensities corresponding to $|d_{eg}(\omega)|^2$ (green), $|d_{ee}(\omega)|^2$ (red), and $|d(\omega)|^2$ (black). Figure adapted from [Milošević, *J. Phys. B* **40**, 3367 (2007)].

Eq. (2.2) applies for HH process starting from ground state only. If we instead require that the initial state be a superposition between the ground $|g\rangle$ and some excited state $|e\rangle$, it can then be shown, after making the substitution $|g\rangle \to c_g |g\rangle + c_e |e\rangle$ in Eq. (2.1) and following the same procedure that leads to Eq. (2.2) and using Eq. (2.3), that the dipole spectrum takes the form

$$\tilde{d}(\omega) = c_g^2 \tilde{d}_{gg}(\omega) + c_e^2 \tilde{d}_{ee}(\omega) + c_g c_e \left(\tilde{d}_{eg}(\omega) + \tilde{d}_{ge}(\omega)\right) + \tilde{d}_B(\omega)$$

with

$$\begin{aligned}
\tilde{d}_{ij}(\omega) &= \int \mathrm{d}t \, (d_{ij}(t) + d_{ji}(t)) e^{i\omega t}, \\
d_{ij}(t) &= -i \int_0^t \mathrm{d}t' \int \mathrm{d}^3\mathbf{k} \, d_i^*(\mathbf{k} + \hat{\mathbf{z}}\mathcal{A}(t)) \, d_j(\mathbf{k} + \hat{\mathbf{z}}\mathcal{A}(t')) \mathcal{E}(t') \exp\left(iS_{ij}(\mathbf{k}, t, t')\right), \\
S_{ij}(\mathbf{k}, t, t') &= \int \mathrm{d}\tau \, \frac{1}{2} (\mathbf{k} + \hat{\mathbf{z}}\mathcal{A}(\tau))^2 + E_i t - E_j t', \\
d_B(\omega) &= \int \mathrm{d}t \, d_B(t) e^{i\omega t} \\
&= 2 \int \mathrm{d}t \, \mathrm{Re}\left\{ a_g^* a_e \langle g|z|e\rangle \, e^{-i(E_e - E_g)t} \right\} e^{i\omega t}.
\end{aligned}$$

The term $\tilde{d}_B(\omega)$ is nonzero only if $|g\rangle$ and $|e\rangle$ have the same parity. Numerical simulations show that the HH spectrum resulting from superposition of states is dominated by the cross term $\tilde{d}_{eg}(\omega)$ [48].

Applying the preceding analysis on Sn^+, whose HHG spectrum is experimentally found to have an enhanced peak at 26.27 eV [44, 70], the spectra shown in Fig. 2.2 results. This simulation is obtained using laser intensity of 4×10^{14} W/cm^2, wavelength of 802 nm and $c_e = c_g = 1/\sqrt{2}$. The total spectrum (black) clearly exhibits several enhanced peaks around the 18-th harmonic. The figure also shows the parts contributed by $\tilde{d}_{ee}(\omega)$ (red) and by $\tilde{d}_{eg}(\omega)$ (green) where it is seen that the latter is responsible for the enhancement as well as for the cutoff position. This observation is interpreted in the following way. During the early portion of the laser where the field amplitude is low, single state HHG is the dominant process. As the field becomes stronger, the kinetic energy of the continuum electron also rises up and at some point the recombination energy (kinetic energy plus ionization potential) reaches the resonant energy ΔE and excite the state $|e\rangle$. Then due to the strong transition amplitude between $|g\rangle$ and $|e\rangle$, state $|e\rangle$ is substantially populated and the HHG process shifts to that starting from superposition between $|g\rangle$ and $|e\rangle$. As the electron recombines to the ground state with return energy equals to ΔE, it emits harmonics with frequencies $\Delta E \pm 2k\omega$. A portion of the resonant photons excite electrons from $|g\rangle$ to $|e\rangle$ hence further increasing the intensity of the resonant radiation.

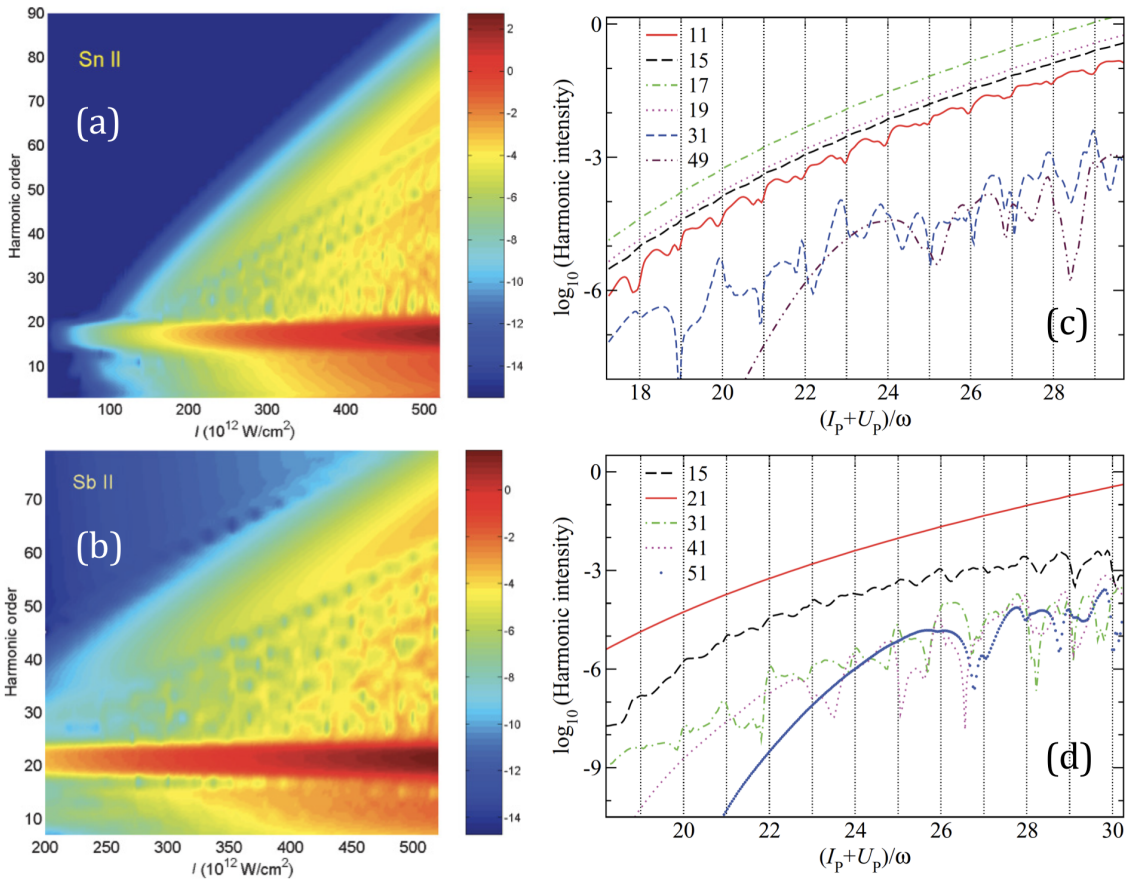

Figure 2.3: The HH spectra from (a) Sn^+ and (b) Sb^+ as a function of fundamental laser intensity. The profiles of some selected harmonics from Sn^+ are shown in (c) while those from Sb^+ in (d). Reprinted figure with permission from [D. B. Milošević, "Resonant high-order harmonic generation from plasma ablation: Laser intensity dependence of the harmonic intensity and phase", *Phys. Rev. A* **81**, 023802 (2010)]. Copyright 2010 by the American Physical Society.

This superposition model to describe resonant HHG has also been employed to investigate the behavior of resonant harmonic intensity and phase with respect to laser intensity [71]. Fig. 2.3(a) and (b) show the HH yields for Sn^+ and Sb^+ in a 2D color plot as functions of harmonic order and intensity. From 2.3(a) and (b) we can clearly see the enhanced 17-th and 21-st harmonics, respectively. Fig. 2.3(c) and (d) plots the intensity of several selected harmonics from Fig. 2.3(a) and (b), respectively, as functions of laser intensity. The intensity of harmonic orders outside the resonant region (e.g. the 11-th, 31-st, and 49-th harmonics in Sn^+) exhibits oscillatory behavior after certain laser intensity. Such oscillatory behavior has been shown to be from interference of many quantum orbits [72–74]. On the other hand, the intensities of resonant harmonics (17-th in Sn^+ and 21-st in Sb^+) increases monotonically without exhibiting any oscillation. The phase of several harmonics are also plotted in Fig. 2.4(a) for Sn^+ and 2.4(b) for Sb^+. From Fig. 2.4 we can see in general the phase of ordinary harmonics vary linearly with respect to laser intensity, this is consistent with earlier findings [12] that shows that the phase varies as $U_p\tau$ where τ is the travel time of the corresponding quantum orbit. The phase of the resonant harmonics however is remarkably stable.

To summarize, this theoretical model which tries to approach the problem about the mechanism of resonant HHG assumes the initial state to be a superposition of stationary states. The results show that this model is indeed able to reproduce the enhancement and further allows investigation of the behavior of resonant harmonic intensity and phase. Despite these successes, this model does not explain in detail how the state $|e\rangle$ gets its population starting from zero. In fact, the corresponding amplitude c_e is taken to be constant while the temporal evolution of this coefficient can be intuitively estimated to be crucial in arriving at an accurate description of the mechanism in question.

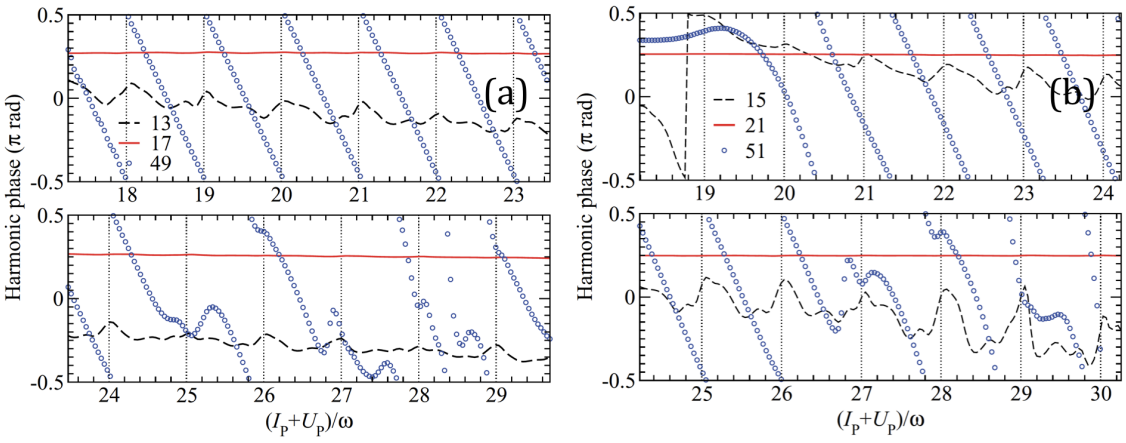

Figure 2.4: The phase of some selected harmonics from (a) Sn^+ and from (b) Sb^+. Reprinted figure with permission from [D. B. Milošević, "Resonant high-order harmonic generation from plasma ablation: Laser intensity dependence of the harmonic intensity and phase", *Phys. Rev. A* **81**, 023802 (2010)]. Copyright 2010 by the American Physical Society.

2.2 The Four-Step Model

In Section 2.1, we presented a mathematical approach for describing the physics of resonant HHG. The underlying mathematical tool of the approach is the use Lewenstein model to calculate time-dependent dipole moment. A different viewpoint on the subject of resonant HHG was proposed by Strelkov who suggested a modification of three-step model to insert an additional step relevant in explaining the excitation of the upper resonant state [52]. The suggested process, which is dubbed "four-step model", replaces the third step with a recombination to the upper resonant state instead of the ground state. In the fourth step, this electron then relaxates back to the ground state emitting the resonantly enhanced HH photon. The four-step model is schematically depicted in Fig. 2.5. It is worthwhile to appreciate the difference between this model and the superposition of states model in the previous section. There, the entire process is essentially the usual three-step process only that the starting state is the upper resonant state (see Fig. 2.1). Whereas in four-step model, the resonant state comes into play at the third step, not in the first step.

Four-step model was further quantitavely studied by Tudorovskaya and Lein [50] where the HH spectrum is calculated in a more formal way - solving the time-dependent Schrödinger equation. The key point of their method is the use of an artificial potential having a pair of barrier surrounding the origin. In most experimentally observed resonant HHG, the energy corresponding to the enhanced harmonic is close to the energy difference between the ground

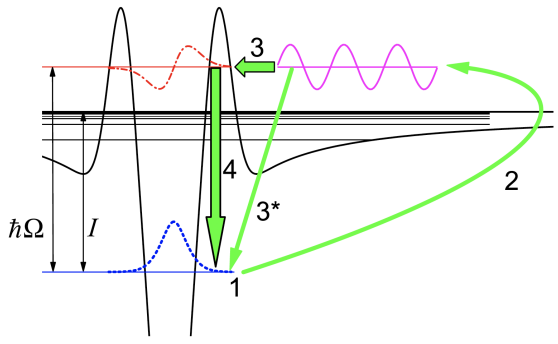

Figure 2.5: A schematic picture illustrating 4-step model. In the first step, an electron tunnels through a potential barrier. In the second step, it is driven by the strong electric field in continuum. In the next step, it recombines to an excited, metastable state. In the last step, it relaxates to its initial state emitting the resonantly enhanced photon. Reprinted figure with permission from [V. Strelkov, "Role of Autoionizing State in Resonant High-Order Harmonic Generation and Attosecond Pulse Production", *Phys. Rev. Lett.* **104**, 123901 (2010)]. Copyright 2010 by the American Physical Society.

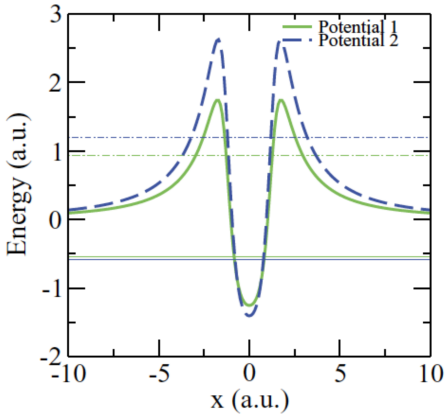

Figure 2.6: The shapes of Potential 1 and Potential 2, with the latter having higher barriers. Reprinted figure with permission from [M. Tudorovskaya and M. Lein, "High-order harmonic generation in the presence of a resonance", *Phys. Rev. A* **84**, 013430 (2011)]. Copyright 2011 by the American Physical Society.

state and some autoionizing state such that these two states are coupled by a giant transition amplitude. An autoionizing state, being a state with a localized probability but is embedded in continuum, makes its formal realization only possible if the system has at least two electrons. For single electron methods such as the one considered here, the autoionizing state must be added 'by hand' and the barriers in this method are introduced exactly for this purpose.

The 1D Schrödinger equation to be solved reads

$$i\frac{\partial}{\partial t}\Psi(x,t) = \left(-\frac{1}{2}\frac{\partial^2}{\partial x^2} + V(x) + \mathcal{E}(t)x\right)\Psi(x,t) \tag{2.4}$$

where $V(x)$ takes the form

$$V(x) = \alpha\left(\frac{1}{1+\exp\left(\frac{x+\beta}{\gamma}\right)} + \frac{1}{1+\exp\left(\frac{-x+\beta}{\gamma}\right)} - 1\right) + \frac{\delta}{\epsilon + x^2}\left(\frac{1}{1+\exp\left(\frac{x+\beta}{\gamma}\right)} + \frac{1}{1+\exp\left(\frac{-x+\beta}{\gamma}\right)}\right),$$

and $\mathcal{E}(t) = \mathcal{E}_0 f(t)\sin(\omega_L t)$ where $\mathcal{E}_0$ and ω_L are related to the laser intensity, which is set to 4×10^{14} W/cm^2, and to the laser wavelength, which is set to 800 nm. The pulse envelope $f(t)$ has a trapezoidal shape supporting 9 optical cycles. The initial state $\Psi(x, t = 0)$ is taken to be the ground state $\Psi_0(x)$ of the right hand side Hamiltonian of Eq. (2.4) with the external field set to zero. Split-operator technique [75, 76] is employed to integrate Eq. (2.4). The effect of barrier shape on the HH emission is investigated by employing two different potentials $V(x)$ whose parameters are $\alpha_1 = 1.32$, $\beta_1 = 1.27$, $\gamma_1 = 0.23$, $\delta_1 = 9.5$, $\epsilon_1 = 1.4$ for potential 1 and $\alpha_2 = 1.5$, $\beta_2 = 1.27$, $\gamma_2 = 0.23$, $\delta_2 = 14$, $\epsilon_2 = 1.4$ for potential 2.

The two potentials are plotted in Fig. 2.6. The lifetime of the metastable states for both potentials is calculated from the width of the corresponding peak in the Fourier transform of a correlation function. This correlation function is calculated as $c(t) = \langle\Phi_0|\Phi(t)\rangle$ where $\Phi_0(x) = \Phi_G(x) - \langle\Psi_0|\Phi_G\rangle\,\Psi_0(x)$, $\Phi_G(x) = \exp\left(-(x-0.9)^2\right)$, and $\Phi(x,t)$ is a time-dependent function resulting from propagating $\Phi_0(x)$ using the same Hamiltonian. It is found that the lifetime of the autoionizing state in potential 1 is 34 a.u. and in potential 2 141 a.u.. Fig. 2.7(a) and (b) show time-frequency spectrograms for potential 1 and 2. The time-frequency spectrogram is obtained by taking the magnitude squared of $G(\omega, t)$ given by

$$G(\omega,t) = \int \mathrm{d}\tau\, a(\tau)\exp\left(-\frac{(t-\tau)^2}{2\sigma^2}\right)$$

where $a(t)$ is the acceleration calculated as

$$a(t) = \langle\Psi(t)|\frac{\mathrm{d}V(x)}{\mathrm{d}x} + \mathcal{E}(t)|\Psi(t)\rangle$$

(note that by definition, $a(t) = \mathrm{d}d(t)/\mathrm{d}t$ where $d(t)$ is given by the right hand expression of the first line of Eq. (2.2)) and the HH spectrum is then obtained by taking the magnitude squared of

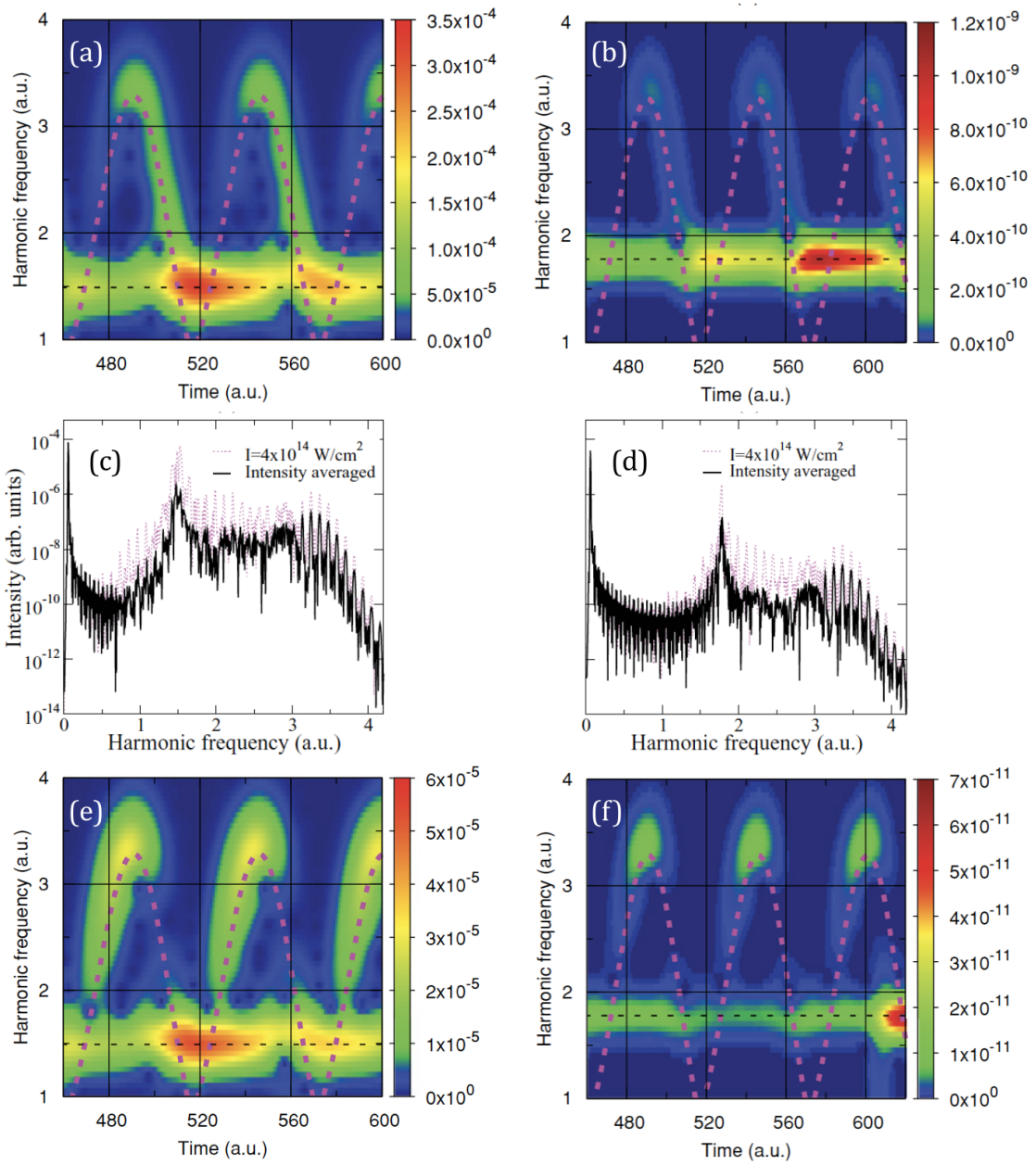

Figure 2.7: (a) and (b) show the time-frequency spectrograms using Potential 1 and Potential 2, respectively. The effect of intensity averaging (black) on single-atom spectra (pink dashed) is shown in (c) for Potential 1 and in (d) for Potential 2. (e) and (f) display the effect of intensity averaging on the time-frequency spectrograms for Potential 1 and Potential 2, respectively. Reprinted figure with permission from [M. Tudorovskaya and M. Lein, "High-order harmonic generation in the presence of a resonance", *Phys. Rev. A* **84**, 013430 (2011)]. Copyright 2011 by the American Physical Society.

the Fourier transform of $a(t)$. In contrast to the established understanding, the HH signals in Fig. 2.7(a) within the plateau region are mainly contributed by long trajectories. This is, however, an artifact of 1D simulation and in 3D simulation, the short trajectories prevail [77]. The existence of enhanced harmonics at 1.5 a.u. and 1.75 a.u. is evident from the spectrograms in Fig. 2.7(a) and (b), respectively. That these peaks indeed correspond to a transition between the ground state and the autoionizing state in each potential, one may compare their harmonic energies with energy difference between the two states in question which can be deduced from Fig. 2.6.

Macroscopic effects such as phase matching poses an interesting question because for a given harmonic order, a constructive interference across the beam path inside the medium is necessary to have non-vanishing signal at the detector. To model macroscopic effect, an intensity averaging

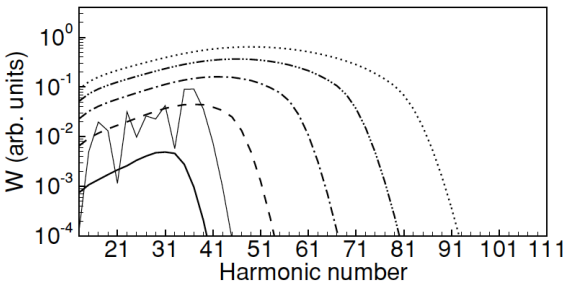

Figure 2.8: The focal-averaged wave packet $\mathcal{W}(E_k)$ for Cr^+ for different intensities $I = \tilde{I} \times 10^{14}$ W/cm^2 and $\lambda = 800$ nm. Solid line, $\tilde{I} = 2$; dashed line, $\tilde{I} = 3$; dash-dotted line, $\tilde{I} = 4$; dash-dot-dotted line, $\tilde{I} = 5$; dotted line, $\tilde{I} = 6$. Thin solid line, $\mathcal{W}E_k$ for $\tilde{I} = 2$ without focal averaging. Reprinted figure with permission from [M. V. Frolov, N. L. Manakov, and A. F. Starace, "Potential barrier effects in high-order harmonic generation by transition-metal ions", *Phys. Rev. A* **82**, 023424 (2010)]. Copyright 2010 by the American Physical Society.

procedure is performed by calculating $a_{\text{eff}}(t)$,

$$a_{\text{eff}}(t) = \frac{1}{N} \sum_{i}^{N} a_{I_i}(t)$$

with $N = 31$ intensities between 3.85×10^{14} and 4.15×10^{14} W/cm^2. The averaged HH spectra are plotted in solid line in Fig. 2.7(c) and (d) for potential 1 and potential 2, respectively, along with single atom spectra (red dased). In general, intensity averaging lower the harmonic intensities but the global trend is maintained, the enhanced peaks using both potentials remain prominent. The lowered intensity for harmonics lower than the enhanced harmonic is caused by the barriers repelling the slow moving returning electrons. The intensity averaged spectrograms usign both potentials are depicted in Fig. 2.7(e) and (f). These spectrograms highlight the the difference in phase variation between short and long trajectories from which we can see that the phase of long trajectories generally vary faster than short trajectory leading to the diminishing signals from the former. Looking at the enhanced harmonic signal, we see that potential 2 spectrogram has lower intensity. This behavior may be rooted in the longer lifetime, 141 a.u., of the autoionizing state in potential 2, which is longer than the optical cycle for an 800-nm laser field. Therefore, when an electron is captured in the autoionizing state, a portion of the previous electron in that state is still there and the interference between the two corresponding wavepackets can be constructive or destructive.

2.3 Factorization Formula for HHG Rate

Based on the factorization formula for HHG rate [78], this approach tries to estimate the intensity of resonantly enhanced harmonic relative to those of the neighboring harmonics. According to this factorization formula, the emission rate of HH photons may be approximately expressed as a product of three factors, each of which can be associated with the three steps in the semi-classical three-step model of HHG [26, 28]. With $\mathcal{T}$ being the tunneling-ionization factor, $\mathcal{W}(E_k)$ the wavepacket propagation factor, and $\sigma_R(E_k)$ the photorecombination cross-section, the rate of HH emission $R(E)$ around the high-energy end of the plateau reads

$$R(E) = \mathcal{T}\mathcal{W}(E_k)\sigma_R(E_k) \tag{2.5}$$

where E_k is the returning electron kinetic energy. The propagation part of Eq. (2.5) includes interference effect between short and long trajectories throughout the course of the electron in continuum. While $\sigma_R(E)$ describes the recombination event by emitting a photon of energy $E = E_k + I_p$. Frolov et al. attempted to apply this approach to explain resonant enhancement in HHG [51].

In order to better imitate experimental condition where the HH signal emanates from an ensemble of atomic sources, focal averaging is carried out. Since only $\mathcal{T}$ and $\mathcal{W}(E_k)$ depend on intensity, the averaging is carried out on the quantity $W(E_k) = \mathcal{T}\mathcal{W}(E_k)$. The effect of focal averaging for several laser intensities on $W(E_k)$ launched from Cr^+ is displayed in Fig. 2.8. It is

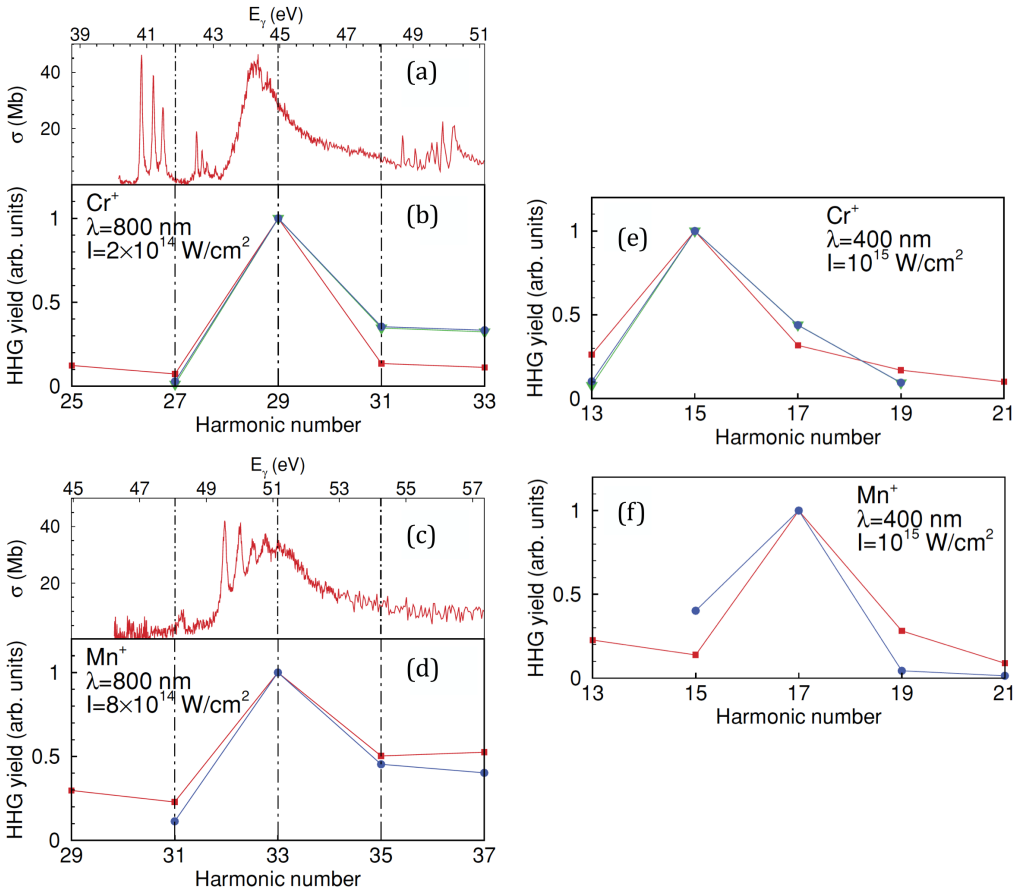

Figure 2.9: (a) and (c) are experimental photoionization cross sections for Cr^+ and Mn^+, respectively [79]. In (b), (d), (e), and (f), the experimental HH yield taken from [37] for Cr^+ and [80] for Mn^+ are represented by the red square markers. The blue dot and green triangle markers are the results from Eq. (2.5). Reprinted figure with permission from [M. V. Frolov, N. L. Manakov, and A. F. Starace, "Potential barrier effects in high-order harmonic generation by transition-metal ions", *Phys. Rev. A* **82**, 023424 (2010)]. Copyright 2010 by the American Physical Society.

seen that the effect of focal averaging is to smooth out the interference fringes coming from short and long trajectories interference. This means if there should be any particular feature showing up in $R(E)$, it must come from $\sigma_R(E_k)$.

HH yields calculated through the factorization formula (2.5) for Cr^+ and Mn^+ using various laser parameters are shown in Fig. 2.9(b), (d), (e), and (f). The experimental photoionization cross sections for Cr^+ and for Mn^+ depicted in Fig. 2.9(a) and (c), respectively, are employed along with the use of principle of detailed balance to calculate the photorecombination cross sections σ_R for each element [51, 81, 82]. Comparing with experimental HHG spectra, the HH yields obtained using factorization formula show a good qualitative agreement for a range of laser parameters as indicated in Fig. 2.9. This approach, however, is limited by the applicability interval of Eq. (2.5) this equation holds only near the cutoff energy in the HH spectrum [78]. Moreover, the energy range of available experimental photoionization cross sections are generally limited.

2.4 Summary

Several single-active electron approaches have been proposed since the first experimental observation of resonant HHG from plasma. Superposition of intiial states model stipulates that the enhancement is a result of a generalized three-step model, where in the first step, an electron can be first excited to an excited state before being tunnel-ionized. The enhanced emission takes place when this electron recombines into the ground state. In shape resonance approach, the core potential is modelled to have barriers surrounding the origin. These barriers ensures the existence of a meta-stable (autoionizing) eigenstate which is then coupled in resonance with the

ground state upon interaction with a laser. Factorization formula which was originally formulated for ordinary HHG had also been applied for resonant HHG. Using experimental photoionization cross section incorporated into the calculation, this model also predicts an enhanced harmonic around the same energy as the large peak found in the photoionization cross section.

While these methods succeeded in reproducing the enhancement, these results along with the features in the HH spectra are subject to the starting assumptions because the methods employed were not first-principles. Most of these methods also use single-active-electron approximation, and hence the multi-electron effects, such as electron correlation and multiple ionization, which can be the actual underlying mechanism, cannot be investigated. In the next chapter, a mathematical account of one of the most successful *ab initio* all-electron methods will be presented.

Chapter 3

Description of The Theoretical Methods

Quantum mechanics is a very successful standard model theory. It has gone through a multitude of experimental tests and it never fails to accurately predict the experimental outcomes provided the energies involved are well below the rest mass of the involved particles. Every non-relativistic system involving atomic or subatomic particles is theoretically described by a scalar wavefunction Ψ satisfying the so-called *Schrödinger equation*, a multi-variable partial differential equation, which for an N-electron atom reads

$$i\hbar\partial_t\Psi(t,\mathbf{x}_1,\ldots,\mathbf{x}_N) = H(t,\mathbf{x}_1,\ldots,\mathbf{x}_N)\Psi(t,\mathbf{x}_1,\ldots,\mathbf{x}_N) \tag{3.1}$$

with

$$H(t,\mathbf{x}_1,\ldots,\mathbf{x}_N) = \sum_{i=1}^{N}\left(-\frac{\hbar^2}{2m}\nabla_i^2 - \frac{Ze^2}{4\pi\epsilon_0}\frac{1}{r_i} + V_{\text{ext}}(t,\mathbf{x}_i)\right) + \frac{e^2}{4\pi\epsilon_0}\sum_{i=1}^{N}\sum_{j>i}^{N}\frac{1}{|\mathbf{r}_i-\mathbf{r}_j|} \tag{3.2}$$

where $\mathbf{x}_i$ is the composite coordinate of the i-th electron, $\mathbf{x}_i \equiv (\mathbf{r}_i, s_i)$, $\mathbf{r}_i$ the Cartesian coordinate, s_i the spin coordinate, Z the nuclear charge, and $V_{\text{ext}}(t,\mathbf{x}_1,\ldots,\mathbf{x}_N)$ accounts for any external interaction. The correct spin coordinate of each electrons is required to obtain a ground state with the correct spin symmetry. Eq. (3.2) is unfortunately only analytically solvable for hydrogen-like systems where $N = 1$ (for reference, see Ref. [83, Sec. 4.2]). Increase the number of electrons more than this and one will be left with no choice but to resort to numerical solution.

In this chapter, the theoretical foundation of the methods of choice in performing all simulations in this thesis, dubbed as *time-dependent multiconfiguration self-consistent field* (TD-MCSCF), will be outlined and discussed. In TD-MCSCF method, the wavefunction is represented as a linear combination of many time-dependent Slater determinants,

$$\Psi(t,\mathbf{x}_1,\ldots,\mathbf{x}_N) = \sum_I C_I(t)I(t,\mathbf{x}_1,\ldots,\mathbf{x}_N) \tag{3.3}$$

where $I(t,\mathbf{x}_1,\ldots,\mathbf{x}_N) = (1/\sqrt{N!})\det(\phi_1^I(t,\mathbf{x}_1),\ldots,\phi_N^I(t,\mathbf{x}_N))$ is a time-dependent Slater determinant, $C_I(t)$ is time-dependent configuration interaction (CI) coefficient, and $\phi_i(t,\mathbf{x})$ is time-dependent orbitals. TD-MCSCF is based on variational principle where the wavefunction that (approximately) solves Schrödinger equation (3.1) is obtained by searching for the minimum of a certain functional. Performing this calculation, one obtains the optimum CI coefficients and orbitals at every time step. A particular case of TD-MCSCF in which *all* possible electron configurations are included in the expansion Eq. (3.3) is called *multiconfiguration time-dependent Hartree-Fock* (MCTDHF) [60–62]. Other variants include *time-dependent complete active space self-consistent field* (TD-CASSCF) [63, 64], *time-dependent occupation restricted multiple active space* (TD-ORMAS) [65], and *time-dependent restricted active space self-consistent field* (TD-RASSCF) [66]. Each of these method attempts to reduce the computational cost of MCTDHF by enabling a custom setting of various orbital occupation numbers. For a review of several existing time-dependent *ab initio* methods, see Ref. [84]. The majority of results presented in this dissertation were obtained using TD-CASSCF and TD-ORMAS for which reason these two methods will also be discussed in this chapter.

In Section 3.1, the mathematical foundation of TD-MCSCF will be presented in the language of variational principle. An important improvement in computational speed to MCTDHF is achieved by TD-CASSCF method, this will be covered in Section 3.2 where important concepts such as redundant orbital rotations will also be explained. In Section 3.3, further speed improvement technique by manipulating the occupations of certain orbitals is discussed in terms of TD-ORMAS method. This chapter is concluded by a discussion about the three important observables in theoretical strong-field physics: dipole moment, dipole velocity, and dipole acceleration, which are necessary to calculate the high-harmonic spectrum.

3.1 TD-MCSCF Method

In quantum chemistry, the well-known multiconfiguration self-consistent field (MCSCF) method is very successfull in calculating the stationary properties of atoms and molecules. Inspired by this success, the time-dependent extension, TD-MCSCF, was developed to tackle quantum mechanical problems involving time-dependent external field. The unknowns, i.e. the quantities to be varied to give the desired solution wavefunction, in TD-MCSCF method are the time-dependent CI coefficients and time-dependent spatial orbitals (see Eq. (3.3)). As in most variational principle calculations, given an integral to be minimized we try to find a set of partial differential equations which are satisfied by the quantities (i.e. the above-mentioned unknowns) which minimize the starting integral. This section is devoted to deriving such differential equations governing the time-dependent CI coefficients and spatial orbitals. For the purpose of analysis of TD-MCSCF methods, we will adopt second quantization representation of operators (for reference, see Ref. [85, Ch. 1]). In this representation, the Schrödinger equation (3.1) becomes

$$i\partial_t|\Psi\rangle = \hat{H}|\Psi\rangle$$

with

$$\hat{H} = \sum_{M,N} h_{MN}\hat{a}_M^\dagger \hat{a}_N + \frac{1}{2}\sum_{M,N,\Lambda,\Gamma} U_{MN,\Lambda\Gamma}\hat{a}_M^\dagger \hat{a}_N^\dagger \hat{a}_\Gamma \hat{a}_\Lambda \tag{3.4}$$

$$h_{MN} = \int d\mathbf{x}\, \phi_M^*(\mathbf{x})\left(-\frac{1}{2}\nabla^2 - \frac{Z}{r} + V_{\text{ext}}(t,\mathbf{x})\right)\phi_N(\mathbf{x}) \tag{3.5}$$

$$U_{MN,\Lambda\Gamma} = \int d\mathbf{x}_1 \int d\mathbf{x}_2\, \frac{\phi_M(\mathbf{x}_1)^*\phi_N(\mathbf{x}_2)^*\phi_\Lambda(\mathbf{x}_1)\phi_\Gamma(\mathbf{x}_2)}{|\mathbf{r}_1 - \mathbf{r}_2|}. \tag{3.6}$$

where each index M is to be understood as a composite index (μ, s) between spatial μ and spin s orbitals. The operators $\hat{a}^\dagger$ and $\hat{a}$ are creation and annihilation operators for electron (fermion). Some relevant properties of creation and annihilation operators for fermions are summarized in Appendix A. In our TD-MCSCF implementation, the spin-orbital are restricted, i.e. a single spatial orbital is shared by the up and down spin functions. Given the fact that none of the operators appearing in the Hamiltonian (3.2) are spin-dependent, Eq. (3.4) can then be reduced to

$$\hat{H} = \sum_{\mu,\nu} h_{\mu\nu}\hat{E}_\nu^\mu + \frac{1}{2}\sum_{\mu,\nu,\lambda,\gamma} U_{\mu\nu,\lambda\gamma}\hat{E}_{\lambda\gamma}^{\mu\nu}$$

with

$$\hat{E}_\nu^\mu = \sum_s \hat{a}_{\mu s}^\dagger \hat{a}_{\nu s} \tag{3.7}$$

$$\hat{E}_{\lambda\gamma}^{\mu\nu} = \sum_{s,s'} \hat{a}_{\mu s}^\dagger \hat{a}_{\nu s'}^\dagger \hat{a}_{\gamma s'}\hat{a}_{\lambda s} = \hat{E}_\lambda^\mu \hat{E}_\gamma^\nu - \hat{E}_\gamma^\mu \delta_\lambda^\nu \tag{3.8}$$

where a property of creation and annihilation operators in Appendix A has been used.

As mentioned in the opening of this chapter, TD-MCSCF obtains the wavefunction by minimizing a certain functional, this functional is referred to as *time-dependent variational principle* (TDVP) [86–89] functional,

TDVP functional

$$S[\Psi] = \int_{t_0}^{t} dt' \langle\Psi(t')|H - i\partial_{t'}|\Psi(t')\rangle \tag{3.9}$$

where the temporal, spatial, and spin dependence in the Hamiltonian and wavefunction have been suppressed. For each t, our goal is to find a particular wavefunction $\left|\Psi^{(0)}(t)\right\rangle$ such that $S[\Psi = \Psi^{(0)}(t)]$ is a stationary point, i.e. $\delta S[\Psi^{(0)}(t)] = 0$, that is to say our solution wavefunction is an extremum of $S[\Psi]$. The emerging optimization problem will definitely be that of a nonlinear type since the orbitals and CI coefficients are connected by multiplication in Eq. (3.3). To facilitate the derivation, we will make use of one-parameter family approach [90, p. 20] in which the variational quantity (i.e. $|\Psi\rangle$) is expressed in terms of a family of functions the members of which are distinguished by a single parameter ϵ,

$$|\Psi_\epsilon(t')\rangle = \left|\Psi^{(0)}(t')\right\rangle + G(\epsilon, t') \tag{3.10}$$

where the dependence on all-electron coordinates are implied. The offset function $G(\epsilon, t)$ is a function which is required to obey the following conditions

$$G(0, t') = 0 \tag{3.11a}$$
$$G(\epsilon, t' = t_0) = G(\epsilon, t' = t) = 0 \tag{3.11b}$$

for the following reasons. The first condition reduces the complexity of the derivation because by setting $\epsilon = 0$ anywhere in the derivation automatically brings the wavefunction $|\Psi_\epsilon(t')\rangle$ (as we shall see later, the CI coefficients and orbitals as well) that is involved in that particular step to the optimized one $\left|\Psi^{(0)}(t')\right\rangle$. The second condition ensures that for any time t, the algorithm searches for the solution within a family of functions having the same initial and final values as the optimized wavefunction. As a side note, both of these conditions are, from rudimentary theoretical point of view, optional since Eq. (3.11a) serves to simplify the effort while Eq. (3.11b) narrows the search space of the algorithm - it rejects all outrightly wrong functions having incorrect initial and final values.

One way to adapt the form Eq. (3.3) for the wavefunction to Eq. (3.10) is to expand CI coefficients in powers of ϵ and introduced a unitary-transformed determinant,

$$|\Psi_\epsilon(t)\rangle = \sum_I \left(C_I^{(0)}(t) + \epsilon C_I^{(1)}(t) + O(\epsilon^2, t)\right) e^{-\epsilon\hat{\mathcal{A}}(t)} |I^{(0)}(t)\rangle \tag{3.12}$$

where the unitary operator $\exp\left(-\epsilon\hat{A}(t)\right)$ is to be understood as an infinte sum

$$e^{-\epsilon\hat{\mathcal{A}}(t)} = \sum_{n=0}^{\infty} \frac{\left(-\epsilon\hat{\mathcal{A}}(t)\right)^n}{n!}.$$

Thus setting $\epsilon = 0$,

$$|\Psi^{(0)}(t)\rangle = \sum_I C_I^{(0)}(t) |I^{(0)}(t)\rangle \tag{3.13}$$

with $I^{(0)}(t) = (1/\sqrt{N!})\det((\phi_1^I)^{(0)}(t), \ldots, (\phi_N^I)^{(0)}(t))$. Substracting Eq. (3.13) from Eq. (3.12) gives $G(\epsilon, t)$ and with this designation, we automatically have $G(0, t) = 0$. The remaining conditions required to satisfy (3.11b) are therefore

$$C_I^{(r)}(t_0) = C_I^{(r)}(t) = 0, \qquad r \geq 1, \forall\, I \tag{3.14a}$$
$$\hat{\mathcal{A}}(t_0) = \hat{\mathcal{A}}(t) = 0. \tag{3.14b}$$

Hence, our task is now clear. We are going to find the stationary point of the functional $S[\Psi]$ with respect to a family of one-parameter functions defined in Eq. (3.12) and (3.14). However before moving on, in order to remove unnecessary notational complication we shall change the notations for the optimized quantities: $\Psi^{(0)} \to \tilde{\Psi}$, $C_I^{(0)} \to \tilde{C}_I$, $I^{(0)} \to \tilde{I}$, and $\phi_\mu^{(0)} \to \tilde{\phi}_\mu$.

We are only interested in the stationary point of $S[\Psi_\epsilon]$, therefore the next step would be to differentiate Eq. (3.9), using Eq. (3.12), with respect to ϵ, and then set the right hand side to zero. When performing the last step, one must also replace ϵ with zero because we have defined the wave function in Eq. (3.13) to be the one that makes $S[\Psi_\epsilon]$ stationary. One obtains the following equation

$$\int_{t_0}^{t} dt' \left(\langle\Psi^{(1)}|H - i\partial_{t'}|\tilde{\Psi}\rangle + \langle\tilde{\Psi}|H - i\partial_{t'}|\Psi^{(1)}\rangle\right) = 0 \tag{3.15}$$

with

$$|\Psi^{(1)}\rangle = \partial_\epsilon |\Psi_\epsilon\rangle\big|_{\epsilon=0} = \sum_I C_I^{(1)} |\tilde{I}\rangle - \hat{\mathcal{A}}|\tilde{\Psi}\rangle. \tag{3.16}$$

In Eq. (3.15), the operator $H - i\partial_{t'}$ can be moved into the bras because of the following reason. First of all, this obviously applies to H because it is Hermitian. As for $i\partial_{t'}$, we observe that the wave function $|\tilde{\Psi}\rangle$ as well as all of its derivatives are analytic (i.e. non-singular) and square-integrable at all times. One can see that this is the case from the fact that the wave function is spanned by finite, square-integrable determinants and its derivatives (e.g. the first one, given by Eq. (3.16)) live in the same Fock space. Due to this finiteness and square-integrability of the wave function and its derivatives, the order of time and spin-space integrals (as designated by the braket notations) can be interchanged. Applying this on the second term of Eq. (3.15) and performing the innermost, time integral by integration by part, one has

$$\begin{aligned}\int_{t_0}^{t} dt' \tilde{\Psi}^* \left(-i\partial_{t'} \Psi^{(1)}\right) &= -i\tilde{\Psi}^*(t')\Psi^{(1)}(t')\big|_{t'=t_0}^{t'=t} + i\int_{t_0}^{t} dt' \left(\partial_{t'}\tilde{\Psi}^*\right)\Psi^{(1)} \\ &= i\int_{t_0}^{t} dt' \left(\partial_{t'}\tilde{\Psi}^*\right)\Psi^{(1)}\end{aligned}$$

where the second equality follows from Eq. (3.16) together with Eq. (3.14). Therefore, we may now rewrite Eq. (3.15) as

$$\int_{t_0}^{t} dt' \left(\langle\Psi^{(1)}|(H - i\partial_{t'})\tilde{\Psi}\rangle + \langle(H - i\partial_{t'})\tilde{\Psi}|\Psi^{(1)}\rangle\right) = 0 \tag{3.17}$$

which tells us that the integral of the real part of the quantity $\langle\Psi^{(1)}|(H - i\partial_{t'})\tilde{\Psi}\rangle$ must vanish for every time t for the functional $S[\Psi]$ to be stationary. These steps shall also illustrate the necessity to define TDVP by including the time integration in Eq. (3.9) as it allows us to carry out integration by part on t' which leads us to Eq. (3.17).

Before proceeding to derive the equations of motion (EOM), let's set a check point here and make a recollection about what we have done so far. First of all, in TD-MCSCF the optimized quantities are the CI coefficients C_I and the orbitals (whose variations are embodied in the operator $\hat{\mathcal{A}}$). In arriving at Eq. (3.17), we differentiate $S[\Psi_\epsilon]$ with respect to ϵ and then require $\partial_\epsilon S[\Psi_\epsilon] = 0$ when $\epsilon = 0$. Looking back at Eq. (3.12), when $\epsilon = 0$ we will have the optimized wavefunction (3.13) regardless of the choice of $C_I^{(1)}$ (as well as all other $C_I^{(r)}$ for $r > 1$) and $\hat{\mathcal{A}}$. This implies that Eq. (3.17) must be satisfied by arbitrary choice of $C_I^{(1)}$ and $\hat{\mathcal{A}}$. The independence between CI coefficients and orbitals also necessitates a separate variation between them. These requirements provide a guidance in deriving the equations of motion.

3.1.1 CI Coefficient Equation of Motion

Now that we have cast the essential equation into a more transparent form of Eq. (3.17) where the integrand turns out to be the sum of a complex quantity and its complex conjugate, we can work on either term to proceed and incorporate the complex conjugate counterpart once we get close to the final expression. Let's pick out the second term and use Eq. (3.16) to substitute for $|\Psi^{(1)}\rangle$,

$$\int_{t_0}^{t} dt' \langle(H - i\partial_t)\tilde{\Psi}| \left(\sum_I C_I^{(1)} |\tilde{I}\rangle - \hat{\mathcal{A}}|\tilde{\Psi}\rangle\right). \tag{3.18}$$

Since for the moment we are interested in CI coefficient EOM and the CI coefficients must be variationally optimized independently from orbitals, upon expansion of Eq. (3.18) on the terms inside parentheses, we only need to focus on the $C_I^{(1)}$ part. The resulting expression contains an integral $\langle(H - i\partial_t)\tilde{\Psi}|\tilde{I}\rangle$ and thus in what follows we will delineate how the action of time derivative on the wave function can be more conveniently expressed in operator form. First of all, it should be obvious that

$$|i\partial_t \tilde{\Psi}\rangle = \sum_I i\dot{\tilde{C}}_I |\tilde{I}\rangle + \sum_I \tilde{C}_I |i\partial_t \tilde{I}\rangle. \tag{3.19}$$

Moreover, due to the product rule of derivative, the first time derivative acting on a determinant acts like the sum of single electron operators and consequently, in second quantization the vector

$|i\partial_t I\rangle$ in Eq. (3.19) may be represented as

$$|i\partial_t I\rangle = \hat{\mathcal{R}}|I\rangle = \sum_{i=1}^{N} \hat{R}(i)|I\rangle = \sum_{\mu,\nu} R_{\mu\nu}\hat{E}^{\mu}_{\nu}|I\rangle$$

where

$$\hat{\mathcal{R}} = \sum_{i} \hat{R}(i) = \sum_{\mu,\nu} R_{\mu\nu}\hat{E}^{\mu}_{\nu}$$
$$R_{\mu\nu} = \int d\mathbf{x}\, \phi^{*}_{\mu}(t,\mathbf{x})\,(i\partial_t \phi_{\nu}(t,\mathbf{x}))\,.$$

This operator $\hat{\mathcal{R}}$ symbolizes a *direct action* of first time derivative on a determinant. As a short remark about the property of $\hat{\mathcal{R}}$, despite being connected in some way with time differentiation, operator $\hat{\mathcal{R}}$ acts directly on determinants, it can "go through" CI coefficients although they are also time-dependent. The hermiticity of R can be guaranteed if furthermore we require the inner products of the time-dependent orbitals to be time-independent, which is the case in most implementation of TD-MCSCF. This is because taking the i-multiplied time derivative of $\langle\phi_\mu|\phi_\nu\rangle \neq f(t)$ gives

$$i\langle\partial_t\phi_\mu|\phi_\nu\rangle + i\langle\phi_\mu|\partial_t\phi_\nu\rangle = 0$$
$$\langle\phi_\mu|i\partial_t\phi_\nu\rangle = \langle i\partial_t\phi_\mu|\phi_\nu\rangle$$

hence establishing the hermitian property of "operator" $i\partial_t$. As a consequence of this property, the matrix elements of $\hat{\mathcal{R}}$ between Slater determinants also obey

$$\langle J|\hat{\mathcal{R}}I\rangle = \langle\hat{\mathcal{R}}J|I\rangle. \tag{3.20}$$

Substituting Eq. (3.19) and (3.20) into the CI part of Eq. (3.18) and with the addition of its complex conjugate, one obtains the CI part of Eq. (3.17), namely

$$\int_{t_0}^{t} dt' \sum_{I} C^{(1)}_{I}\left(\langle\tilde{\Psi}|H - \hat{\mathcal{R}}|I\rangle + i\dot{C}^{*}_{I}\right) + \text{c.c.} = 0. \tag{3.21}$$

As often adopted in literatures [91], we stipulate that C_I and its complex conjugate to be variationally independent, which according to (3.21), allows to write for the CI coefficient EOM

$$\begin{aligned} i\dot{\tilde{C}}_I &= \langle\tilde{I}|H - \hat{\mathcal{R}}|\tilde{\Psi}\rangle \\ &= \sum_{J} \tilde{C}_J \left\langle\tilde{I}\middle|\hat{H} - \hat{\mathcal{R}}\middle|\tilde{J}\right\rangle \end{aligned} \tag{3.22}$$

Note that, however, due to the freedom in choosing the global phase of the wavefunction, Eq. (3.22) is not unique - another form of CI coefficient EOM differing in the presence of an additional time-dependent term than Eq. (3.22) also exists. If we were to introduce a global phase factor to the solution of TD-MCSCF, it is most convenient to extract it from CI coefficients,

$$C'_I = \exp\left(i\chi(t)\right) C_I\,. \tag{3.23}$$

Substituting Eq. (3.23) into Eq. (3.22) yields a new but physically equivalent CI equation of motion

$$i\dot{\tilde{C}}'_I = \sum_{J} \tilde{C}'_J \left\langle\tilde{I}\middle|\hat{H} - \hat{\mathcal{R}} - \dot{\chi}(t)\hat{I}\middle|\tilde{J}\right\rangle. \tag{3.24}$$

Eq. (3.24) constitutes the most general CI coefficient equation of motion governing the temporal evolution of CI coefficient valid for any choice of real phase $\chi(t)$. At this point however, we will defer further algebraic manipulation of Eq. (3.24) to Section 3.2.2 below and instead let's make a first move to derive the EOM governing the evolution of orbitals.

3.1.2 Orbital Equation of Motion

The second half of the system of EOM, namely the orbital EOM will be derived in this section. If we branched out from the $C_I^{(1)}$ part of Eq. (3.18) to obtain CI EOM, then, as one may guess, we shall now start from the $\hat{\mathcal{A}}$ part of the same equation to arrive at the desired orbital EOM. In the last paragraph before Section 3.1.1, it was mentioned that the minimum of TDVP functional must occur at arbitrary choice of $\hat{\mathcal{A}}$. Therefore, as the first step, we want to find a condition to be imposed on the $\hat{\mathcal{A}}$ part of Eq. (3.18) so that this equation is satisfied for arbitrary $\exp(-\epsilon\hat{\mathcal{A}})$. First, let's find a good description of what it means for this unitary operator to be arbitrary. Let's remember how $\hat{\mathcal{A}}$ was defined in Eq. (3.12) - it serves as the generator of a unitary transformation matrix $\exp\{(-\epsilon\hat{\mathcal{A}})\}$ *acting on determinants*, i.e. $\exp\{(-\epsilon\hat{\mathcal{A}})\}$ acts on the N-electron Fock space, and it is anti-hermitian. Since inside each determinant, these N orbitals are connected by ordinary multiplication, we can stipulate the arbitrary unitary transform to be performed on each of these orbitals

$$\exp\{(-\epsilon\hat{\mathcal{A}})\} = \prod_{i=1}^{N} \exp\left(-\epsilon\hat{A}(i)\right) = \exp\left(-\epsilon\sum_{i=1}^{N}\hat{A}(i)\right)$$

where $\hat{A}(i)$ is an anti-hermitian operator acting on the Hilbert space of the i-th electron and $\left[\hat{A}(i), \hat{A}(j)\right] = 0$ for all i and j. The product in the middle expression is to be understood as tensor product between one-particle unitary operators. The last equality follows from the commutativity of $\hat{A}(i)$'s. The argument in the exponent turns out to be the usual sum of one-electron operators and we know how to transform it to the second quantized version. Thus, we have, for the unitary operator acting on determinants

$$\hat{\mathcal{A}} = \sum_{\mu,\nu} A_{\mu\nu}\hat{E}_\nu^\mu \tag{3.25}$$

Substituting Eq. (3.25) into the $\hat{\mathcal{A}}$ part of (3.18), one has

$$\begin{aligned}
&\int_{t_0}^{t} dt' \sum_{\mu,\nu} A_{\mu\nu}\langle(H - i\partial_t)\tilde{\Psi}|\hat{E}_\nu^\mu|\tilde{\Psi}\rangle \\
&\quad= \int_{t_0}^{t} dt' \sum_{\mu,\nu} A_{\mu\nu}\left\{\langle\tilde{\Psi}|H\hat{E}_\nu^\mu|\tilde{\Psi}\rangle - \sum_I \tilde{C}_I^*\langle\tilde{I}|\hat{\mathcal{R}}\hat{E}_\nu^\mu|\tilde{\Psi}\rangle + \sum_I i\dot{\tilde{C}}_I^*\langle\tilde{I}|\hat{E}_\nu^\mu|\tilde{\Psi}\rangle\right\} \\
&\quad= \int_{t_0}^{t} dt' \sum_{\mu,\nu} A_{\mu\nu}\left\{\langle\tilde{\Psi}|(H - \hat{\mathcal{R}})\hat{E}_\nu^\mu|\tilde{\Psi}\rangle + \sum_I i\dot{\tilde{C}}_I^*\langle\tilde{I}|\hat{E}_\nu^\mu|\tilde{\Psi}\rangle\right\},
\end{aligned}$$

where the second line follows from using Eq. (3.19) and the third line is obtained by using Eq. (3.13). The second term of the last line inside the curly bracket can further be simplified by substituting Eq. (3.24) for $i\dot{\tilde{C}}_I^*$, which after some algebra gives

$$\int_{t_0}^{t} dt' \sum_{\mu,\nu} A_{\mu\nu}\left(\langle\tilde{\Psi}|(H - \hat{\mathcal{R}})(\mathcal{I} - \hat{\Pi})\hat{E}_\nu^\mu|\tilde{\Psi}\rangle + \left\langle\tilde{\Psi}\middle|\hat{E}_\nu^\mu\middle|\tilde{\Psi}\right\rangle\dot{\chi}(t)\right) = 0 \tag{3.26}$$

with $\mathcal{I}$ denoting identity operator and $\hat{\Pi} = \sum_I |\tilde{I}\rangle\langle\tilde{I}|$ the projection operator to the Fock space spanned by determinants included in the linear expansion of the wave function.

Let's not forget that the last equation obtained above was derived by working on the second term only in Eq. (3.17). As has been noted before, the expression that would have resulted if we picked the first term is just the complex conjugate of the left side of Eq. (3.26), adding this to (3.26) and after some rearrangements yields the orbital part of Eq. (3.17),

$$\int_{t_0}^{t} dt' \sum_{\mu,\nu} A_{\mu\nu}\left\{\langle\tilde{\Psi}|(H - \hat{\mathcal{R}})\hat{Q}\hat{E}_\nu^\mu|\tilde{\Psi}\rangle - \langle\tilde{\Psi}|\hat{E}_\nu^\mu\hat{Q}(H - \hat{\mathcal{R}})|\tilde{\Psi}\rangle\right\} = 0$$

where we have made use of the anti-hermiticity property of $\hat{\mathcal{A}}$ and defined $\hat{Q} = \hat{I} - \hat{\Pi}$. Note that the term containing $\dot{\chi}(t)$ is canceled out upon adding the complex conjugate of (3.26) - the optimized orbitals are independent of the choice of global phase. The arbitrariness of $A_{\mu\nu}$ requires

that the terms inside curly bracket be vanishing in order to satisfy the equation, hence giving us the sought orbital EOM,

$$\langle\tilde{\Psi}|H\hat{Q}\hat{E}^{\mu}_{\nu} - \hat{E}^{\mu}_{\nu}\hat{Q}H|\tilde{\Psi}\rangle = \langle\tilde{\Psi}|\hat{\mathcal{R}}\hat{Q}\hat{E}^{\mu}_{\nu} - \hat{E}^{\mu}_{\nu}\hat{Q}\hat{\mathcal{R}}|\tilde{\Psi}\rangle.$$

To sum up, in this section we have derived equations of motion which are to be satisfied by optimizing variational quantities in TD-MCSCF method, the CI coefficient and spatial orbital. For convenience, these equations are written down again below

TD-MCSCF Equations of Motion

$$i\dot{\tilde{C}}_I = \langle\tilde{I}|H - \hat{\mathcal{R}} - \dot{\chi}(t)\hat{I})|\tilde{\Psi}\rangle \tag{3.27a}$$

$$\langle\tilde{\Psi}|H\hat{Q}\hat{E}^{\mu}_{\nu} - \hat{E}^{\mu}_{\nu}\hat{Q}H|\tilde{\Psi}\rangle = \langle\tilde{\Psi}|\hat{\mathcal{R}}\hat{Q}\hat{E}^{\mu}_{\nu} - \hat{E}^{\mu}_{\nu}\hat{Q}\hat{\mathcal{R}}|\tilde{\Psi}\rangle. \tag{3.27b}$$

Eq. (3.27) above is general in the sense that they apply for general multi-determinantal method with any possible arbitrarily set requirements on the orbital occupations. They, for instance, serve as the starting equations in deriving orbital and CI coefficient differential equations both in TD-CASSCF and TD-ORMAS. The reader may have noticed that, even though multiple references such as "CI coefficient EOM" or "orbital EOM" have been made up to this point, none of them actually contain solely the quantity which they are referred to as. The CI EOM of Eq. (3.27a) also contains the unknown orbitals embodied inside $|\tilde{\Psi}\rangle$ and $|\tilde{I}\rangle$. Likewise, orbital EOM of Eq. (3.27b) also couples CI coefficients which are again contained in $|\tilde{\Psi}\rangle$. Eq. (3.27) therefore constitutes a system of coupled integro-differential equations satisfied by CI coefficients and orbitals which make the TDVP functional Eq. (3.9) stationary. The dependence of Eq. (3.27) on CI coefficient is explicit, the orbital dependency is however manifested through the presence of a compound creation and annihilation operators $\hat{E}^{\mu}_{\nu}$ where ν and μ are the references to spatial orbitals. This being the case however, in practice one does not actually directly solve these spatial orbitals, instead with the help of basis functions, one takes the time-dependent expansion coefficients associated with the chosen bases as the working variables. A discussion about the choice of bases is presented in Section 3.4.1.

3.2 TD-CASSCF Method

In the special case of TD-MCSCF where all possible configurations are included in the determinant bases, often referred to as *multiconfiguration time-dependent Hartree-Fock* (MCTDHF) method, the computation time scales factorially with respect to the number of electrons and orbitals. This obviously poses an upper limit in the size of the system to be simulated. An analog of *complete active space self-consistent field* (CASSCF) method [92–95], dubbed as time-dependent-CASSCF (TD-CASSCF), is developed for the purpose of alleviating the computational burden in MCTDHF without severely compromising the accuracy [63]. The idea behind TD-CASSCF lies in the varying degree of influence of the laser field with a given intensity on the orbitals of the atom. The deeper an orbital is bound (for instance, as quantified by the position of the radial global maximum), the lesser it will be distorted by an external field. Based on this behavior one may reasonably assume that the first few orbitals be doubly occupied as well as frozen in time. Such orbitals in TD-CASSCF are called *frozen core*. The capability of practically doing nothing to frozen orbitals is what constitute the main virtue of TD-CASSCF - it can save a significant computation time by propagating in time only a select orbitals, something that is absent in full MCTDHF. One degree less restrictive than frozen core, is the *dynamic core* where the orbital is doubly occupied but is allowed to vary in time. Dynamic core is the closer analogy with *core* orbitals in stationary CASSCF since the latter is iteratively optimized while maintaining double occupation. In obtaining the ground state wavefunction for the simulations in this research thesis by imaginary time relaxation (discussed later in Section 3.4.2), we set some of the deepest bound orbitals to be dynamic to let them be self-consistently optimized.

The highest orbitals, some of which contain valence electrons, can have arbitrary occupation n where $0 \leq n \leq 2$ and also be time-dependent, they are called *active orbital*. The dominant portion of electron correlation is expressed by the multiple rearrangements of electrons among these active orbitals. Strong-field dynamics such as tunnel-ionization and recombination are *role-played* mostly by active electrons provided numerical parameters such as radial size, radial grid density, and

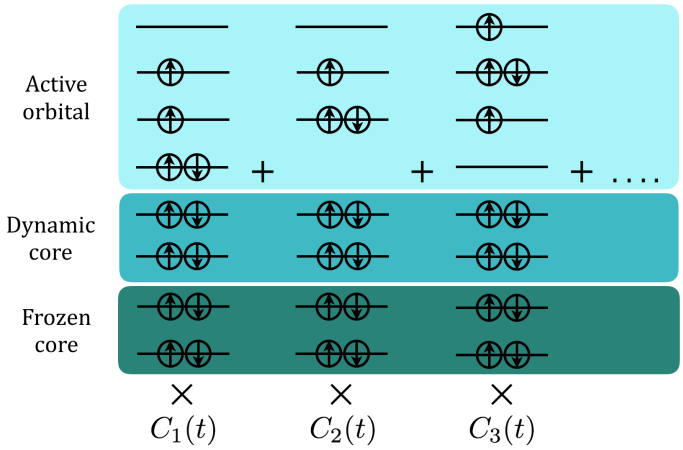

Figure 3.1: In TD-CASSCF, the orbitals are classified into frozen core, dynamic core, and active orbitals.

angular momenta are sufficiently specified in accordance with laser intensity and wavelength. For a given number of active orbitals and active electrons, all possible rearrangements of electrons are included as the basis to span the total wavefunction, hence giving its name 'complete active space'. To summarize, in TD-CASSCF we classify the spatial orbitals into three categories:

- *Frozen core*, where the orbital has a constant occupation of two and is also fixed in time.
- *Dynamic core*, where the orbital is also constantly doubly occupied but is time-dependent.
- *Active orbital*, where the occupation can be any number n with $0 \leq n \leq 2$ and is time-dependent.

As a matter of notational convention, from this point on we will adopt the following notations to distinguish orbitals from various orbital groups. We will use $\{i, j, k\}$ for core (frozen plus dynamic), $\{t, u, v\}$ for active orbitals, $\{a, b\}$ for virtual orbitals, $\{p, q\}$ for general occupied, and $\{\mu, \nu, \lambda, \gamma\}$ for general orbitals.

The orbital structure in TD-CASSCF method may schematically be depicted in Fig. 3.1. In this example, we assume an atom having 7 spin-up and 5 spin-down electrons occupying 8 orbitals. The first two orbitals have been set to frozen core and the next two to dynamic core. The remaining 4 electrons (3 spin-up and 1 spin-down) are allowed to occupy any of the four active orbitals. Each configuration is multiplied by a complex time-dependent configuration interaction coefficient. Our implementation of TD-CASSCF is restricted to spin-conserving interactions, such as dipole interaction with strong-field laser. This allows us to make the number of spin-up and spin-down electrons to be constant. The number of determinants resulting from rearrangements of active electrons among active orbitals is therefore given by the number of every possible pairing between spin-up configuration and spin down configuration, mathematically

$$N_{\text{det}} = \binom{n_a}{N_\alpha - N_c/2} \times \binom{n_a}{N_\beta - N_c/2}$$

where n_a, N_α, N_β, and N_c are the number of active orbitals, the number of spin-up, spin-down, and core (frozen plus dynamic) electrons, respectively. Configuration scheme in Fig. 3.1 gives $N_{\text{det}} = 4!/(1!3!) \times 4!/(3!1!) = 16$.

3.2.1 Redundant and Non-Redundant Orbital Rotations

It turns out that not all matrix elements of $\hat{R}$ appearing as unknowns in Eq. (3.27) are essential for the evolution of the wavefunction. This can be understood upon using Eq. (3.22) to substitute $\dot{\tilde{C}}_i$ in (3.19) to obtain

$$|i\partial_t \Psi\rangle = \hat{\Pi}\hat{H}|\Psi\rangle + \hat{Q}\hat{\mathcal{R}}|\Psi\rangle \tag{3.28}$$

and expanding $\hat{\mathcal{R}}$ in the following way

$$\hat{\mathcal{R}} = \sum_{(\mu,\nu)\,\in\,\text{red}} R_{\mu\nu}\hat{E}^{\mu}_{\nu} + \sum_{(\mu,\nu)\,\in\,\text{non-red}} R_{\mu\nu}\hat{E}^{\mu}_{\nu} \tag{3.29}$$

where

$$\sum_{(\mu,\nu)\,\in\,\text{red}} R_{\mu\nu}\hat{E}^{\mu}_{\nu} = \sum_{i,j} R_{ij}\hat{E}^{i}_{j} + \sum_{t,u} R_{tu}\hat{E}^{t}_{u} + \sum_{a,b} R_{ab}\hat{E}^{a}_{b} \tag{3.30a}$$

$$\sum_{(\mu,\nu)\,\in\,\text{non-red}} R_{\mu\nu}\hat{E}^{\mu}_{\nu} = \sum_{i,t}(R_{it}\hat{E}^{i}_{t} + R_{ti}\hat{E}^{t}_{i}) + \sum_{i,a}(R_{ia}\hat{E}^{i}_{a} + R_{ai}\hat{E}^{a}_{i}) + \sum_{t,a}(R_{ta}\hat{E}^{t}_{a} + R_{at}\hat{E}^{a}_{t}). \tag{3.30b}$$

The sums over the red (for 'redundant') pairs involves only rotations within the same orbital subspace whereas those over non-red contain rotations between different orbital subspaces. The action of $\hat{Q}$ on $\hat{E}^{\mu}_{\nu}$ with $(\mu,\nu) \in$ red yields zero because $\hat{E}^{\mu}_{\nu}|\Psi\rangle$ always gives a state living in $\hat{\Pi}$ subspace, the orthogonal complement of $\hat{Q}$. On the other hand, if $(\mu,\nu) \in$ non-red, i.e. when μ and ν belong to different orbital subspaces, then $\hat{Q}\hat{E}^{\mu}_{\nu}|\Psi\rangle = \hat{E}^{\mu}_{\nu}|\Psi\rangle$ since $\hat{E}^{\mu}_{\nu}$ brings every single determinant in $|\Psi\rangle$ into $\hat{Q}$. The projection operator $\hat{Q}$ effectively filters out the contribution from redundant matrix elements in $\hat{R}$. This arbitrariness gives us freedom in defining matrix elements of $\hat{R}$ between the same orbital subspace - these elements can be chosen to be the elements of arbitrary Hermitian matrix $\hat{\theta}(t)$,

$$R_{\mu\nu} = \theta_{\mu\nu} \qquad (\mu,\nu) \in \text{red}.$$

While the non-redundant elements of $\hat{R}$ must of course be solved through Eq. (3.27a) and (3.27b).

Despite arbitrary, the choice of redundant elements of $\hat{R}$ may affect the stability of the time propagation algorithm. In our TD-MCSCF program, we employ two choices of Hermitian matrix representing the redundant elements of $\hat{R}$,

$$\hat{\theta}(t) = 0$$

and

$$\hat{\theta}(t) = \hat{h}.$$

It is known that the choice of redundant elements of $\hat{R}$ can affect the stability of the propagation [62]. All simulation results presented in this dissertation used the first type of redundant hermitian matrix. Along with the choice of global phase (see Section 3.2.2), the choice of redundant elements of $\hat{R}$ modify the form of CI equation of motion, the discussion of which will be covered in the next section.

3.2.2 TD-CASSCF Equation of Motion for CI Coefficients - The Choice of Global Phase and Redundant Matrix Elements

The most general form of CI equation of motion applicable for any TD-MCSCF method and the choice of global phase as well as redundant matrix elements is given by Eq. (3.27a). But we have not taken advantage of the freedom in choosing the global phase and redundant matrix elements of $\hat{R}$. In this section, we shall employ this freedom in order to cast Eq. (3.27a) into a more explicit form.

As is well-known, the wavefunction of a quantum system is arbitrary up to a global phase factor. Indeed, multiplying the wavefunction with a global phase that is independent of space but can be time-dependent leaves expectation values invariant. Despite theoretically unimportant, the choice of global phase can be exploited in the framework of TD-MCSCF method, e.g. to obtain a slowly oscillating wavefunction which otherwise potentially requires very fine time step, especially when the active space is large [63]. Note that, making a change such as

$$|\Psi'\rangle = \exp\left(i\chi(t)\right)|\Psi\rangle \tag{3.32}$$

where $\chi(t)$ is a scalar real function, does not change the structure of functional (3.9). It is easily shown that

$$S[\Psi'] = S[\Psi] + \chi(t) - \chi(t_0),$$

that is, if Ψ minimizes TD-MCSCF functional (3.9), then so does any other wavefunction connected by Eq. (3.32) with Ψ. The multiplication of wavefunction with a phase factor corresponds to the appearance of an additional term proportional to $\dot{\chi}(t)$) in the CI equation of motion

$$i\dot{C}_I = \sum_J C_J \langle I|H - \hat{\mathcal{R}} - \dot{\chi}(t)\hat{I})|J\rangle. \tag{3.33}$$

By invoking the results from Appendix B, we can explicitly express the matrix element of Hamiltonian in terms of the elements of density matrices,

$$\begin{aligned}
\langle I|\hat{H}|J\rangle &= \sum_{\mu,\nu} h_{\mu\nu} (D_{IJ})^{\nu}_{\mu} + \frac{1}{2} \sum_{\mu,\nu,\lambda,\gamma} U_{\mu\nu,\lambda\gamma} (P_{IJ})^{\lambda\gamma}_{\mu\nu} \\
&= \delta_{IJ} \left(2 \sum_i h_{ii} + \sum_{i,j} \left(2U_{ij,ij} - U_{ij,ji} \right) \right) + \sum_{t,u} h_{tu} (D_{IJ})^{u}_{t} + \dots \\
&\quad \sum_{t,u} \sum_i \left(2U_{it,iu} - U_{it,ui} \right) (D_{IJ})^{u}_{t} + \frac{1}{2} \sum_{t,u,v,w} (P_{IJ})^{tu}_{vw} U_{vw,tu} \\
&= \delta_{IJ} \sum_i (h_{ii} + f_{ii}) + \sum_{t,u} f_{tu} (D_{IJ})^{u}_{t} + \frac{1}{2} \sum_{t,u,v,w} (P_{IJ})^{tu}_{vw} U_{vw,tu} \\
&= H^C_{IJ} + H^A_{IJ}
\end{aligned} \tag{3.34}$$

where we have defined $(D_{IJ})^{\nu}_{\mu} = \langle I|\hat{E}^{\mu}_{\nu}|J\rangle$ and $(P_{IJ})^{\lambda\gamma}_{\mu\nu} = \langle I|\hat{E}^{\mu\nu}_{\lambda\gamma}|J\rangle$ and

$$H^C_{IJ} = \delta_{IJ} \sum_i (h_{ii} + f_{ii}) \tag{3.35a}$$

$$H^A_{IJ} = \sum_{t,u} f_{tu} (D_{IJ})^{u}_{t} + \frac{1}{2} \sum_{t,u,v,w} (P_{IJ})^{tu}_{vw} U_{vw,tu} \tag{3.35b}$$

$$\hat{f} = \hat{h} + \sum_i^{\text{f.c.+d.c.}} \left(2\hat{\mathcal{J}}^i_i - \hat{\mathcal{K}}^i_i \right) \tag{3.35c}$$

$$\mathcal{J}^{\mu}_{\nu}(\mathbf{r}) = \int d^3\mathbf{r}' \frac{\phi^*_{\mu}(\mathbf{r}')\phi_{\nu}(\mathbf{r}')}{|\mathbf{r} - \mathbf{r}'|} \tag{3.35d}$$

$$\mathcal{K}^{\mu}_{\nu}(\mathbf{r})\phi_{\gamma}(\mathbf{r}) = \int d^3\mathbf{r}' \frac{\phi^*_{\mu}(\mathbf{r}')\phi_{\gamma}(\mathbf{r}')}{|\mathbf{r} - \mathbf{r}'|} \phi_{\nu}(\mathbf{r}). \tag{3.35e}$$

In order to evaluate $\langle I|\hat{\mathcal{R}}|J\rangle$, we make use of the separation of $\hat{\mathcal{R}}$ into redundant and non-redundant parts (see Eq. (3.30)) and the fact that projection by $\langle I|$ filters out the non-redundant part,

$$\mathcal{R}_{IJ} = \sum_{(\mu,\nu) \in \text{red}} \theta_{\mu\nu} (D_{IJ})^{\nu}_{\mu} .$$

Having obtained the explicit expression of operators appearing in Eq. (3.27a), we may now proceed by considering various forms of CI equation of motion based on the choices for $\chi(t)$ and $\hat{\theta}(t)$.

Case 1: $\chi(t) = \chi$ **and** $\hat{\theta}(t) = 0$

In this most obvious and simplest case, we have

$$i\dot{C}_I = \sum_J C_J \left(H^C_{IJ} + H^A_{IJ} \right).$$

Case 2: $\chi(t) = 0$ **and** $\hat{\theta}(t) = \hat{h}$

Since the one-particle part of $\langle I|\hat{H}|J\rangle$ also contains rotations between the same orbital subspace as $\mathcal{R}_{IJ}$ does, these two quantities will cancel each other leaving only the electron-electron potential,

$$i\dot{C}_I = \sum_J C_J \langle I|\hat{U}|J\rangle$$

where

$$\langle I|\hat{U}|J\rangle = \delta_{IJ}\sum_{i,j}\left\{2\left(\mathcal{J}_j^j\right)_{ii} - \left(\mathcal{K}_j^j\right)_{ii}\right\} + \sum_{t,u}\sum_{j}\left\{2\left(\mathcal{J}_j^j\right)_{tu} - \left(\mathcal{K}_j^j\right)_{tu}\right\}(D_{IJ})_t^u + \ldots$$
$$\frac{1}{2}\sum_{t,u,v,w}(P_{IJ})_{vw}^{tu}\,U_{vw,tu}.$$

Case 3: $\chi(t) = \int^t \mathrm{d}t'\,E(t')$ **and** $\hat{\theta}(t) = 0$

By choosing $\dot{\chi}(t) = E(t) = \langle\Psi|\hat{H}|\Psi\rangle$, we find that the propagation can run with a coarser time step. In order to evaluate $E(t)$, we proceed in a similar way as when arriving at Eq. (3.34).

$$E(t) = \left\langle\tilde{\Psi}\middle|\hat{H}\middle|\tilde{\Psi}\right\rangle = E^C + E^A \tag{3.36}$$

where we have defined one-electron reduced density matrix (1RDM) $D_\mu^\nu = \left\langle\tilde{\Psi}\middle|\hat{E}_\nu^\mu\middle|\tilde{\Psi}\right\rangle$ and two-electron reduced density matrix (2RDM) $P_{\mu\nu}^{\lambda\gamma} = \left\langle\tilde{\Psi}\middle|\hat{E}_{\lambda\gamma}^{\mu\nu}\middle|\tilde{\Psi}\right\rangle$ and

$$E^C = \sum_i (h_{ii} + f_{ii}),$$
$$E^A = \sum_{t,u} f_{tu}D_t^u + \frac{1}{2}\sum_{t,u,v,w}P_{vw}^{tu}U_{vw,tu}$$

Then using Eq. (3.34) and (3.36) in Eq. (3.33), we arrive at

$$i\dot{C}_I = \sum_J\left(H_{IJ}^A - \delta_{IJ}E^A\right)C_J.$$

The three forms of CI coefficient equation of motions (among many others) presented above may look quite different one from another. Nevertheless, we would like to stress again, all of them actually correspond to the same observables evaluated with respect to the optimized wavefunction. The different choices of global phase and redundant elements of $\hat{R}$ have their effect in the numerical aspect of the method. For instance, we have found that sometimes taking $E(t)$ as $\dot{\chi}(t)$ (Case 3) enables propagation with a longer time step whereas the choice of $\hat{\theta} = \hat{h}$ makes the numerical implementation of split operator propagation method easier.

3.2.3 TD-CASSCF Equations of Motion for Orbitals

Our goal in this section is to derive the differential equations satisfied by the time-dependent orbitals and CI coefficients in TD-CASSCF method. For a general time-dependent orbitals (i.e. frozen core excluded), supposing that the first time derivative of the orbital to be also a vector in the same one-particle Hilbert space as the orbitals, we take the differential equation governing the time-dependent orbitals to be the following relation

$$|i\partial_t\phi_\mu\rangle = \sum_\nu|\phi_\nu\rangle\langle\phi_\nu|\hat{R}|\phi_\mu\rangle.$$

Hence, the aforementioned task is equivalent to finding the non-redundant matrix elements $R_{\mu\nu}$. The redundant ones can be taken to be the elements an arbitrary Hermitian matrix.

As was pointed out at the end of of Section 3.1.2, in order to derive equations of motion for TD-CASSCF method we start from Eq. (3.27). In order to proceed with the derivation, let's work on Eq. (3.27b) so that we get an equation where the various matrix elements of $\hat{h}$, $\hat{U}$, and $\hat{R}$ are explicitly shown. First, note that Eq. (3.27b) can be cast into

$$\langle\tilde{\Psi}|\hat{U}\hat{Q}\hat{E}_\nu^\mu - \hat{E}_\nu^\mu\hat{Q}\hat{U}|\tilde{\Psi}\rangle = -\langle\tilde{\Psi}|\bar{h}\hat{Q}\hat{E}_\nu^\mu - \hat{E}_\nu^\mu\hat{Q}\bar{h}|\tilde{\Psi}\rangle.$$

with

$$\bar{h} = \sum_{\gamma,\lambda}\left(h_{\gamma\lambda} - R_{\gamma\lambda}\right)\hat{E}_\lambda^\gamma$$
$$\hat{U} = \frac{1}{2}\sum_{\mu,\nu,\lambda,\gamma}U_{\mu\nu,\lambda\gamma}\hat{E}_{\lambda\gamma}^{\mu\nu}.$$

The presence of a series of operator such as $\hat{Q}\bar{h}$ suggests that we should expand $\bar{h}$ in the same way as $\hat{\mathcal{R}}$ is in Eq. (3.29) and (3.30). Within the same reason as outlined following Eq. (3.30), the sums over (γ, λ) pairs within the same orbital subspace vanishes while those between different subspaces remain. This yields

$$\begin{aligned}
\langle\tilde{\Psi}|\hat{U}\hat{Q}\hat{E}^{\mu}_{\nu} - \hat{E}^{\mu}_{\nu}\hat{Q}\hat{U}|\tilde{\Psi}\rangle &= \sum_{(\gamma,\lambda)\,\in\,\text{non-red}} \bar{h}_{\gamma\lambda}\langle\tilde{\Psi}|[\hat{E}^{\mu}_{\nu}, \hat{E}^{\gamma}_{\lambda}]|\tilde{\Psi}\rangle \\
\langle\tilde{\Psi}|\hat{U}\hat{Q}\hat{E}^{\mu}_{\nu} - \hat{E}^{\mu}_{\nu}\hat{Q}\hat{U}|\tilde{\Psi}\rangle &= \sum_{(\gamma,\lambda)\,\in\,\text{non-red}} \bar{h}_{\gamma\lambda}\langle\tilde{\Psi}| - \delta_{\mu\lambda}\hat{E}^{\gamma}_{\nu} + \delta_{\gamma\nu}\hat{E}^{\mu}_{\lambda}|\tilde{\Psi}\rangle.
\end{aligned} \tag{3.38}$$

where we have used a commutator identity in Appendix A. Keep in mind that for any given term constituting the sum in the right side, ϕ_γ and ϕ_λ belong to different orbital spaces. Because of this, when both ϕ_μ and ϕ_ν belong to the same orbital subspace, the non-vanishing $\delta_{\mu\lambda}$ occurs when ϕ_λ is in the same space as ϕ_μ and ϕ_ν. But since ϕ_γ is in a different space from ϕ_λ, which is itself in the same space as ϕ_ν, $\hat{E}^{\gamma}_{\nu}$ will bring the wavefunction outside $\hat{\Pi}$ and thus $\langle\tilde{\Psi}|\hat{E}^{\gamma}_{\nu}|\tilde{\Psi}\rangle = 0$. By the same token, the term containing $\delta_{\gamma\nu}$ also vanishes if ϕ_μ and ϕ_ν belong to the same orbital space.

As for the left side of Eq. (3.38), the presence of a sequence of operators such as $\hat{Q}\hat{E}^{\mu}_{\nu}$ makes it obvious that it will also equal zero if ϕ_μ and ϕ_ν belong to the same orbital space. Long story short, Eq. (3.38) reduces to an identity $0 = 0$ when ϕ_μ and ϕ_ν belong to the same orbital space and thus we need only consider the cases where they are in different orbital spaces due to which operator $\hat{Q}$ can be dropped from the left side of Eq. (3.38),

$$\frac{1}{2}\sum_{\mu',\nu',\lambda',\gamma'} U_{\mu'\nu',\lambda'\gamma'}\langle\tilde{\Psi}|[\hat{E}^{\mu'\nu'}_{\lambda'\gamma'}, \hat{E}^{\mu}_{\nu}]|\tilde{\Psi}\rangle = -\sum_{\gamma}\bar{h}_{\gamma\mu}D^{\nu}_{\gamma} + \sum_{\lambda}\bar{h}_{\nu\lambda}D^{\lambda}_{\mu} \tag{3.39}$$

where $D^{\mu}_{\nu} = \langle\tilde{\Psi}|\hat{E}^{\nu}_{\mu}|\tilde{\Psi}\rangle$ and *with the conditions such that the first sum on the right runs over orbitals in different subspace as ϕ_μ and the second sum runs over orbitals in different subspace as ϕ_ν*. In arriving at Eq. (3.39), we made use of commutator properties in Appendix A. Working on the commutator in the left side of Eq. (3.39) using these commutator identities and performing the necessary algebra, one obtain the following equation which we will use as the starting equation to get the expression of various non-redundant elements of $\hat{R}$,

$$-\sum_{\nu',\lambda',\gamma'} U_{\nu\nu',\lambda'\gamma'}P^{\lambda'\gamma'}_{\mu\nu'} + \sum_{\mu',\nu',\lambda'} U_{\mu'\nu',\lambda'\mu}P^{\lambda'\nu}_{\mu'\nu'} = -\sum_{\gamma}\bar{h}_{\gamma\mu}D^{\nu}_{\gamma} + \sum_{\lambda}\bar{h}_{\nu\lambda}D^{\lambda}_{\mu} \tag{3.40}$$

where $P^{\mu\nu}_{\lambda\gamma} = \langle\tilde{\Psi}|\hat{E}^{\lambda\gamma}_{\mu\nu}|\tilde{\Psi}\rangle$. For various non-redundant pairs (μ, ν)), Eq. (3.40) constitutes a system of linear equations to be solved for $R_{\mu\nu}$ where ϕ_μ resides in a different orbital subspace as ϕ_ν.

As a short remark, notice that the one-particle part $\hat{h}$ of the Hamiltonian appears symmetrically as $\hat{R}$ which implies that only those elements of $\hat{h}$ between orbitals from different subspaces appear in Eq. (3.40). It may be tempting to conclude from this that the elements of $\hat{h}$ within the same subspace to be also redundant, i.e. can be chosen arbitrarily. This is, however, not true because these elements appear in the expression of the first time derivative of the total wavefunction (see Eq. (3.28)). These elements are needed in calculating the time-dependent CI coefficients. We therefore would like to emphasize that the redundancies of whatever elements of a matrix should better be judged from the evolution of the total wavefunction, i.e. (3.28). Below we will derive $R_{\mu\nu}$ for various non-redundant pairs (μ, ν). Given the hermiticity of $\hat{R}$, we will be dealing with only four kinds of non-redundant matrix element.

Case 1: when $\mu = a$ and $\nu = i$ (d.c.)

When ϕ_μ is a virtual orbital, the first sum in the right side of (3.40) must run over core and active orbitals. With $\nu = i$, this range is narrowed down to core only because $D^{i}_{t} = 0$. The core block of $\hat{D}$ matrix is diagonal, i.e. $D^{i}_{j} = 2\delta_{ij}$, thus

$$-\sum_{\gamma}\bar{h}_{\gamma a}D^{i}_{\gamma} = -2\bar{h}_{ia} = 2\left(R_{ia} - h_{ia}\right). \tag{3.41}$$

The second term in the right side of (3.40) vanishes because $D^{\gamma}_{a} = 0$. For the left side of (3.40), using the result from Appendix B we have

$$\sum_{k,l,j} P^{ji}_{kl} U_{kl,ja} + \sum_{u,j,t} P^{ti}_{uj} U_{uj,ta} + \sum_{j,u,t} P^{ti}_{ju} U_{ju,ta} = 2 \sum_{j}^{\text{f.c.+d.c.}} \left(2(\mathcal{J}^{j}_{j})_{ia} - (\mathcal{K}^{j}_{j})_{ia} \right) + \dots$$
$$\sum_{u,t} D^{t}_{u} \left(2(\mathcal{J}^{u}_{t})_{ia} - (\mathcal{K}^{u}_{t})_{ia} \right) \tag{3.42}$$

Combining Eq. (3.41) and (3.42) and defining an operator $\hat{\mathcal{G}}$ as

$$\hat{\mathcal{G}} = \sum_{u,t} D^{t}_{u} \left(2\hat{\mathcal{J}}^{u}_{t} - \hat{\mathcal{K}}^{u}_{t} \right), \tag{3.43}$$

gives us the matrix element of $\hat{R}$ between core and virtual orbitals,

$$R_{ia} = f_{ia} + \frac{1}{2} \mathcal{G}_{ia} \qquad i \in \text{d.c.}$$

where $\hat{f}$ is given by Eq. (3.35c). Owing to the hermiticity of $\hat{f}$ and $\hat{\mathcal{G}}$, one has

$$R_{ai} = R^{*}_{ia} = f_{ai} + \frac{1}{2} \mathcal{G}_{ai} \qquad i \in \text{d.c.}.$$

Case 2: when $\mu = a$ and $\nu = t$

Like Case 1, here we still have the second sum on the right side of Eq. (3.40) zero because of annihilation on a virtual orbital, leaving the first sum only

$$- \sum_{u} D^{t}_{u} \bar{h}_{ua}. \tag{3.45}$$

The left side gives

$$\sum_{j,u,i} P^{it}_{ju} U_{ju,ia} + \sum_{u,j,i} P^{it}_{uj} U_{uj,ia} + \sum_{v,w,u} P^{ut}_{vw} U_{vw,ua} = \dots$$
$$\sum_{u} D^{t}_{u} \sum_{j}^{\text{f.c.+d.c.}} \left(2(\mathcal{J}^{j}_{j})_{ua} - (\mathcal{K}^{j}_{j})_{ua} \right) + \mathcal{L}_{ta} \tag{3.46}$$

where we have defined an operator $\hat{\mathcal{L}}$ such that

$$\mathcal{L}_{\lambda\gamma} = \sum_{v,w,u} P^{\lambda u}_{wv} \left(\mathcal{J}^{v}_{u} \right)_{w\gamma}$$
$$\left(\mathcal{L}^{\dagger} \right)_{\lambda\gamma} = \sum_{v,w,u} \left(\mathcal{J}^{u}_{v} \right)_{\gamma w} P^{vw}_{u\lambda}$$

Combining Eq. (3.45) and (3.46) yields the matrix element of $\hat{R}$ between active and virtual orbitals

$$R_{ta} = f_{ta} + \sum_{x} (D^{-1})^{t}_{x} \mathcal{L}_{xa}$$

whose complex conjugate is

$$R_{at} = f_{at} + \sum_{x} \left(\mathcal{L}^{\dagger} \right)_{ax} \left(D^{-1} \right)^{x}_{t}$$

Note that this time, the determination of matrix element of $\hat{R}$ involves an inverse operation. This, in fact, can become the source of failure during ORMAS imaginary time relaxation for calculating ground state. In the numerical implementation of this inversion, the eigenvalues of 1RDM are first calculated followed by inversion of the diagonal elements by adding some small regularization parameter in the denominator to avoid singularity. In the event when even after setting a reasonably big value for the regularization parameter, the propagation still fails, that is usually an indication of unsuitable choice of orbital subspace division applied to the problem at hand.

Case 3: when $\mu = i$ (d.c.) and $\nu = t$

This time both sums on the right side of (3.40) are nonvanishing because neither μ nor ν is virtual,

$$\sum_u \bar{h}_{ui} \left(2\delta_{tu} - D^t_u\right)$$

The left side also contains more terms,

$$-\sum_{j,k,l} P^{kl}_{ij} U_{tj,kl} - \sum_{u,w,j} P^{wj}_{iu} U_{tu,wj} - \sum_{u,j,w} P^{jw}_{iu} U_{tu,jw} + \ldots$$
$$\sum_{k,u,j} P^{jt}_{ku} U_{ku,ji} + \sum_{u,k,j} P^{jt}_{uk} U_{uk,ji} + \sum_{v,w,u} P^{ut}_{vw} U_{vw,ui} =$$
$$-\sum_u \left(2\delta_{tu} - D^t_u\right) \sum_j^{\text{f.c.+d.c.}} \left(2(\mathcal{J}^j_j)_{ti} - (\mathcal{K}^j_j)_{ti}\right) - \sum_{u,w} D^w_u \left(2(\mathcal{J}^u_w)_{ti} - (\mathcal{K}^u_w)_{ti}\right) + \mathcal{L}_{ti}$$

Finally, R_{ti} and its complex conjugate are given by

$$R_{ti} = f_{ti} + \sum_x \left(\bar{D}^{-1}\right)^t_x (\mathcal{G}_{xi} - \mathcal{L}_{xi}) \tag{3.48a}$$

$$R_{it} = R^*_{ti} = f_{it} + \sum_x \left(\mathcal{G}_{ix} - \left(\mathcal{L}^\dagger\right)_{ix}\right) \left(\bar{D}^{-1}\right)^x_t \tag{3.48b}$$

where $\bar{D}^t_u = 2\delta_{tu} - D^t_u$. Like Case 2, an inversion is required here and regularization method is also employed to calculate the inverse.

Case 4: either μ or ν is frozen core

In all previous cases, the core orbital being considered is a dynamic core. For matrix element of R involving frozen core, a different treatment is required. The frozen orbitals are not among the variational quantities since their values are predetermined throughout the simulation. Mathematically, this means the matrix elements of R involving frozen orbitals are not solution of Eq. (3.40). In the implementation of TD-CASSCF used in this dissertation, we define frozen orbitals the following way

Time evolution of TD-CASSCF frozen orbitals

$$\phi_i(\mathbf{r}, t) = \begin{cases} \phi_i(\mathbf{r}), & \text{length gauge} \\ e^{-izA(t)}\phi_i(\mathbf{r}), & \text{velocity gauge.} \end{cases} \tag{3.49}$$

Therefore

$$R_{\mu i} = \begin{cases} 0, & \text{length gauge} \\ E(t) \left\langle \phi_\mu \middle| z \middle| \phi_i \right\rangle, & \text{velocity gauge} \end{cases}$$

where ϕ_i is a frozen orbital while ϕ_μ is either active or virtual and $R_{i\mu} = R^*_{\mu i}$.

Having derived the expression for various non-redundant matrix elements of $\hat{R}$, we now have all the necessary parts to construct the equations of motion that couple orbitals in a nonlinear manner. For dynamic cores this equation looks like

Time evolution of TD-CASSCF dynamic orbitals

$$\begin{aligned} |i\partial_t \phi_i\rangle &= \sum_\nu |\phi_\nu\rangle\langle\phi_\nu|\hat{R}|\phi_i\rangle \\ &= \sum_j \theta_{ji} \left|\phi_j\right\rangle + \sum_t R_{ti} \left|\phi_t\right\rangle + \hat{q}\left(\hat{f} + \frac{1}{2}\hat{\mathcal{G}}\right)|\phi_i\rangle \end{aligned} \tag{3.50}$$

with R_{ti}, $\hat{f}$, and $\hat{G}$ are given by Eq. (3.48a), (3.35c), and (3.43), respectively. $\hat{q} = \hat{I} - \sum_p |\phi_p\rangle\langle\phi_p|$ is a projector to virtual space. Similarly for the derivative of active orbital

Time evolution of TD-CASSCF active orbitals

$$|i\partial_t \phi_t\rangle = \sum_j R_{jt} |\phi_j\rangle + \sum_u \theta_{ut} |\phi_u\rangle + \hat{q}\left(\hat{f} + \hat{\mathcal{Y}}\right)|\phi_t\rangle \tag{3.51}$$

with R_{jt} and $\hat{f}$ are given by Eq. (3.48b) and (3.35c) and an operator $\hat{\mathcal{Y}}$ is defined such that

$$\mathcal{Y}_{\lambda\gamma} = \sum_t \left(\mathscr{L}^\dagger\right)_{\lambda t} \left(D^{-1}\right)^t_\gamma .$$

For a given choice of redundant matrix elements $\hat{\theta}$ and global phase $\chi(t)$, Eq. (3.33), (3.50), and (3.51) represent a system of nonlinearly coupled differential equations to be solved for CI coefficients and time-dependent orbitals which, when brought together according Eq. (3.3) to form the wavefunction, will minimize the functional (3.9). A wavefunction obtained in this way is used to calculate various observables in this dissertation such as dipole moment, velocity, and acceleration (see Section 3.5 below) as well as to perform related anaylises. In the next section, the underlying concept of TD-ORMAS, a cheaper alternative to TD-CASSCF, will be outlined.

3.3 TD-ORMAS Method

TD-CASSCF method presented in Section 3.2 is a powerful method for dealing with many electron systems. This method is efficient yet can be as accurate as the full MCTDHF provided appropriate division of orbital space s carried out (as will be shown in Section 4.2.2). Even so, the number of determinants grows in the same way with respect to n_a and N_a as that in MCTDHF does with n and N. Freezing n_c orbitals virtually reduces the number of orbitals by that amount but the way the electrons are redistributed is just the same as MCTDHF. This can result in a prohibitively long computational time as well as large memory requirement if one has large number of ways to rearrange active electrons.

In the present section, we will discuss another variant of TD-MCSCF which further takes advantage of the choice in prescribing orbital occupations beyond restricting double occupation one can do in TD-CASSCF. Given that the rate of excitation should be proportional to the laser intensity, it sounds reasonable to assume that the higher an orbital is, the less chance it will populated during laser interaction. Hence, it may be a good approximation to set a maximum occupation for a particular shell nl lower than the number it can accommodate, which is $4(l+1)$. This is the basic idea underlying time-dependent occupation-restricted multiple-active-space or TD-ORMAS method [65], which had also been developed for stationary state calculation [96, 97].

In TD-ORMAS one further subdivides the active space into several groups and specify both maximum and minimum numbers of electrons that can occupay each active subgroup. Mathematically, assuming one has G active subgroups TD-ORMAS active space structure is illustrated the following way

$$\mathcal{A} = \bigoplus_{g=1}^{G} \mathcal{A}_g$$

where to each subgroup $\mathcal{A}_g$ is associated the number of orbitals n_g, satisfying $\sum_{g=1}^{G} n_g = n_a$. Each subgroup g can only accomodate no more than $N_g^{\max}$ and no less than $N_g^{\min}$ electrons,

$$\begin{aligned} N_1^{\min} \leq & N_1 \leq N_1^{\max} \\ N_2^{\min} \leq & N_2 \leq N_2^{\max} \\ & \vdots \\ N_G^{\min} \leq & N_G \leq N_G^{\max} \end{aligned}$$

with

$$\sum_{g=1}^{G} N_g = N_A .$$

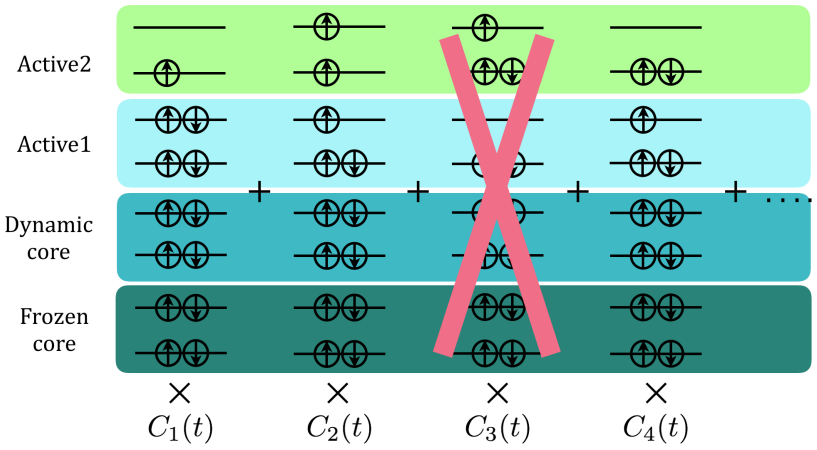

Figure 3.2: As in TD-CASSCF, in TD-ORMAS the orbitals are divided into frozen core, dynamic core, and active orbital. The difference is that in TD-ORMAS, active orbitals set can be further divided into several active subgroups, each of which can accommodate a range of electron occupations set by the user.

Without frozen cores, the determinants $|I\rangle$ to be included to represent the wavefunction (see Eq. (3.3)) are therefore those whose occupation number satifies

$$\sum_{\mu \in g} \langle I|\hat{E}^{\mu}_{\mu}|I\rangle = N_g, \qquad 1 \leq g \leq G. \tag{3.52}$$

With frozen cores, the conditions

$$\langle I|\hat{E}^{\mu}_{\mu}|I\rangle = 2 \qquad \phi_\mu \in \text{frozen orbitals}$$

must be added to TD-ORMAS condition (3.52). Such restriction in active space structure can yield a drastically smaller number of determinants than there are in TD-CASSCF. In fact, TD-CASSCF is just one special case of TD-ORMAS for which $G = 1$ and $N_1^{\min} = N_1^{\max} = N_A$.

As an example, consider an atom having 13 electrons distributed among 8 orbitals as shown in Fig. 3.2, where the active orbitals are divided into to groups Active1 and Active2. If we require the following conditions on the occupations of Active1 and Active2:

$$\begin{aligned} N_1^{\min} &= 3; & N_1^{\max} &= 4 \\ N_2^{\min} &= 1; & N_2^{\max} &= 2 \end{aligned}$$

then, for instance, the third configuration must be rejected because it has 2 electrons in Active1 and 3 electrons in Active2. In practice, to be as physically reasonable as possible the number of electrons should become smaller and smaller as one goes to higher active subgroups. In the following section, we will derive the equations of motion for orbitals and CI coefficients in TD-ORMAS.

3.3.1 TD-ORMAS Equations of Motions

As in the case of TD-CASSCF, in order to solve for the time evolution of orbitals and CI coefficients in the framework of TD-ORMAS, one must obtain the equations of motion governing these quantities. Conceptually, there is no big differences in the mathematical structure between TD-ORMAS and TD-CASSCF. The underlying equations for CI coeffient and orbital are still Eq. (3.27a) and (3.27b), respectively. One important consequence arising from subdivision of active space is that some of the previously redundant active-active rotations now become non-redundant because for instance a rotation $\hat{E}^t_u$, where ϕ_t and ϕ_u are from different active subgroups (say g and g' respectively), may bring some determinants in the wavefunction to $\hat{Q}$ if for these determinants $N_g = N_g^{\max}$ or if $N_{g'} = N_{g'}^{\min}$ before rotation. In general, rotations between different active subgroups bring some determinants in the wavefunction to $\hat{Q}$ and keep the rest in $\hat{\Pi}$. On the other hand, rotations between orbitals in the same active subgroup, as one would guess, are redundant. For the purpose

of this section, we shall adopt the following notation where we use primed index to denote orbital from a different active subgroup.

First, let's recall that during the discussion of TD-CASSCF in Section 3.2, we have never expressed the elements of 1RDM between active orbitals explicitly, i.e. we simply write them like D^t_u. Second, looking at Table B.1 of Appendix B, the entries corresponding to vanishing elements of 2RDM (first to 10th line) equal zero due to operations not involving active-active rotations, e.g. $\left|\hat{E}^i_t\Psi\right\rangle$, even if they do they are still projected by $\left|\hat{E}^t_i\Psi\right\rangle$. In short, all vanishing elements of 1RDM and 2RDM in the case of TD-CASSCF are again zero in TD-ORMAS. And for the non-zero elements of 2RDM involving more than one active-active rotations, again we do not calculate their explicit expressions, e.g. the 11th-14th and 16th lines. This leads to the conclusion that in TD-ORMAS, Table B.1 is still applicable and the expression of matrix elements R_{ia}, R_{it}, and R_{at} (for any ϕ_t irrespective of the subgroup) in TD-ORMAS are identical to those derived in Section 3.2.3 prompting us to proceed to the calculation of $R_{tu'}$ where ϕ_t and $\phi_{u'}$ are from different active subgroups. A different way of thinking is required, however, to obtain the expression of $R_{tu'}$. The reason is, for instance, we cannot proceed past Eq. (3.27b) by eliminating $\hat{Q}$ as we did in arriving at Eq. (3.38) because rotations such as $\hat{E}^t_{u'}$ can yield a vector lying across $\hat{\Pi}$ and $\hat{Q}$. Instead, we start by noting that the rotations involving different active orbitals do not appear in any equations in the four cases discussed in Section 3.2.3, suggesting that all equations containing elements of $\hat{R}$ between different active subgroups are obtained only if we set $\mu = t$ and $\nu = u'$ in Eq. (3.27b), that is if

$$\langle\tilde{\Psi}|H\hat{Q}\hat{E}^t_{u'} - \hat{E}^t_{u'}\hat{Q}H|\tilde{\Psi}\rangle = \langle\tilde{\Psi}|\hat{\mathcal{R}}\hat{Q}\hat{E}^t_{u'} - \hat{E}^t_{u'}\hat{Q}\hat{\mathcal{R}}|\tilde{\Psi}\rangle. \tag{3.53}$$

In the following we will first prove that any equations arising from Eq. (3.53) will not contain R_{it}, R_{ia}, R_{at} as well as their complex conjugates.

First, we can expand $\mathcal{R}$ the same way as Eq. (3.29) and (3.30) only with the addition of different active subgroups rotations to the non-redundant part

$$\langle\tilde{\Psi}|H\hat{Q}\hat{E}^t_{u'} - \hat{E}^t_{u'}\hat{Q}H|\tilde{\Psi}\rangle = \sum_{(\lambda,\gamma)\,\in\,\text{non-red}} R_{\lambda\gamma}\langle\tilde{\Psi}|\hat{E}^\lambda_\gamma\hat{Q}\hat{E}^t_{u'} - \hat{E}^t_{u'}\hat{Q}\hat{E}^\lambda_\gamma|\tilde{\Psi}\rangle.$$

The redundant part vanishes as before due to projector $\hat{Q}$. Let's now consider the terms containing core-active rotations $R_{iv}\hat{E}^i_v$, i.e. $\lambda = i$ and $\gamma = v$. In this instance, we can drop $\hat{Q}$ from the right side because $\hat{E}^i_v|\Psi\rangle$ will always be in $\hat{Q}$ space, giving us an expectation value $\langle\Psi|\left[\hat{E}^i_v, \hat{E}^t_u\right]|\Psi\rangle$ on the right. Evaluating this commutator with the help of Appendix A yields

$$\langle\Psi|-\delta_{iu'}\hat{E}^t_v + \delta_{tv}\hat{E}^i_{u'}|\Psi\rangle = 0$$

The equality comes about because $\delta_{iu'} = 0$ and $\hat{E}^i_{u'}|\Psi\rangle$ is in $\hat{Q}$ space. Following similar steps, one can show that

$$\begin{aligned}
R_{vi}\langle\tilde{\Psi}|\hat{E}^v_i\hat{Q}\hat{E}^t_{u'} - \hat{E}^t_{u'}\hat{Q}\hat{E}^v_i|\tilde{\Psi}\rangle &= 0\\
R_{av}\langle\tilde{\Psi}|\hat{E}^a_v\hat{Q}\hat{E}^t_{u'} - \hat{E}^t_{u'}\hat{Q}\hat{E}^a_v|\tilde{\Psi}\rangle &= 0\\
R_{va}\langle\tilde{\Psi}|\hat{E}^v_a\hat{Q}\hat{E}^t_{u'} - \hat{E}^t_{u'}\hat{Q}\hat{E}^v_a|\tilde{\Psi}\rangle &= 0\\
R_{ia}\langle\tilde{\Psi}|\hat{E}^i_a\hat{Q}\hat{E}^t_{u'} - \hat{E}^t_{u'}\hat{Q}\hat{E}^i_a|\tilde{\Psi}\rangle &= 0\\
R_{ai}\langle\tilde{\Psi}|\hat{E}^a_i\hat{Q}\hat{E}^t_{u'} - \hat{E}^t_{u'}\hat{Q}\hat{E}^a_i|\tilde{\Psi}\rangle &= 0
\end{aligned}$$

Hence we have shown that any equation arising from Eq. (3.53) exclusively has $R_{tu'}$ as the unknowns, other elements of $\hat{R}$ are absent. Herewith, one can separate this system of equations from the other ones containing the other elements of $\hat{R}$ and work on it to solve for all $R_{tu'}$'s.

There is no unique way in solving the ensuing matrix equation from (3.53) for $R_{tu'}$'s, but we will follow Ref. [65] by employing a separation between real and imaginary parts of (3.53) as well as of the unknowns,

$$\mathrm{Re}\langle\tilde{\Psi}|H\hat{Q}\hat{E}^t_{u'} - \hat{E}^t_{u'}\hat{Q}H|\tilde{\Psi}\rangle = \mathrm{Re}\langle\tilde{\Psi}|\hat{\mathcal{R}}\hat{Q}\hat{E}^t_{u'} - \hat{E}^t_{u'}\hat{Q}\hat{\mathcal{R}}|\tilde{\Psi}\rangle \tag{3.55a}$$

$$\mathrm{Im}\langle\tilde{\Psi}|H\hat{Q}\hat{E}^t_{u'} - \hat{E}^t_{u'}\hat{Q}H|\tilde{\Psi}\rangle = \mathrm{Im}\langle\tilde{\Psi}|\hat{\mathcal{R}}\hat{Q}\hat{E}^t_{u'} - \hat{E}^t_{u'}\hat{Q}\hat{\mathcal{R}}|\tilde{\Psi}\rangle \tag{3.55b}$$

$$R_{tu} = R^R_{tu} + iR^I_{tu} \tag{3.55c}$$

With (3.55c), one can rewrite the intersubgroup part of $\hat{\mathcal{R}}$, $R(v,w')$, as

$$R(v,w') = \sum_{(v,w')\in\mathcal{B}} \left(R^R_{vw'}\hat{E}^+_{vw'} + iR^I_{vw'}\hat{E}^-_{vw'} \right) \tag{3.56}$$

where $\hat{E}^{\pm}_{vw} = \hat{E}^v_w \pm \hat{E}^w_v$ and $\mathcal{B} = \{(v,w)\,|\,(v\in g)\wedge(w\in g')\wedge(g,g'\in\{g_1,\ldots,G\})\wedge(g>g')\}$. Using (3.56) to replace $\hat{\mathcal{R}}$ in the right side of Eq. (3.55a) and (3.55b) and after rearranging, one gets

$$\sum_{(v,w)\in\mathcal{B}} \left(\mathcal{M}^{+-}_{vw,tu}R^R_{vw} + \mathcal{M}^{--}_{vw,tu}R^I_{vw} \right) = \mathcal{N}^-_{tu} \tag{3.57a}$$

$$\sum_{(v,w)\in\mathcal{B}} \left(\mathcal{M}^{++}_{vw,tu}R^R_{vw} + \mathcal{M}^{-+}_{vw,tu}R^I_{vw} \right) = \mathcal{N}^+_{tu} \tag{3.57b}$$

valid for $(t,u)\in\mathcal{B}$, where

$$\begin{aligned}
\mathcal{M}^{\mp\mp}_{vw,tu} &= \mp\,\mathrm{Im}\ \langle\Psi|\hat{E}^{\mp}_{vw}\hat{Q}\hat{E}^{\mp}_{tu}|\Psi\rangle \\
\mathcal{M}^{\mp\pm}_{vw,tu} &= \mathrm{Re}\ \langle\Psi|\hat{E}^{\mp}_{vw}\hat{Q}\hat{E}^{\pm}_{tu}|\Psi\rangle \\
\mathcal{N}^-_{tu} &= \mathrm{Re}\ \langle\Psi|\hat{H}\hat{Q}\hat{E}^-_{tu}|\Psi\rangle \\
\mathcal{N}^+_{tu} &= \mathrm{Im}\ \langle\Psi|\hat{H}\hat{Q}\hat{E}^+_{tu}|\Psi\rangle
\end{aligned}$$

Eq. (3.57) constitutes a matrix equation

$$\mathcal{M}r = \mathcal{N} \tag{3.59}$$

with $\mathcal{M}$ being a $2N_{\mathrm{rot}}\times 2N_{\mathrm{rot}}$ square matrix, r and $\mathcal{N}$ being $2N_{\mathrm{rot}}$ column vectors. N_{rot} is given by the total number of unique intersubgroup rotations

$$N_{\mathrm{rot}} = \sum_{g'>g}^{G} n_g n_{g'}.$$

The equation of motion for dynamic core is identical to Eq. (3.50). For active orbital, a little modification is needed to account for the change in the active space structure. For an active orbital ϕ_t in an active subgroup g this equation reads

Time evolution of TD-ORMAS active orbitals

$$|i\partial_t\phi_t\rangle = \sum_j R_{jt}\,|\phi_j\rangle + \sum_u \theta_{ut}\,|\phi_u\rangle + \sum_{u'} R_{u't}\,|\phi_{u'}\rangle + \hat{q}\left(\hat{f} + \hat{\mathcal{Y}}\right)|\phi_t\rangle \tag{3.60}$$

where the second sum runs over orbitals in the same subgroup as ϕ_t while the third sum runs over orbitals in different active subgroups and $R_{tu'}$ are the solutions of Eq. (3.59).

This completes our endeavour in outlining the mathematical foundations of TD-CASSCF and TD-ORMAS methods, the two methods employed in this research. To summarize, both methods are extension of the more general TD-MCSCF method which tries to solve multi-electron time-dependent Schrödinger equation by variational principle, see Eq. (3.9). In both methods, one has the ability to require a constant double occupation for some of the lowest orbitals and whether they are also time-dependent, such doubly occupied orbitals are referred to as frozen (time-independent) and dynamic (time-dependent) cores. The rest of the occupied orbitals can have any occupation between 1 and 2 and are called active orbital. In TD-CASSCF, all possible determinants arising from rearranging active electrons among active orbitals are included in the determinant bases to represent the total wavefunction. TD-ORMAS relaxes this restriction by allowing the user to subdivide active orbitals to multiple subgroups and to control the range of occupations for each active subgroups. The equations governing CI coefficient and dynamic core orbital in both TD-CASSCF and TD-ORMAS are given by Eq. (3.33) and (3.50), respectively. For active orbital, in TD-CASSCF this equation is given by Eq. (3.51) and in TD-ORMAS by Eq. (3.60). The particular forms of these equations depend on the choice of global phase and redundant matrix element of $\hat{R}$. Although the choices of these free parameters may affect numerical stability, any expectation value evaluated with respect to the optimized wavefunction shall give identical value.

3.4 Radial Discretization and Initial Condition

The time-dependent Schrödinger equation is a partial differential equation, therefore its general solution is not uniquely defined until one imposes the boundary values of the solution.

3.4.1 Radial Discretization - The Choice of Bases

The boundary values of the solution wavefunction in spatial coordinate are determined by the square-integrability condition which otherwise would make the wavefunction unsuitable to describe a physical situation. This square-integrability requirement in our TD-MCSCF implementation is fulfilled by choosing basis functions that vanish at the origin and drop to zero faster than r^2 towards infinity. In particular, we choose spherical finite-element discrete variable representation (FEDVR) [98–101] as the basis set to span the one-particle orbital functions. This basis function looks like

$$\upsilon_{nlm}(\mathbf{r}) = \frac{p_n(r)}{r} Y_{lm}(\theta, \varphi), \tag{3.61}$$

where $p_n(r)$ are the radial DVR function defined in Ref. [98] and $Y_{lm}(\theta, \varphi)$ is a spherical harmonic. In FEDVR scheme, the radial distance is segmented into n_{FE} finite elements and each finite element further consists of n_{GP} grid points.

The grid points in each finite element are taken to be Gauss-Lobatto quadrature points [102, Sec. 3.1.4]. Then, one defines the so-called *Lobatto shape funtion* $f_{ik}(r)$ that reads

$$f_{ik}(r) = \begin{cases} \prod_{k' \neq k}^{n_{\mathrm{GP}}} \frac{r - r^i_{k'}}{r^i_k - r^i_{k'}}, & r^i_1 \leq r \leq r^i_{n_{\mathrm{GP}}} \\ 0, & \text{otherwise} \end{cases} \tag{3.62}$$

whith

$$1 \leq i \leq n_{\mathrm{FE}}$$
$$1 \leq k \leq n_{\mathrm{GP}}$$

associated with the i-th finite element and the k-th grid point inside that finite element [98]. r^i_k is the k-th quadrature grid point in the i-th finite element. Looking at Eq. (3.62), we see that at grid points inside the i-th finite element, $f_{ik}(r)$ evaluates to zero unless $r = r^i_k$. One can then associate the index n of $p_n(r)$ with an FEDVR index pair (i, k) by requiring that the boundary grids shared by adjacent finite elements be counted once. By this construction, $p_n(r)$ is calculated as

$$p_{n \Rightarrow (i,k)}(r) = \frac{f_{ik}(r)}{\sqrt{w^i_k}} \tag{3.63}$$

when $k = 2, \ldots, n_{\mathrm{GP}} - 1$, i.e. at non-boundary grid points, and

$$p_{n \Rightarrow (i,k)}(r) = \begin{cases} \frac{f_{i,n_{\mathrm{GP}}} + f_{i+1,1}}{\sqrt{w^i_{n_{\mathrm{GP}}} + w^{i+1}_1}}, & k = n_{\mathrm{GP}} \\ \\ \frac{f_{i-1,n_{\mathrm{GP}}} + f_{i,1}}{\sqrt{w^{i-1}_{n_{\mathrm{GP}}} + w^i_1}}, & k = 1 \end{cases} \tag{3.64}$$

when n corresponds to a boundary point. This bridge function ensures the continuity of orbitals at finite element boundaries. The quantity w^i_k is the quadrature weight associated to r^i_k and its appearance in (3.63) and (3.64) is to normalize $p_n(r)$ [98],

$$\int \mathrm{d}r \, p_n(r) p_{n'}(r) = \delta_{nn'}.$$

In order to ensure that the orbitals vanish at the origin and at the last radial point, the radial DVR functions p_1 and $p_{n_{\max}}$ are omitted, or equivalently the corresponding expansion coefficients $c^{\mu}_{1,l}(t)$ and $c^{\mu}_{n_{\max},l}(t)$ (see Eq. (3.65) below) be set to zero. As a side remark, the vanishing of $p_{n_{\max}}$ is actually not an exact boundary condition since if an electron is ionized, it may travell towards

infinity. But for HHG simulation, the important continuum wavepackets are those that return to the atom (consider the three-step model introduced in Chapter 1). The wavepackets that leave the atom will not contribute to the harmonic emission. Furthermore, it is also advantageous to have orbitals that slowly decrease to zero at large distances in order to minimize the effect of electron reflection. Due to the finite simulation space, a fraction of electrons leaving the atom can be reflected at the simulation boundary and hence create spurious radiation upon recombination.

One last point regarding orbitals' magnetic quantum number m, since the laser field in our implementation is always polarized in z direction, the time-dependent Hamiltonian including the laser still commutes with $\hat{L}_z$, the z component of total angular momentum operator, and M, the total magnetic quantum number of the initial wavefunction, is conserved. This constancy of M is achieved by conserving m of each initial orbital. For this reason, the expansion of electron orbitals $\phi_\mu(\mathbf{r}, t)$ in the basis set of Eq. (3.61) does not involve summation over m's different than m_μ, the initial magnetic quantum number of $\phi_\mu(\mathbf{r}, t)$. Hence the time-dependent orbital function is expanded as

$$\phi_\mu(\mathbf{r}, t) = \sum_{n=1}^{n_{\max}} \sum_{l=0}^{l_{\max}} c_{nl}^{\mu}(t) \upsilon_{nlm_\mu}(\mathbf{r}). \tag{3.65}$$

The expansion coefficients $c_{nl}^{\mu}(t)$ become the working variables in solving EOMs of orbitals, i.e. Eq. (3.49), (3.50), (3.51), and (3.60) at every time step.

3.4.2 Initial Condition - Obtaining The Ground State

The initial condition is chosen to be the ground state, which is the most common experimental condition (this condition applies if there is no pump laser which prepares the system in an excited state). There are many numerical ways to calculate the ground state of an atom. In the implementation of our TD-MCSCF program, we chose in particular the imaginary time relaxation method to do this task. Basically, this method works in a very analagous way as the ordinary (real time) propagation, one only changes the time parameter to a purely imaginary number $t \to -it$. Any numerical propagation method, including TD-MCSCF just described in the preceding sections, qualifies to be used to perform the imaginary time propagation provided that the aforesaid change of time variable is performed and no external field is present. Therefore, in this section only a proof of concept of imaginary time propagation is presented.

The proof is straightforward, one starts by expanding the guess wavefunction $|\Psi'\rangle$ in terms of field-free Hamiltonian eigenfunctions $|\Psi_m\rangle$,

$$|\Psi'\rangle = \sum_{m=0} c_m |\Psi_m\rangle$$

The imaginary time relaxation proceeds by applying imaginary time evolution operator $\hat{U}(\Delta t) = e^{-\hat{H}_0 \Delta t}$ on the wavefunction at the current step, where Δt is the step size, and $\hat{H}_0$ the field-free Hamiltonian. After k steps, one has

$$|\Psi(k)\rangle = \sum_{m=0} c_m e^{-kE_m \Delta t} |\Psi_m\rangle$$

Since $\hat{U}(\Delta t)$ is not unitary, the state $|\Psi(k)\rangle$ needs to be renormalized,

$$\left|\bar{\Psi}(k)\right\rangle = \frac{|\Psi(k)\rangle}{\sqrt{\langle\Psi(k)|\Psi(k)\rangle}} = \frac{\sum_{m=0}(c_m/c_0)e^{-k\Delta E_m \Delta t} |\Psi_m\rangle}{\sqrt{\sum_{m=0} |(c_m/c_0)|^2 e^{-2k\Delta E_m \Delta t}}} \tag{3.66}$$

with $\Delta E_m = E_m - E_0$. Eq. (3.66) is easily seen to approach $e^{i\mathrm{Arg}(c_0)} |\Psi_0\rangle$ when k is very large.

Hence, the key reason of the working of imaginary time relaxation is renormalization. In practice, it is better to renormalize the wavefunction after every time step in order to prevent the norm from going smaller than the smallest representable number of the chosen computer precision. The advantage of using imaginary time relaxation to calculate the ground state is that it provides a check for the correctness of the algorithm implementation for at least the field-free part of the time propagation program. One, for instance, can check the resulting ground state energy against the available benchmark references. On the other hand, comparison of the result of real time propagation, e.g. time-dependent acceleration (see Section 3.5), is impractical as benchmark references are hardly available. Towards the end of this chapter, we will discuss the important observables in HHG simulation, dipole moment, dipole velocity, and dipole acceleration.

3.5 Dipole Moment, Velocity, and Acceleration

When irradiated by an external lightfield, atoms or molecules will response by emitting a secondary radiation. In experiment, when the external lightfield is provided by a strong-field ($10^{13} - 10^{14}$ W/cm^2) laser, this secondary radiation is what we observe as high-harmonic photons. Now it remains to formulate how we can express this secondary radiation in mathematical terms. This is traditionally done by taking a direct analogy with the well-known classical electrodynamic result which states that the secondary emission from an oscillating dipole antenna driven by an external electromagnetic field is proportional to the dipole acceleration. With HHG being exactly the secondary emission of a quantum systems (provided the driving radiation lies in the strong-field regime), one then take it to be proportional to the second time derivative of the induced dipole moment (i.e. acceleration) of electrons in the atoms or molecules [29, p. 274],

$$E_s(t) \propto \frac{\mathrm{d}^2}{\mathrm{d}t^2} \langle \Psi | \hat{d} | \Psi \rangle$$

with $d = \sum_i^N z_i$ is the total dipole moment and we have assumed the laser to be polarized in z direction. The all-important HH spectrum is finally calculated as the power spectrum of the Fourier transform of $E_s(t)$.

The dipole moment is a sum of single-electron operators, its expectation value is therefore given by

$$d(t) = \langle \Psi | \hat{d} | \Psi \rangle = \sum_{\mu,\nu} z_{\mu\nu} \hat{E}^\mu_\nu .$$

The velocity and acceleration, however, must take a slightly different form as those that would have resulted if one solves TDSE (3.1) with exact method. When the wavefunction is the exact solution of TDSE, a quantity defined to be the first time derivative of an expectation value of another observable $\hat{O}$ reads

$$\frac{\mathrm{d}}{\mathrm{d}t} \langle \Psi | \hat{O} | \Psi \rangle = -i \langle \Psi | \left[\hat{O}, \hat{H} \right] | \Psi \rangle + \langle \Psi | \frac{\partial \hat{O}}{\partial t} | \Psi \rangle .$$

The non-exact nature of TD-CASSCF (or any general TD-MCSCF method with truncated orbitals) manifest in the appearance of an additional term which reflects the non-completeness of the determinant bases. To understand this, we start by expanding the time derivative of $\langle \hat{O} \rangle$ using product rule of derivative

$$\frac{\mathrm{d}}{\mathrm{d}t} \langle \Psi | \hat{O} | \Psi \rangle = \left\langle \frac{\partial \Psi}{\partial t} \middle| \hat{O} \middle| \Psi \right\rangle + \left\langle \Psi \middle| \hat{O} \middle| \frac{\partial \Psi}{\partial t} \right\rangle + \langle \Psi | \frac{\partial \hat{O}}{\partial t} | \Psi \rangle .$$

Then using Eq. (3.28) to replace the first time derivatives of Ψ gives, after some algebra,

$$i \frac{\mathrm{d}}{\mathrm{d}t} \langle \Psi | \hat{O} | \Psi \rangle = \langle \Psi | \left[\hat{O}, \hat{H} \right] | \Psi \rangle + i \langle \Psi | \frac{\partial \hat{O}}{\partial t} | \Psi \rangle + \Delta(\dot{O})$$

where

$$\begin{aligned} \Delta(\dot{O}) &= \langle \Psi | \hat{O}\hat{Q}\hat{\mathcal{R}} - \hat{\mathcal{R}}\hat{Q}\hat{O} | \Psi \rangle - \langle \Psi | \hat{O}\hat{Q}\hat{H} - \hat{H}\hat{Q}\hat{O} | \Psi \rangle \\ &= \sum_{\mu,\nu} O^\mu_\nu \left\{ \langle \Psi | \hat{E}^\mu_\nu \hat{Q}\hat{\mathcal{R}} - \hat{\mathcal{R}}\hat{Q}\hat{E}^\mu_\nu | \Psi \rangle - \langle \Psi | \hat{E}^\mu_\nu \hat{Q}\hat{H} - \hat{H}\hat{Q}\hat{E}^\mu_\nu | \Psi \rangle \right\} . \end{aligned} \tag{3.67}$$

We note that the terms inside curly brackets in (3.67) is identical to (3.27b) after bringing the right side terms to the left. From Eq. (3.67) we may see the reason of the appearance of this additional term to be the existence of unoccupied determinant space $\hat{Q}$, which disappear if all of the infinitely many determinants are inlcuded.

The correction term $\Delta(\dot{O})$ bears an important consequence for the correct determination of the time derivative of an expectation value in TD-CASSCF because this term is non-vanishing only when one has frozen orbitals. We recall that the various matrix elements of R (excluding those that involve frozen orbitals) derived in Section 3.2.3 serve as the solution of Eq. (3.27b) for a particular orbital pair (μ, ν). This means, if all $R_{\mu\nu}$'s appearing in Eq. (3.67) were such solutions,

then $\Delta(\dot{O}) = 0$. If, however, there are frozen orbitals among the summed indices μ or ν, the ensuing terms will not vanish.

We note that the terms for which μ and ν belong to the same orbital subspace do not contribute to $\Delta(\dot{O})$ as is evident from the appearance of operator sequence $\hat{Q}\hat{E}^{\mu}_{\nu}$ and its Hermitian conjugate. Therefore, the pairs (μ, ν) which contribute to $\Delta(\dot{O})$ only come from those in which one of them is frozen orbital and the other is either active or virtual. Using Case 1 and Case 3 from Section 3.2.3,

$$\begin{aligned}\Delta(\dot{O}) &= \sum_{i}^{\text{f.c.}} \sum_{t} O^{i}_{t} \left(- \sum_{u} \bar{h}_{ui} \bar{D}^{t}_{u} + \frac{1}{2} \langle \Psi | \left[\hat{U}, \hat{E}^{i}_{t} \right] | \Psi \rangle \right) + \sum_{i}^{\text{f.c.}} \sum_{a} O^{i}_{a} \left(-2\bar{h}_{ai} + \frac{1}{2} \langle \Psi | \left[\hat{U}, \hat{E}^{i}_{a} \right] | \Psi \rangle \right) - \text{c.c.} \\ &= 2i \sum_{i}^{\text{f.c.}} \sum_{t} \text{Im} \left\{ O^{i}_{t} \left(\sum_{u} \bar{D}^{t}_{u} \left(R_{ui} - f_{ui} \right) - G_{ti} + \sum_{v,w,u} P^{ut}_{vw} \left(J^{v}_{u} \right)_{wa} \right) \right\} + \dots \\ &\quad 2i \sum_{i}^{\text{f.c.}} \sum_{a} \text{Im} \left\{ O^{i}_{a} \left(2 \left(R_{ai} - f_{ai} \right) - G_{ai} \right) \right\} .\end{aligned}$$

The velocity and acceleration are therefore calculated as

Time-dependent dipole velocity and acceleration

$$v(t) = \frac{\mathrm{d}}{\mathrm{d}t} d(t) = -i \langle \Psi | \left[\hat{d}, \hat{H} \right] | \Psi \rangle - i\Delta(\dot{d}) \tag{3.68}$$

$$a(t) = \frac{\mathrm{d}}{\mathrm{d}t} v_{\text{exact}}(t) = -i \langle \Psi | \left[\hat{P}_z, \hat{H} \right] | \Psi \rangle - i\Delta(\dot{P}_z). \tag{3.69}$$

where

$$\hat{P}_z = \sum_{\mu,\nu} (p_z)_{\mu\nu} \hat{E}^{\mu}_{\nu},$$

$$v_{\text{exact}}(t) = -i \langle \Psi | \left[\hat{d}, \hat{H} \right] | \Psi \rangle .$$

The HH spectrum is then calculated to be the magnitude squared of Fourier transform of $a(t)$,

HH spectrum

$$\mathcal{P}_{\text{HH}}(\omega) = \left| \int_{-\infty}^{\infty} dt \, a(t) e^{i\omega t} \right|^2 \tag{3.70}$$

With the HH spectrum often becoming the cardinal quantity in any test of a computational method applied for strong-field simulations, Eq. (3.69) and Eq. (3.70) constitute two of the most important equations in the present chapter. All HH spectra presented in the subsequent chapters are calculated exactly through these formula.

As a side remark pertaining the situation where ionization is significant, in this instance the instantaneous electron cloud may be driven substantially off the origin even around the time when the laser pulse has passed. This happens when the strong field interaction leaves the atom in a superposition state such that the electron cloud is highly asymetric. The substantially large dipole moment around the pulse end can prevent a faithful calculation of Fourier transform to get the dipole spectrum (if for some reason required). On the other hand, after the laser field diminishes the acceleration will be oscillating more or less symmetrically around zero (think of a forced classical pendulum after the driving force is removed). For this reason, it is desirable to make use of the derivative property of Fourier transform which allows us to calculate the dipole as well as velocity spectra from the acceleration spectrum, i.e. HHG spectrum, by multiplication with $1/\omega^2$ and $1/\omega$ respectively.

3.6 Summary

In TD-MCSCF, the total time-dependent wavefunction is represented as a linear combinations of time-dependent determinants with time-dependent CI coefficients, see Eq. (3.3). The determinants are up from time-dependent orbitals, which along with the CI coefficients constitute the variational

quantities to be optimized in TD-MCSCF. The full TD-MCSCF, i.e., when the occupation of orbitals are not restricted, is referred to as MCTDHF. Being computationally prohibitive if the number of CI coefficients is large, an improvement in computation time is offered by TD-CASSCF thanks to its ability in restricting double occupation for some orbitals, effectively reducing the number of configurations, while still possessing gauge invariant property. Further reduction in computation time can be achieved by dividing active orbitals into several subgroups and imposing restriction on the range of occupations in each subgroup. This method corresponds to TD-ORMAS, which is also gauge invariant. The equation of motion (EOM) for CI coefficients in TD-CASSCF and TD-ORMAS are the same, and is given in Eq. (3.27a) up to the choice of phase factor $\chi(t)$. The EOMs for frozen, dynamic, and active orbitals in TD-CASSCF are given in Eq. (3.49), (3.50), and (3.51), respectively. While EOMs for frozen and dynamic orbitals in TD-ORMAS are identical as in TD-CASSCF, the EOM for active orbital is given in Eq. (3.60). These orbital EOMs are, however, up to the choice of redundant matrix elements $\hat{\theta}$. The particular choices of these freedoms, i.e., the choice of global phase factor and redundant matrix elements do not change expectation values of observables calculated with respect to TD-MCSCF wavefunction, but they may affect the stability of the numerical propagation.

Chapter 4

Resonant High-Harmonic Generation from Mn Plasma

The systems considered in the current chapter are Mn ($Z = 25$), Mn^+ and Mn^{2+}. With moderate number of electrons, atomic Mn and its first few cations are an ideal testbed to verify the capability of resource-intensive methods such as TD-CASSCF and TD-ORMAS to reproduce resonant enhancement in HHG. From the perspective of application, HHG from Mn plasma also possesses an attractive feature, the photon energy where the resonant enhancement occurs, $\sim$ 50 eV, is the highest among other metallic plasma that have been reported so far as HH source [37, 38]. The primary goal of this chapter is therefore to investigate resonant enhancement that is experimentally observed in Mn plasma HHG and to arrive at an understanding about the mechanism that gives rise to this enhancement.

4.1 Simulation Conditions

All simulation results presented in this chapter were obtained using TD-MCSCF methods discussed in Chapter 3. For easier reference for the rest of the chapter, the input parameters of these simulations, such as orbital subspace decompositions, laser parameters, grid points and so on, are compiled in the present section.

4.1.1 Ground State Simulation Conditions

As outlined in Section 3.4.2, the ground state is obtained by running a numerical propagation with purely imaginary time. For all ground states used in the present chapter, Slater type functions are used as the guess orbital to feed the imaginary time relaxation. The orbital subspace decompositions used in obtaining the ground states are displayed in Fig. 4.1. The DVR grid points used to span the orbitals during ground state calculations are identical for Mn, Mn^+, and Mn^{2+}, and are presented in Table 4.2.

The electronic configurations of Mn, Mn^+, and Mn^{2+} are given in Table 4.3. In this section, except for Mn^{2+} we generally employ two different methods to get the ground state. The first method is CASSCF which uses orbital schemes as depicted in 4.1(a), (b), and (c) for Mn, Mn^+, and Mn^{2+}, respectively. The second method is ORMAS, which uses Fig. 4.1(d) and (e) for Mn and Mn^+. No ORMAS result for Mn^{2+} is presented because many computationally tractable ORMAS orbital occupation settings have been tried, yet all of them fail to produce a ground state with vanishing dipole moment, as it should for a stationary state of an atom must have a definite parity.

For Mn and Mn^+, CASSCF requires at least 15 orbitals to accomodate all electrons so that Pauli exclusion principle is still satisfied, whereas for the dication a minimum of 14 orbitals are needed. For the purpose of a later study in finding out which orbitals are responsible for the resonant enhancement, it becomes necessary to vary the boundary between dynamic and active orbitals. These different orbital schemes are indicated by "dn. $2p$", "dn. $3s$", and "dn. $3p$" in Fig. 4.1 and "MCHF" (not shown) where all 15 orbitals are active. In order to have more accurate analysis, we also prepare ground states for Mn and Mn^+ obtained using ORMAS single double

Table 4.1: The number of determinants, ground state energies, and orbital energies of Mn, Mn^+, and Mn^{2+} obtained using various methods as mentioned in the text. Energy values inside parentheses indicate a relative value $\Delta E = E - E_{\mathrm{MCHF}}$, where E is its absolute value and E_{MCHF} is the corresponding MCHF energy for that ionic species. All energies are in Hartree.

Ion	Mn					Mn^+					Mn^{2+}			
Method	MCHF	dn. $2p$	dn. $3s$	dn. $3p$	ORMAS	MCHF	dn. $2p$	dn. $3s$	dn. $3p$	ORMAS	MCHF	dn. $2p$	dn. $3s$	dn. $3p$
No. of dets	629	52	26	2	86510	997	44	18	1	66068	410	26	12	1
GS energy	−1149.890661	(+0.000102)	(+0.000102)	(+0.024409)	−1150.076001	−1149.673886	(+0.000108)	(+0.000932)	(+0.024503)	−1149.855479	−1149.134376	(+0.000107)	(+0.000144)	(+0.025155)
Orbital energies $1s$	−240.530111	(−0.000047)	(−0.000047)	(−0.003881)	−240.542021	−240.824263	(−0.000053)	(−0.001015)	(−0.003991)	−240.838479	−241.183325	(−0.000049)	(−0.000054)	(−0.003718)
$2s$	−29.104334	(−0.000066)	(−0.000066)	(−0.005141)	−29.121675	−29.396134	(−0.000077)	(−0.000605)	(−0.005243)	−29.421164	−29.745874	(−0.000068)	(−0.000077)	(−0.004891)
$2p_{-1}$	−24.807756	(−0.000149)	(−0.000149)	(−0.004834)	−24.836419	−25.100402	(−0.000154)	(−0.000408)	(−0.004931)	−25.129565	−25.453132	(−0.000055)	(−0.000064)	(−0.004493)
$2p_0$	−24.807756	(−0.000149)	(−0.000149)	(−0.004834)	−24.836419	−25.100402	(−0.000154)	(−0.000408)	(−0.004931)	−25.129565	−25.453132	(−0.000055)	(−0.000064)	(−0.004493)
$2p_{+1}$	−24.807756	(−0.000149)	(−0.000149)	(−0.004834)	−24.836419	−25.100402	(−0.000154)	(−0.000408)	(−0.004931)	−25.129565	−25.453132	(−0.000055)	(−0.000064)	(−0.004493)
$3s$	−3.812528	(−0.000036)	(−0.000036)	(−0.004119)	−18.160937	−4.101759	(−0.000040)	(−0.000300)	(−0.004263)	−21.318154	−4.451581	(−0.000038)	(−0.000028)	(−0.004016)
$3p_{-1}$	−2.484469	(+0.000079)	(+0.000079)	(+0.004937)	−16.314911	−2.775400	(+0.000076)	(−0.000039)	(+0.004852)	−17.293419	−3.130824	(−0.000017)	(+0.000001)	(+0.005187)
$3p_0$	−2.484469	(+0.000079)	(+0.000079)	(+0.004937)	−16.314887	−2.775400	(+0.000076)	(−0.000039)	(+0.004852)	−17.293419	−3.130824	(−0.000017)	(+0.000001)	(+0.005187)
$3p_{+1}$	−2.484469	(+0.000079)	(+0.000079)	(+0.004937)	−16.314887	−2.775400	(+0.000076)	(−0.000039)	(+0.004852)	−17.293419	−3.130824	(−0.000017)	(+0.000001)	(+0.005187)
$3d_{-2}$	−0.646173	(+0.000024)	(+0.000024)	(+0.007325)	−11.659529	−0.940357	(+0.000021)	(+0.000269)	(+0.007150)	−12.386179	−1.295604	(+0.000023)	(+0.000038)	(+0.007349)
$3d_{-1}$	−0.646173	(+0.000024)	(+0.000024)	(+0.007325)	−11.659529	−0.940357	(+0.000021)	(+0.000269)	(+0.007150)	−12.386178	−1.295604	(+0.000023)	(+0.000038)	(+0.007349)
$3d_0$	−0.646173	(+0.000024)	(+0.000024)	(+0.007325)	−11.659527	−0.940357	(+0.000021)	(+0.000269)	(+0.007150)	−12.386178	−1.295604	(+0.000023)	(+0.000038)	(+0.007349)
$3d_{+1}$	−0.646173	(+0.000024)	(+0.000024)	(+0.007325)	−11.659527	−0.940357	(+0.000021)	(+0.000269)	(+0.007150)	−12.386178	−1.295604	(+0.000023)	(+0.000038)	(+0.007349)
$3d_{+2}$	−0.646173	(+0.000024)	(+0.000024)	(+0.007325)	−11.659526	−0.940357	(+0.000021)	(+0.000269)	(+0.007150)	−12.386178	−1.295604	(+0.000023)	(+0.000038)	(+0.007349)
$4s$	−0.247549	(−0.000002)	(−0.000002)	(−0.000322)	−0.436677	−0.543604	(+0.000004)	(−0.000012)	(−0.000706)	−0.804669				
$4d_{-2}$					6.043347					5.964270				
$4d_{-1}$					6.043347					5.964270				
$4d_0$					6.043347					5.964270				
$4d_{+1}$					6.043347					5.964270				
$4d_{-2}$					6.043347					5.964270				
$5s$					7.951378					8.093741				
$4p_{-1}$					7.951395					8.093741				
$4p_0$					7.951395					8.093741				
$4p_{+1}$					8.320806					10.208535				

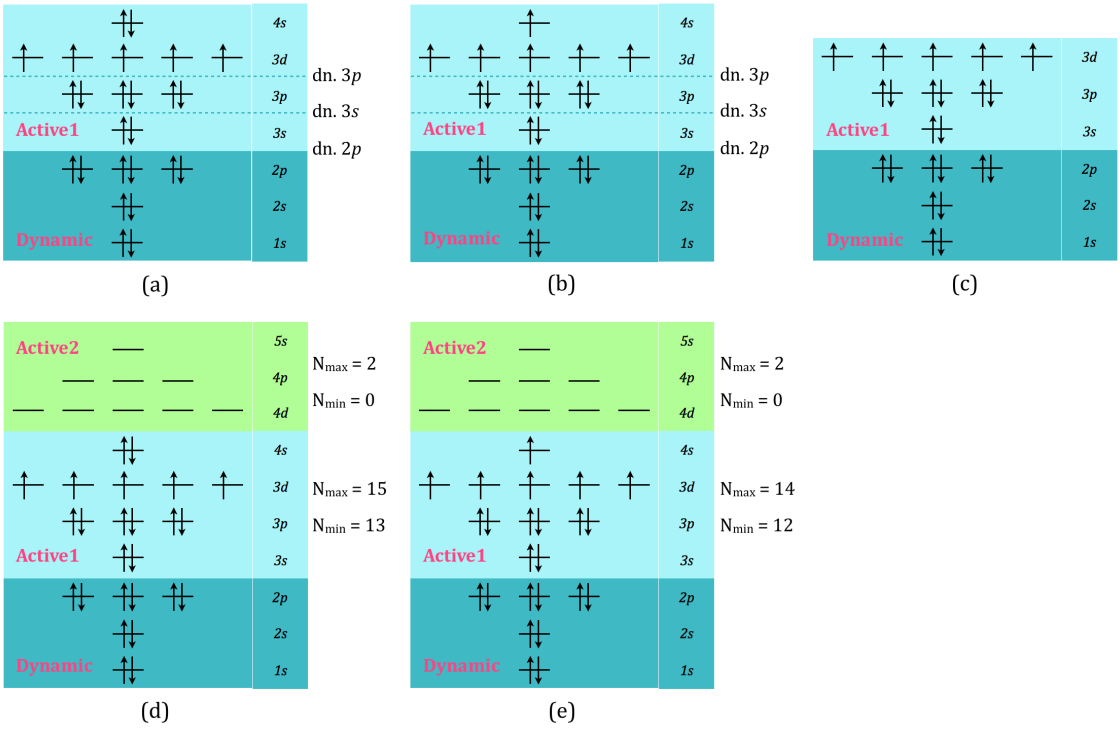

Figure 4.1: Orbital subspace decompositions used to calculate the ground states for simulations in the present chapter.

Table 4.2

Interval	no. of FEs	n_{GP} per FE
0.0 – 1.0	1	25
1.0 – 3.0	1	25
3.0 – 6.0	1	25
6.0 – 10.0	1	25
10.0 – 42.0	8	25

(SD) method with 24 orbitals (Fig. 4.1(d) and (e)). In this method, we chose to divide the active orbitals into two subgroups: Active1 and Active2 as indicated in Fig. 4.1(d) and (e), and restrict up to two electron excitations (hence the specification single double) from Active1 to Active2. These ORMAS simulations were carried out in a phased manner. For example, to get ORMAS final wavefunction for Mn, we start the imaginary time relaxation by using CI coefficients and orbitals produced by orbital scheme "dn. 2p" in Fig. 4.1(a) as the guess wavefunction instead of using the Slater type functions. This proves to be more stable in that it allows longer time step to be used during the ORMAS (last) phase. Whereas for Mn^+, the ORMAS phase started from CI coefficients and orbitals produced by CASSCF with the same orbitals as Fig. 4.1(b) except that all of them are active (i.e. MCHF).

The resulting ground state energy, number of determinants, and orbital energies of Mn and Mn^+ using MCHF, dn. 2p, dn. 3s, dn. 3p, and ORMAS and of Mn^{2+} using MCHF, dn. 2p, dn. 3s, and dn. 3p are summarized in Table 4.1. We do not perform simulation on higher ionic states than the dication because the laser intensities used throughout this chapter do not exceed 3×10^{14} W/cm^2, which is to be compared with the barrier suppression intensity of the dication in Table 4.3.

4.1.2 HHG Simulation Conditions

The calculated ground states discussed in Section 4.1.1 serve as the initial boundary value of wavefunction for the real-time propagation (the HH simulation). These HH simulations must

Table 4.3: Experimental ionization potential I_p, barrier-suppression intensity I_{BS}, and the ground-state configuration of Mn, Mn^+, and Mn^{2+}.

	Mn	Mn^+	Mn^{2+}
I_p[a]	7.43	15.64	33.67
I_{BS}[b]	1.2×10^{13}	2.4×10^{14}	5.2×10^{15}
GS[c]	$[Ar]4s^2 3d^5(^6S_{5/2})$	$[Ar]4s3d^5(^7S_3)$	$[Ar]3d^5(^6S_{5/2})$

[a] Experimental ionization potential in eV [103].
[b] Barrier-suppression intensity in W/cm^2.
[c] Ground state configuration [103].

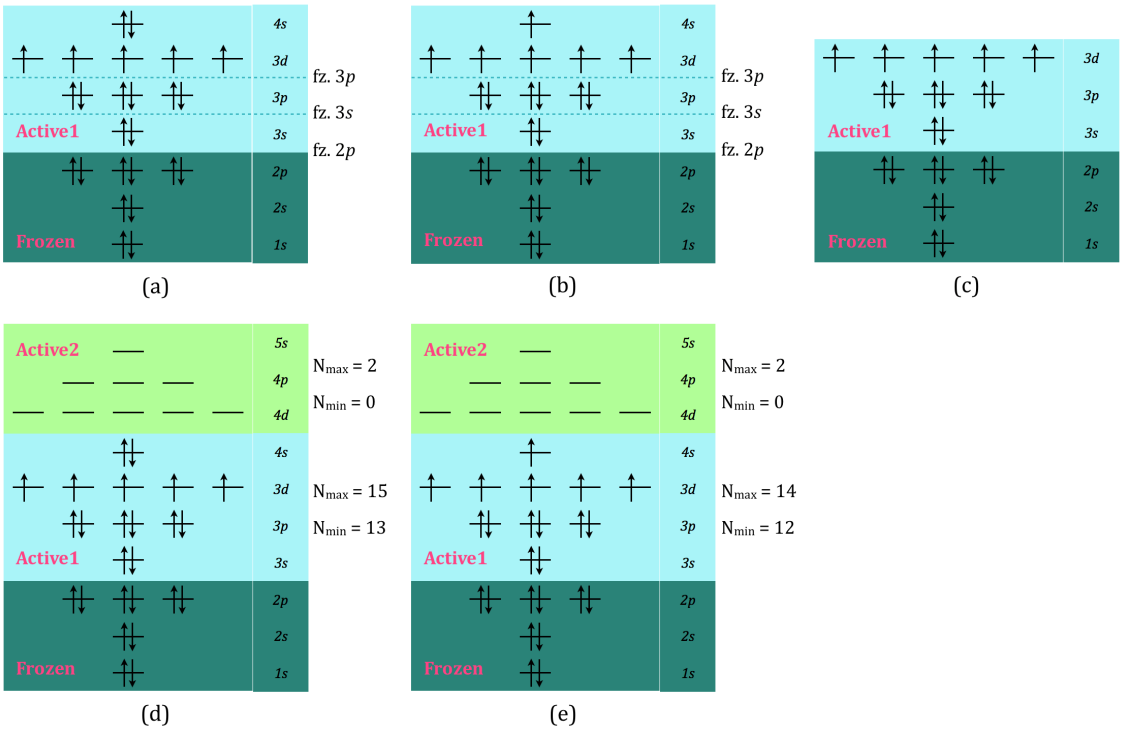

Figure 4.2: Orbital subspace decompositions used to perform HH simulations in the present chapter.

use the same orbitals and employ the same orbital occupation scheme as those used in obtaining the starting ground state, i.e. frozen or dynamic orbitals in the ground state can be made frozen or dynamic as well for the HH simulation since the occupations are still double, but not active. Meanwhile an active orbital in the ground state can only become active orbital in the HH simulation. In case TD-ORMAS is requested, the number of subgroups, which orbitals belong to each subgroup, and the occupation restrictions (e.g. single, double, triple etc) in each subgroup must also be identical between ground state and HH simulations. Bearing these requisites in mind, we set the orbital schemes for HH simulations as depicted in Fig. 4.2, i.e. all dynamic orbitals in Fig. 4.1 have been changed to frozen.

For HH simulations, the DVR radial grid points should be larger than and contain those used in the corresponding ground state calculation, these grids are given in Table 4.4, Table 4.5, Table 4.6, Table 4.7, and Table 4.8. The other inputs, which are single-valued parameters, are summarized and defined as follows,

L_{max}	=	Maximum angular momentum in a.u. for spherical harmonics.
p. shape	=	Pulse shape.
λ_0	=	Laser center wavelength in nanometers.
I_0	=	Laser peak intensity in W/cm^2.

Input 4.1	
$L_{\max}$	47
p. shape	$\sin^2$
λ_0	770
I_0	3×10^{14}
φ_{CEP}	0°
p. length	4-cycle
n_{sp}	10000
Grid	Table 4.4
Absorb	irECS
r_{abs}	46.0
θ	15°

Input 4.2	
$L_{\max}$	47
p. shape	$\sin^2$
λ_0	770
I_0	3×10^{14}
φ_{CEP}	0°
p. length	4-cycle
n_{sp}	17000
Grid	Table 4.5
Absorb	Mask
r_{mask}	205.7

Input 4.3	
$L_{\max}$	47
p. shape	$\sin^2$
λ_0	770
I_0	3×10^{14}
φ_{CEP}	0°
p. length	4-cycle
n_{sp}	10000
Grid	Table 4.6
Absorb	Mask
r_{mask}	160

Input 4.4	
$L_{\max}$	45
p. shape	$\sin^2$
λ_0	1820
I_0	5×10^{13}
φ_{CEP}	0°
p. length	4-cycle
n_{sp}	15000
Grid	Table 4.7
Absorb	irECS
r_{abs}	142.0
θ	15°

Input 4.5	
$L_{\max}$	40
p. shape	$\sin^2$
λ_0	1333.7
I_0	1×10^{14}
φ_{CEP}	0°
p. length	4-cycle
n_{sp}	17000
Grid	Table 4.5
Absorb	Mask
r_{mask}	205.7

Input 4.6	
$L_{\max}$	40
p. shape	$\sin^2$
λ_0	1333.7
I_0	1×10^{14}
φ_{CEP}	0°
p. length	4-cycle
n_{sp}	17000
Grid	Table 4.8
Absorb	Mask
r_{mask}	154.7

φ_{CEP}	=	Laser carrier-envelope phase in degree. A value of 0° means that an oscillation peak coincides with the envelope peak.
p. length	=	Pulse length in cycle.
n_{sp}	=	The number of temporal points in single cycle
Grid	=	Radial DVR grid points.
Absorb	=	The type of absorbing boundary.
r_{mask}	=	Needed if Absorb = mask, and is the radial position of the start of $\cos^{1/4}$ damping part. Unit in Bohr.
r_{abs}	=	Needed if Absorb = irECS, and is the radial position where the complex region begins. Unit in Bohr.
θ	=	Needed if Absorb = irECS, and is the damping parameter that controls the rate of decay of the orbital within the complex region. Unit in degree.

The sets of input parameters which are employed in various HH simulations in this chapter are listed in Input 4.1, Input 4.2, Input 4.3, Input 4.4, Input 4.5, and Input 4.6. Some of these input sets use infinite range exterior complex scaling (irECS) [104, 105] to efficiently reduce the radial size. The use of irECS is characterized by two parameters, the radial boundary between real and complex regions and the damping parameter (mathematically, the angle in the complex region). The choice of complex region boundary is based on the quiver amplitude of laser-driven electrons. As far as our experience is concerned, about twice the quiver amplitude is sufficient to place the complex region boundary. For example, irECS is used in Input 4.1 and Input 4.4 where the laser intensity is 3×10^{14} W/cm^2 and the wavelength is 770 nm, hence the classical quiver amplitude is

Table 4.4

Interval	no. of FEs	n_{GP} per FE
GS grid Table 4.2		
42.0 – 46.0	1	25
46.0 – 54.0	2	25
54.0 – 58.0	1	25

Table 4.5

Interval	no. of FEs	n_{GP} per FE
GS grid Table 4.2		
42.0 – 242.0	50	25

Table 4.6

Interval	no. of FEs	n_{GP} per FE
GS grid Table 4.2		
42.0 – 202.0	40	25

Table 4.7

Interval	no. of FEs	n_{GP} per FE
GS grid Table 4.2		
42.0 – 142.0	25	25
142.0 – 150.0	2	25
150.0 – 154.0	1	25

Table 4.8

Interval	no. of FEs	n_{GP} per FE
GS grid Table 4.2		
42.0 – 182.0	35	25

about $\mathcal{E}_0/\omega_0^2 \approx 26.4$ Bohr. Therefore, the complex region boundary is chosen to be at $r = 46$ Bohr and set the damping parameter $\theta = 15°$.

4.2 The Resonant Enhancement in HH Spectrum from Mn Plasma

The all-important HH spectra from Mn, Mn^+, and Mn^{2+} will be presented here. The TD-CASSCF (light color) and TD-ORMAS (dark color) time-dependent dipole moment, dipole velocity, and dipole acceleration as well as their respective power spectra for Mn, Mn^+, and Mn^{2+} are shown in Fig. 4.3, Fig. 4.4, and Fig. 4.5, respectively. The orbital subspace decomposition for TD-CASSCF results for Mn, Mn^+, and Mn^{2+} are obtained using Fig. 4.2(a) fz. $2p$, 4.2(b) fz. $2p$, and 4.2(c) fz. $2p$, respectively. The laser parameters and other input parameters for these simulations are summarized in Input 4.1. Whereas for TD-ORMAS results, Mn and Mn^+ simulations use orbital subspace decompositions in Fig. 4.2(d) and Fig. 4.2(e) and laser and other input parameters in Input 4.2 and Input 4.3, respectively.

From velocity spectrum in panel (e) and acceleration or HHG spectrum in panel (f) of Fig. 4.3, 4.4, and X, it is evident that the harmonic peak around 51.5 eV is enhanced several times stronger than the neighboring ones. Recall that the experimentally observed enhancement from Mn plasma occurs at around 50 eV (see Table 1.1) [37, 38]. Upon comparing TD-CASSCF and TD-ORMAS results in Mn and Mn^+, it is seen that in general the two methods produce qualitatively similar dipole moment, velocity, and acceleration as well as their spectra. The features of the spectra such as resonance position and cutoff energy agree reasonable well between the two methods. Hereby, we have demonstrated the success of TD-CASSCF and TD-ORMAS in reproducing the experimentally observed resonant enhancement in HH spectra from Mn plasma. With spin multiplicities of 6 and 7 (Table 4.3), to the best of our knowledge our results demonstrate a pioneering successful time-dependent *ab initio* simulations applied to open-shell systems having high spin quantum numbers.

4.2.1 Calculated Excitation Spectra

Being a transition element in the periodic table, Mn has partially filled $3d$ orbitals - five electrons are in there in Mn, Mn^+, and Mn^{2+}. Therefore, provided the exciting light has a sufficient photon energy, one photon absorption can easily induce core excitation to $3d$ orbitals from a lower orbital.

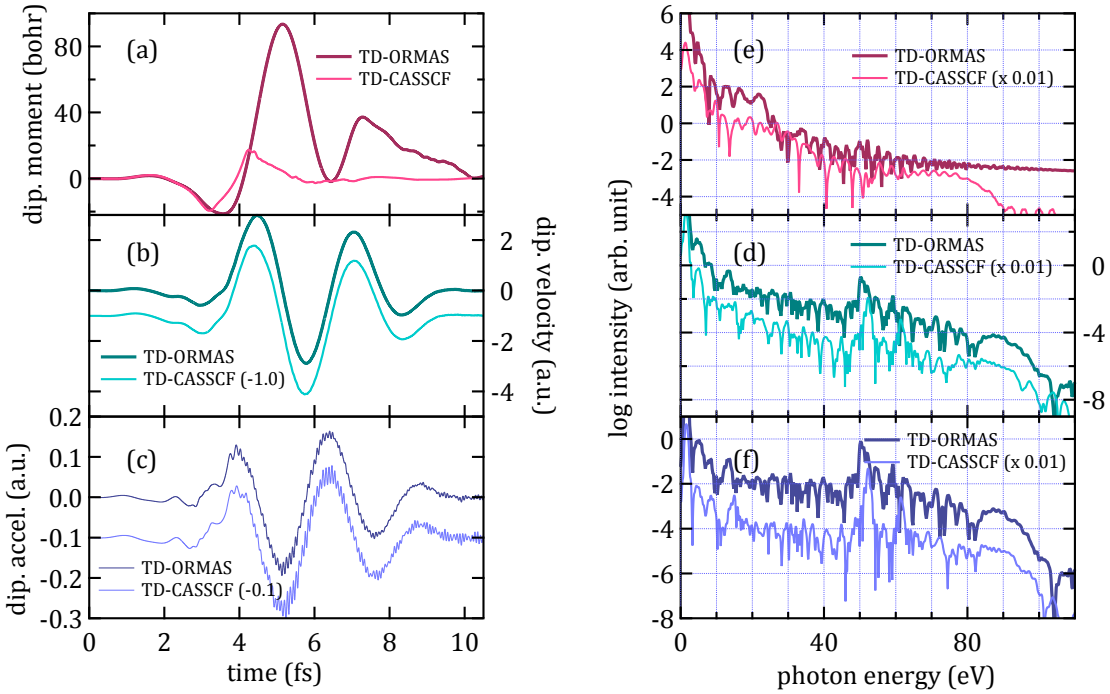

Figure 4.3: The time-dependent dipole moment (a), velocity (b), and acceleration (c) from neutral Mn using TD-ORMAS (dark color) and TD-CASSCF fz. 2*p* (light color). The corresponding power spectra are plotted in (e)-(f). To enhance visibility, TD-CASSCF results are shifted in (a)-(c) and scaled in (e)-(f), with the amount of shift and scaling indicated after the plot label. The HH spectra are the acceleration spectra in panel (f).

Fig. 4.6 shows 3*p* photoabsorption cross sections of Mn, Mn^+, and Cr (Cr also has five 3*d* electrons) within an energy range from 42 eV to 70 eV [106]. Around 51 eV in Mn and Mn^+ and 43.6 eV in Cr, one can see one or several prominent peaks. Each of these peaks is associated to a highly probable one-electron transition from 3*p* to 3*d*. By means of TD-MCSCF method, excitation spectra of this sort can be calculated.

In order to calculate excitation spectra, δ-kick simulations were performed where the external field takes the form of a delta impulse having non-zero values only at three consecutive points and low intensity (1×10^8 W/cm^2). In such interaction, the system starting from ground state receives a jolt, populating many excited states. Taking the time-dependent dipole moment with respect to such wavefunction and calculate the power spectrum yields an excitation spectrum. The calculated excitation spectra of Mn, Mn^+, and Mn^{2+} obtained through TD-CASSCF fz. 2*p* and TD-ORMAS SD (see Fig. 4.2) are shown in Fig. 4.7. One can confirm that there does exist a large transition line at 50.3 eV in all ionic species calculated with TD-CASSCF fz. 2*p* (Fig. 4.7(a)) and at 51.5 eV in Mn and Mn^+ calculated with TD-ORMAS SD (Fig. 4.7). We note that these peaks are about as strong as the lowest transition line.

Although eventually the calculated excitation spectra confirm the experimental ones (at least within an energy range around 50 eV), e.g. the Mn and Mn^+ panels in Fig. 4.6, the calculated spectra are still necessary in order to ascertain that the enhancement at a particular energy is indeed accompanied by the presence of a large transition amplitude at the same energy obtained through the same method. Calculated excitation spectra are also essential when the giant transition lines from different ionization stages of the atom do not coincide.

4.2.2 The Role of 3*p* Orbitals in The Resonant Enhancement

The question that naturally arises following the observation of an unusually intense harmonic peak in the plateau region is undoubtedly regarding the physics behind it. Some early works link the origin of such enhancement with the existence of a giant transition amplitude at the same energy where the enhancement occurs [35, 36]. Indeed, looking back at Fig. 4.6, there exist a large 3*p* photoabsorption peak around 51 eV. Whether this is the actual mechanism, none of the previously

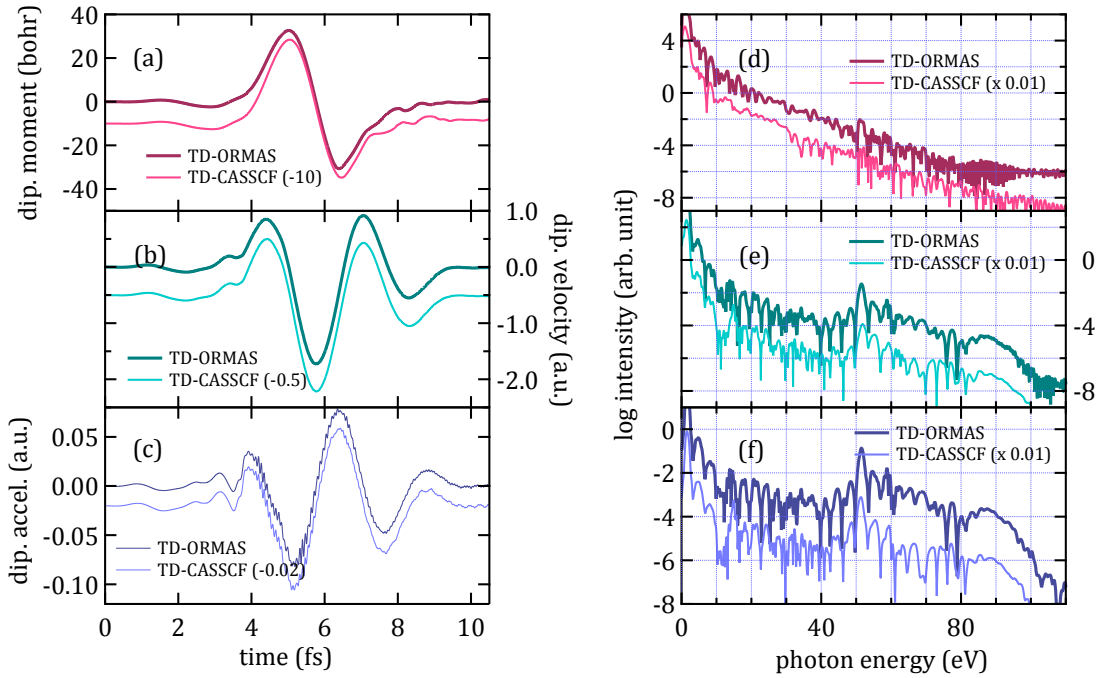

Figure 4.4: The time-dependent dipole moment (a), velocity (b), and acceleration (c) from Mn^+ using TD-ORMAS (dark color) and TD-CASSCF fz. 2*p* (light color). The corresponding power spectra are plotted in (e)-(f). To enhance visibility, TD-CASSCF results are shifted in (a)-(c) and scaled in (e)-(f), with the amount of shift and scaling indicated after the plot label. The HH spectra are the acceleration spectra in panel (f).

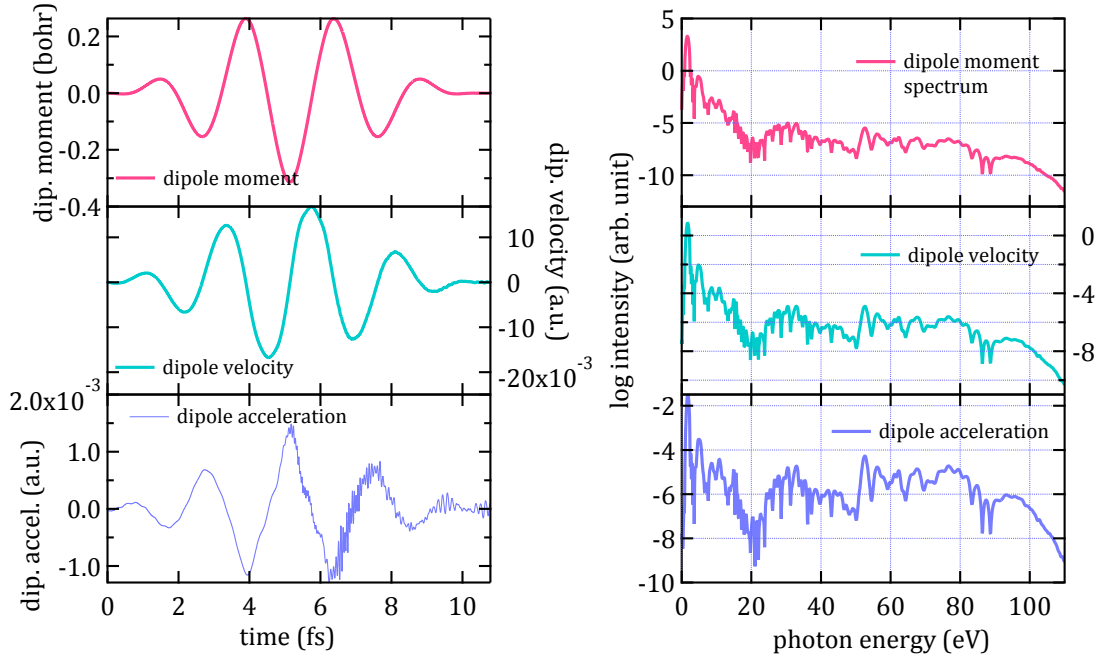

Figure 4.5: The time-dependent dipole moment (a), velocity (b), and acceleration (c) from Mn^{2+} TD-CASSCF fz. 2*p*. The corresponding power spectra are plotted in (e)-(f). The HH spectra are the acceleration spectra in panel (f).

proposed methods were able to unambiguously provide an answer. These methods rely on SAE approximation and the resonant structure is encoded in the choice of potential (the procedure of which is likely to be of a trial-and-error type) or by manually introducing a second state to be superposed with the ground state (see Chapter 2). In SAE methods, clearly the knowledge of

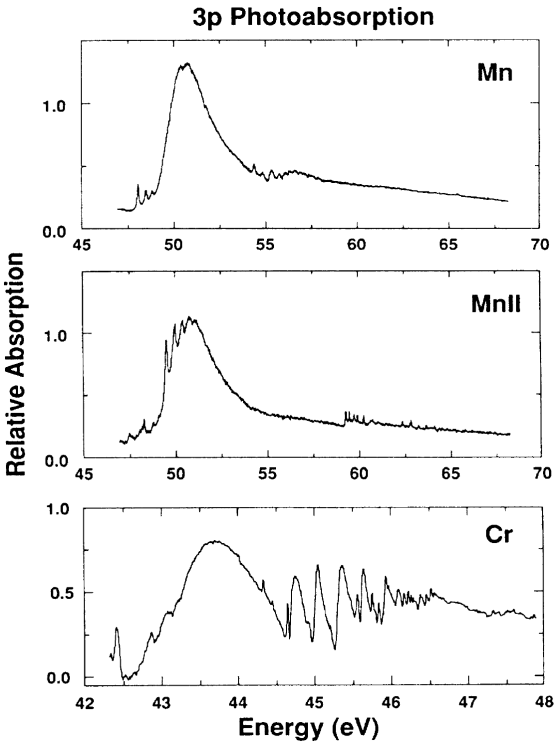

Figure 4.6: Experimental relative absorption cross sections for Mn, Mn^+, and Cr. Reprinted figure with permission from [J. W. Cooper, C. W. Clark, C. R. Cromer, T. B. Lucatorto, B. F. Sonntag, E. T. Kennedy, and J. T. Costello, "Marked differences in the 3p photoabsorption between the Cr and Mn^+ isoelectronic pair: Reasons for the unique structure observed in Cr", *Phys. Rev. A* **39**, 6074 (1989)]. Copyright 1989 by the American Physical Society.

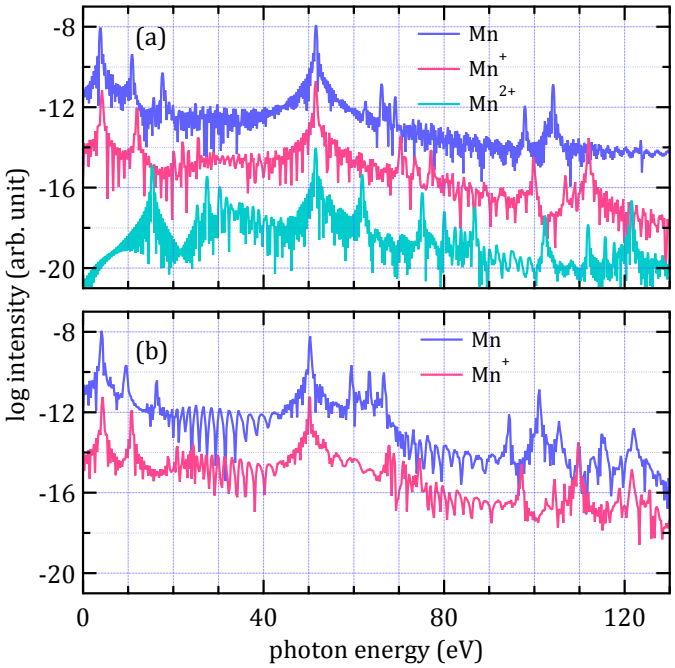

Figure 4.7: Calculated excitation spectrum of Mn, Mn^+, and Mn^{2+} obtained using (a) TD-CASSCF and (b) TD-ORMAS.

which orbitals are responsible for the resonance is not accessible.

TD-MCSCF relies on the representation of wavefunction in determinants which is further made

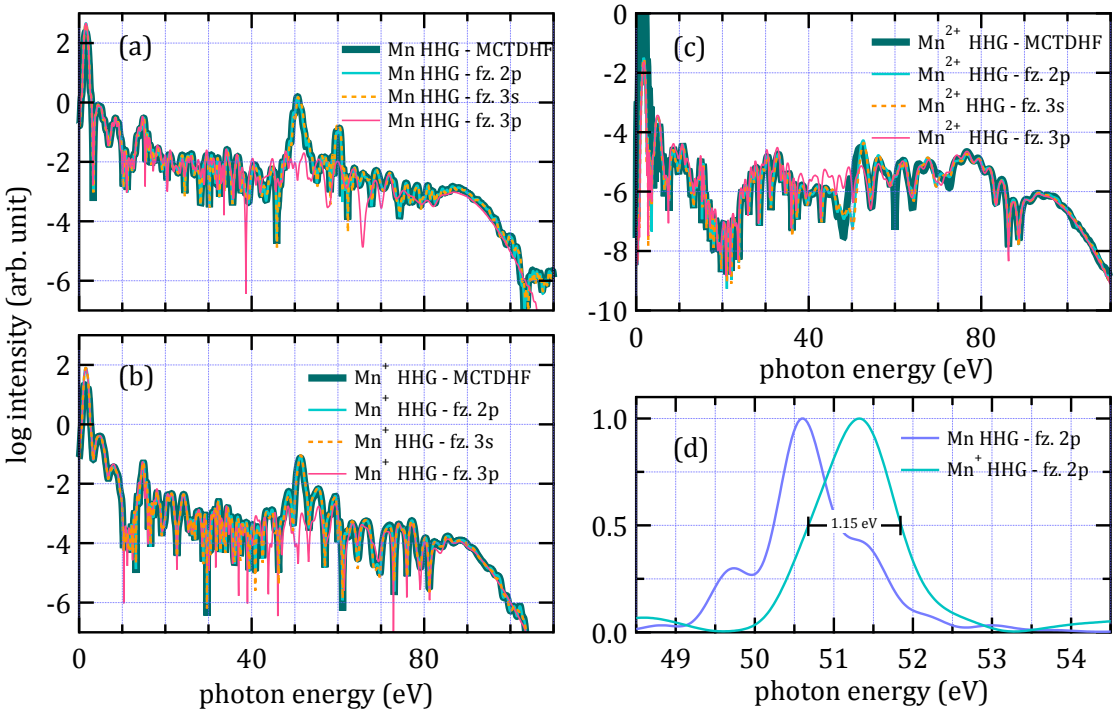

Figure 4.8: HH spectra from (a) Mn, (b) Mn^+, and (c) Mn^{2+} obtained using TD-CASSCF with orbital subspace decompositions differing in the boundary of the frozen set. Consult Fig. 4.2(a), (b), and (c) regarding the orbital schemes. The laser intensity is 3×10^{14} W/cm^2 and the wavelength is 770 nm. (d) The lineshape in linear scale of the enhanced harmonic from fz. $2p$ spectra in (a) as dark green and in (b) as cyan lines.

up of time-dependent one-particle orbitals. We exploit this property of our TD-MCSCF method to gain a deeper insight into the physics underlying resonant HHG. In this section, we start the analysis by varying the boundary between frozen and active orbitals during HH simulations in Mn, Mn^+, and Mn^{2+} (Fig. 4.2(a), (b), and (c)) [69]. The results are summarized in Fig. 4.8. All spectra presented in Fig. 4.8 are obtained using Input 4.1.

First, we run MCTDHF simulations (all orbitals active in Fig. 4.2) and the thick dark green spectra (MCTDHF) resulted. As it should be, this method, which is the most accurate simulation within 15 orbitals restriction, is able to seamlessly produce the resonant enhancement at 51.5 eV. Then, orbitals from $1s$ to $2p$ are frozen (using fz. $2p$ in Fig. 4.2(a), (b), and (c)) and we obtain the thin cyan spectra which are practically still identical to the MCTDHF spectra in all ionic species. This result demonstrates that TD-CASSCF can be as accurate as MCTDHF provided the choice of orbital subspace decomposition is appropriate with respect to laser parameters. Adding one more orbital $3s$ to be frozen (using fz. $3s$ in Fig. 4.2(a), (b), and (c)), we get the dashed yellow spectra (fz. $3s$) exhibiting no discernible differences with previous two spectra. Finally, when $3p$ orbitals are frozen (using fz. $3p$ in Fig. 4.2(a), (b), and (c)), a notable modification in the spectrum around the resonant energy is observed - the enhancement is lost. This observation hints at a crucial involvement of transitions from $3p$ orbitals in the enhancement process in Mn plasma because by freezing $3p$ orbitals, we are actually removing any determinants in the determinant basis set where $3p$ orbitals are not doubly occupied, i.e., no $3p$ transitions can happen if these orbitals are frozen. Fig. 4.8 further tells us that the contribution from these unknown transitions involving $3p$ is effectively limited to the enhancement only. If one compares fz. $3p$ spectra and any of the other three spectra in each ionic species, one sees that the differences in the shape of the peaks are remarkably small outside the enhancement region.

Fig. 4.8(d) shows a close up view of the enhanced harmonic from fz. $2p$ HH spectra in Fig. 4.8(a) and (b). While it is possible to quantify the full width at half maximum (FWHM) of Mn^+ peak, due to the substructures appearing in Mn peak doing so will not give a value which allows an accurate comparison with Mn^+ peak. It is known that the width of the harmonics in HH spectra in general scales reciprocally with driving laser pulse duration. Although a proper analysis has not been performed in this dissertation, the width of the enhanced peak does not necessarily behave

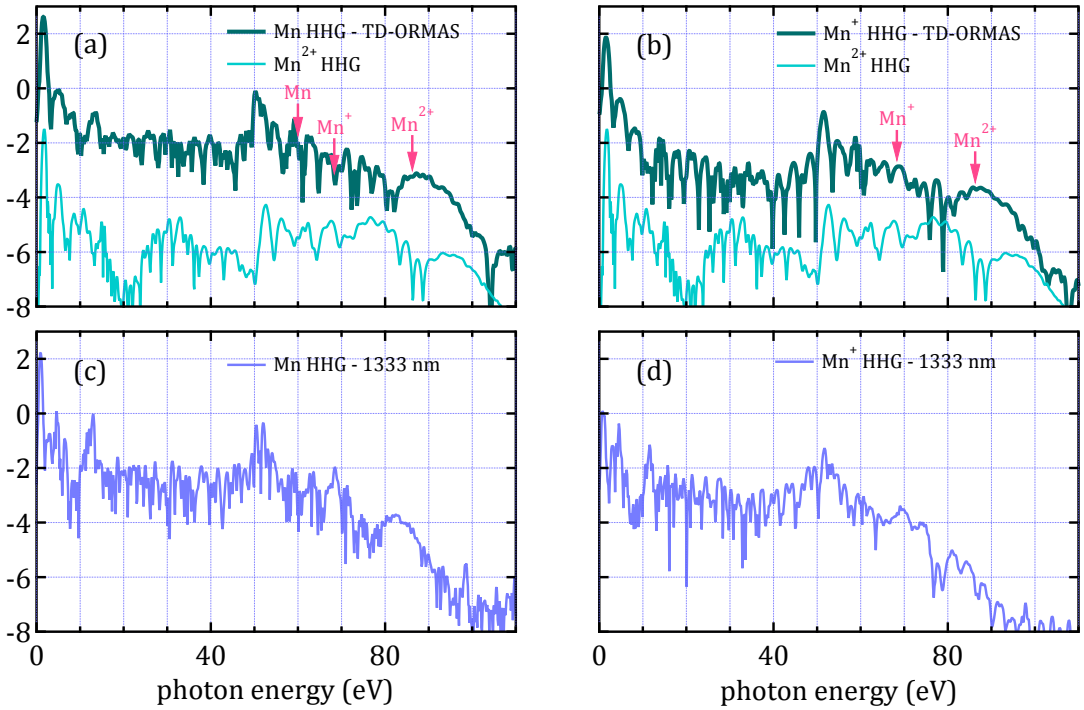

Figure 4.9: TD-ORMAS HHG spectra from Mn ((a) and (c)) and Mn^+ ((b) and (d)). For (a) and (b), the peak intensity is $I_0 = 3 \times 10^{14}$ W/cm^2 and the wavelength is $\lambda_0 = 770$ nm. For (c) and (d), $I_0 = 1 \times 10^{14}$ W/cm^2 and $\lambda_0 = 1333$ nm.

the same way as the ordinary harmonics when the driving pulse duration is changed. The reason is that the upper state (to be determined later in Section 4.3.1) which is in resonant with the ground state usually corresponds to an autoionizing state. Therefore, ionization becomes an important factor affecting the lifetime of this upper state and widening the overall enhanced harmonic peak. The effect of which should become more and more prevalent as the laser pulse becomes longer because then the perturbation needed for ionization to take place lasts longer. As the laser pulse duration gets longer, we predict that the competition between spectral narrowing and widening due to ionization lifetime is what determines the actual width of the enhanced harmonic.

4.2.3 Cutoff Energy Analysis

The TD-ORMAS SD HH spectra of Mn and Mn^+ (dark green) are replotted in Fig. 4.9 along with TD-CASSCF fz. 2p HH spectrum of Mn^{2+} (cyan). In particular, this figure also shows the position of cutoff energies of Mn, Mn^+, and Mn^{2+} as red arrows. It is evident that the cutoff energies in Mn and Mn^+ HH spectra are both extended well beyond their own cutoff position approaching that of Mn^{2+}. This is a sign of a non-trivial production of the dications as a result of tunneling ionization. In fact, when one compares the intensity used in both simulations (3×10^{14} W/cm^2) with the barrier suppression intensities of 1.2×10^{13} W/cm^2 for Mn and 2.4×10^{14} W/cm^2 for Mn^+ (see Table 4.3), it is reasonable to expect almost complete removal of two electrons from the former and one electron from the latter during the course of interaction with the laser.

Looking at Mn^{2+} HH spectrum (cyan), however, one can see the harmonic intensity is actually too low to conclude that this extension in the HH responses from Mn and Mn^+ to be that of an ordinary three-step process. A similar effect has been observed and described in Ref. [67] where the extension of harmonic responses of a neutral 1D Be atom and its cation up to that of the dication is shown to be the result of electron correlation effect. In this mechanism a returning electron excites another electron in the dication core via Coulomb interaction to a higher orbital. The three-step process starting from this higher orbital is more easily initiated due to a lower potential barrier, thus increasing the HH contribution of the dication [67, 68, 107]. It is very likely that the same mechanism also applies in our results [69].

TD-ORMAS SD results for different laser parameters are presented in Fig. 4.9(c) and (d). Orbital subspace decomposition for Fig. 4.9(c) (Fig. 4.9(d)) is given in Fig. 4.2(d) (Fig. 4.2(e)) with

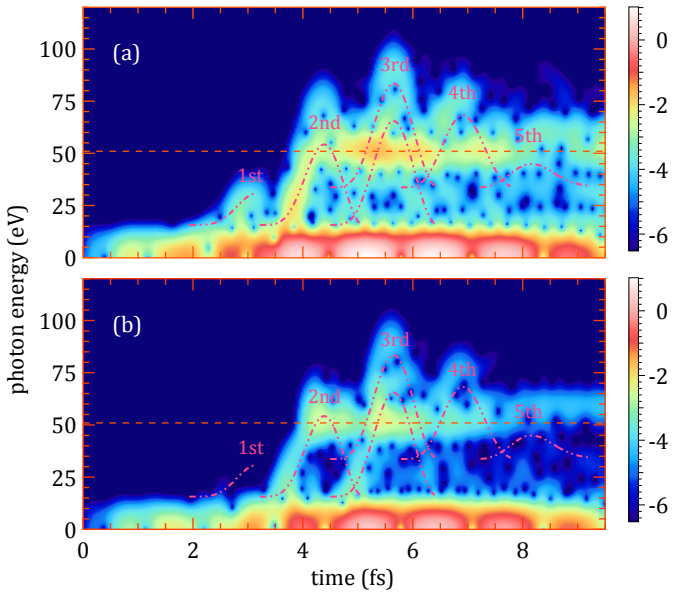

Figure 4.10: The time frequency spectrograms obtained using Gabor transform for (a) Mn and (b) Mn^+. The lower and upper groups of return energy curves are for Mn^+ and Mn^{2+}, respectively.

input parameters given in Input 4.5 (4.6). With three times lower intensity of 1×10^{14} W/cm^2 and somewhat longer wavelength 1333.7 nm (which are chosen so that the ponderomotive energy is constant), one sees that the enhanced harmonic around 51.5 eV is still produced. This demonstrate that resonant enhancement is an atomic process.

4.2.4 Time-Frequency Analysis

Mapping of the emission time of each harmonic frequency requires a two-dimensional function, the time-frequency spectrogram. Here we present a time-frequency analysis for Mn and Mn^+ HH responses in Fig. 4.10 with the classical return kinetic energy curves superimposed (compare the shape of these curves with Fig. 1.3(b)). The time-frequency sepctrograms are calculated using Gabor transform,

$$\begin{aligned} S(\tau,\omega) &= \left| \int_{-\infty}^{\infty} dt\; W(t,\tau) a(t) \exp(-i\omega t) \right|^2 \\ &= |\mathrm{FT}\left[W(t,\tau)a(t)\right]|^2 \end{aligned} \tag{4.1}$$

with $W(t,\tau)$ being a windowing function which is chosen to be of Gaussian form having unit amplitude and standard deviation $\sigma = 7.5$ a.u. of time,

$$W(t,\tau) = \exp\left(\frac{-(t-\tau)^2}{\sigma^2}\right). \tag{4.2}$$

The peak at 50.6 eV starts to appear during the second returning trajectory when the electron's return energy is close to this energy value. This suggests the following mechanism. When an electron has return energy matching the resonant energy, this electron is captured by an autoionizing state lying at 50.6 eV above the ground state. This electron then goes back to the ground state emitting the resonantly enhanced radiation [69].

In Fig. 4.10(a) and (b), the superimposed classical return energy curves are classified into two groups. The lower one corresponds to the return to Mn^+ while the upper one to the return to Mn^{2+}. The lower group is seen to last only up to the third returning bunch, whereas the upper group starts to become significant also from the third returning bunch and beyond. This behavior is in line with the ionic yields in Fig. 4.11(a) when the propagation starts from Mn and (b) when it starts from Mn^+ in which after about 6 fs, the yield of Mn^+ has practically diminishes. These simulations use Input 4.2 and Fig. 4.2(d) for Fig. 4.11(a) and 4.3 and Fig. 4.2(e) for Fig. 4.11(b).

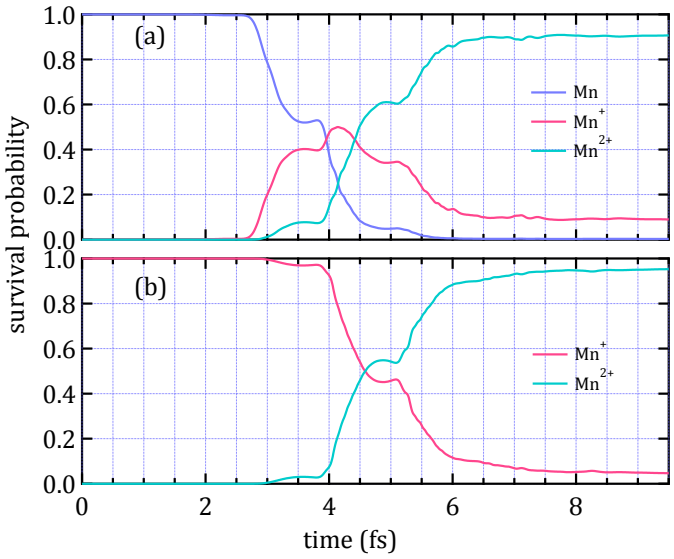

Figure 4.11: The yields of Mn, Mn^+, and Mn^{2+} when the simulation starts from (a) Mn and from (b) Mn^+. The peak intensity is $I_0 = 3 \times 10^{14}$ W/cm^2 and the wavelength is $\lambda_0 = 770$ nm.

4.3 Transition Analysis of High-Harmonic Spectra

One of the early theoretical models of high-harmonic generation is due to Lewenstein [23, 45] where the time-dependent wavefunction is assumed to be a superposition of ground state and continuum states. This model shows a good agreement with experimental observations, in particular the important features such as plateau and cutoff energy. In this model, the harmonic emission is related to the infinitely many transitions between a continuum state and the ground state.

In this section, we shall adopt a similar but mathematically distinct notion of transitions as those in the Lewenstein model for the analysis of high-harmonic spectra. We start from the time-dependent accelaration given in Eq. (3.69) [69]

$$a(t) = \sum_{pq} \langle \phi_p | \hat{a} | \phi_q \rangle \, D_p^q - N\mathscr{E}(t) - i\Delta(\dot{P}_z) \tag{4.3}$$

where

$$\hat{a}(\mathbf{r}) = -Z\frac{\cos\theta}{r^2}. \tag{4.4}$$

Looking at the first term in Eq. (4.3), each individual term is proportional to the matrix element of $\hat{a}$ whose coordinate representation is proportional to $\cos\theta$. Now, the orbitals appearing in (4.3) are the TDVP-optimized, time-dependent orbitals which are a linear combination of many spherical harmonics (Eq. (3.65)). If, on the other hand, these orbitals are fixed in time and furthermore have a definite angular momentum and its z-projection, it is possible to associate the quantity $\langle \phi_\mu | \hat{a} | \phi_\nu \rangle \, D_\mu^\nu$ to $\phi_\mu \leftrightarrow \phi_\nu$ transition because the angular integral of $\langle \phi_\mu | \hat{a} | \phi_\nu \rangle$ is governed by the usual dipole selection rules and the 1RDM D_μ^ν is, in some way, proportional to the populations of ϕ_μ and ϕ_ν. Such time-independent orbitals having fixed l and m values are easily satisfied by the initial orbitals, i.e. the ground state orbitals calculated by imaginary time relaxation. For the purpose of the present analysis, we will therefore expand $|\phi_\mu\rangle$ in Eq. (4.3) in terms of *all* initial orbitals, i.e. both occupied and virtual ones to ensure completeness [69]. In the following we will simplify the ket notation for orbitals so that $|\phi_\mu\rangle \to |\mu\rangle$ and use overbar to denote an initial orbital, i.e. $|\phi_{\bar{\mu}}\rangle = |\phi_\mu(t=0)\rangle \to |\bar{\mu}\rangle$. The transformed expression of (4.3), neglecting the second and last terms which do not bear any special feature near the resonant energy, reads

$$a(t) = \sum_{\bar{\mu}\bar{\nu}} \langle \bar{\mu} | a | \bar{\nu} \rangle + \sum_{pq} \langle \bar{\nu} | q \rangle \, D_p^q \, \langle p | \bar{\mu} \rangle \tag{4.5}$$

where we recall that indices p, q are used for general occupied orbitals.

Starting from Eq. (4.5), we will split the summations over $\bar{\mu}$ and $\bar{\nu}$ into initial orbitals occupied in Hartree-Fock configuration (denoted by $\mathcal{HF}$ set) and those which are not (denoted by $\mathcal{V}$ set),

$$\sum_{\bar{\mu}} \rightarrow \sum_{\bar{\mu}\in\mathcal{HF}} + \sum_{\bar{\mu}\in\mathcal{V}} .$$

This division is based on the occupation of ground state orbitals where we noticed that the probability (i.e. $|C_I|^2$) corresponding to Hartree-Fock configuration in our MCSCF-optimized ground state to be r where r never drops below 0.95. Therefore, the occupation number of orbitals making up the Hartree-Fock configuration is always bigger than r whereas the occupation of those not included in this configuration must be smaller than $2(1-r)$. Applying this division on the Eq. (4.5),

$$a(t) = a_1(t) + a_2(t) + a_3(t) \tag{4.6}$$

where

$$a_1(t) = \sum_{\bar{\mu},\bar{\nu}\in\mathcal{HF}} \langle\bar{\mu}|\mathcal{a}|\bar{\nu}\rangle\, D^{\bar{\nu}}_{\bar{\mu}} = \frac{1}{2}\sum_{\bar{\mu}\in\mathcal{HF}} \alpha(\bar{\mu},\bar{\mu},t) + \sum_{(\bar{\mu}>\bar{\nu})\in\mathcal{HF}} \alpha(\bar{\mu},\bar{\nu},t) \tag{4.7a}$$

$$a_2(t) = 2\,\mathrm{Re}\left\{\sum_{\bar{\mu}\in\mathcal{HF}}\sum_{\bar{\nu}\in\mathcal{V}} \langle\bar{\mu}|\mathcal{a}|\bar{\nu}\rangle\, D^{\bar{\nu}}_{\bar{\mu}}\right\} = \sum_{\bar{\mu}\in\mathcal{HF}} \beta(\bar{\mu},t) \tag{4.7b}$$

$$a_3(t) = \sum_{\bar{\mu},\bar{\nu}\in\mathcal{V}} \langle\bar{\mu}|\mathcal{a}|\bar{\nu}\rangle\, D^{\bar{\nu}}_{\bar{\mu}} \tag{4.7c}$$

$$\alpha(\bar{\mu},\bar{\nu},t) = 2\,\mathrm{Re}\left\{\langle\bar{\mu}|\hat{\alpha}|\bar{\nu}\rangle\, D^{\bar{\nu}}_{\bar{\mu}}\right\} \tag{4.7d}$$

$$\beta(\bar{\mu},t) = 2\,\mathrm{Re}\left\{\sum_{p,q}\langle\bar{\mu}|\hat{\alpha}|q\rangle\, D^{q}_{p}\,\langle p|\bar{\mu}\rangle\right\} - \sum_{\bar{\nu}\in\mathcal{HF}} \alpha(\bar{\mu},\bar{\nu},t) \tag{4.7e}$$

$$D^{\bar{\mu}}_{\bar{\nu}} = \sum_{pq}\langle\bar{\nu}|q\rangle\, D^{q}_{p}\,\langle p|\bar{\mu}\rangle\,. \tag{4.7f}$$

Notice that if the initial orbitals have a definite angular momentum and hence a definite parity, then $\alpha(\bar{\mu},\bar{\mu},t) = 0$ due to parity restriction.

In the subsequent analysis, we will rely on the quantities $\alpha(\bar{\mu},\bar{\nu},t)$, $\beta(\bar{\mu},t)$, and their power spectra to disentangle the contributions of various orbital transitions. Thanks to the dipole selection rules, for a given set of initial orbitals, the number of important orbital pairs $(\bar{\mu},\bar{\nu})$ and hence $\alpha(\bar{\mu},\bar{\nu},t)$'s can be substantially reduced. Considering which matrix elements of $\mathcal{a}$ are involved in $a_1(t)$ (or $\alpha(\bar{\mu},\bar{\nu},t)$), $a_2(t)$ (or $\beta(\bar{\mu},t)$), and $a_3(t)$, one may therefore interpret them to be the contributions from bound-bound, bound-virtual, and virtual-virtual transitions, respectively, to the total HH spectrum. Specifically, we will analyze and compare the features exhibited by the power spectrum of these transition contributions to arrive at the answer about which transition is responsible for the 50 eV enhancement in Mn plasma.

4.3.1 Contribution of Individual Transitions to The Resonant Energy

In Section 4.2.2, it was found that freezing $3s$ and $3p$ leads to the disappearance of the enhancement at 50.6 eV. While this behavior reveals the multi-electron nature of the enhancement origin (since the orbitals being frozen, $3p$, are core orbitals), we have yet to establish the upper orbitals with which $3p$ are coupled in the transitions that prompt enhancement mechanism. Moreover, in Mn^+ there are some other levels that actually lie in the vicinity of the resonant peak, involve $3p$ orbitals, and also have the same spin multiplicity as the ground state. These are the multiplet levels of $3d^5 4s^2(^7P)$, that is, one electron is excited from $3p$ to $4s$, whose energies fall in the narrow range 49.5 - 50.4 eV (see Table I in Ref. [106]).

Employing orbital subspace decompositions given in Fig. 4.2(d) and Input 4.2 for Mn and in Fig. 4.2(e) and Input 4.3 for Mn^+, we performed an analysis of the transitions responsible for the enhancement. With orbitals set given in Fig. 4.2(d) (or (e)), one should identify 18 selection rules-obeying pairs for both ionic species (the pairs involving frozen orbitals $1s, 2s, 2p_{0,\pm1}$ are not taken into account as the corresponding density matrix elements $D^{\bar{\mu}}_{\bar{\nu}}$ vanish), and since $\mathcal{HF}$ sets

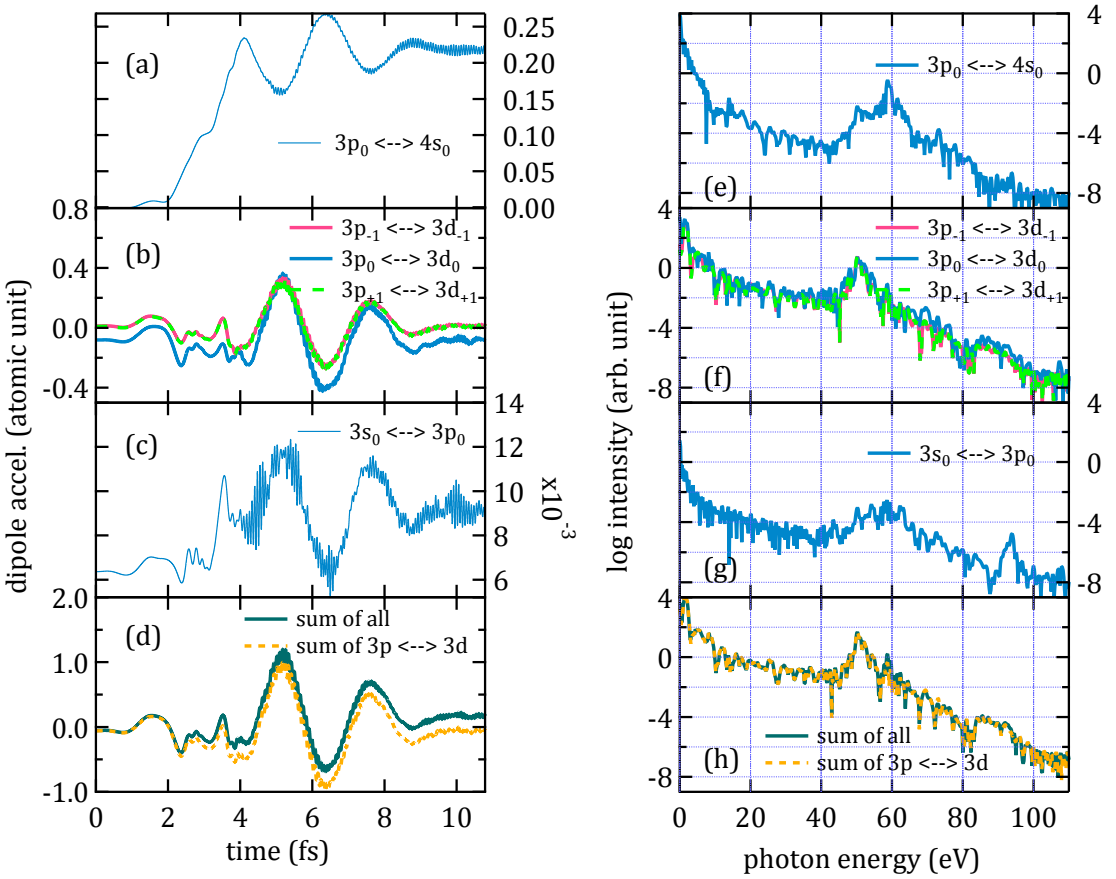

Figure 4.12: $\mathcal{HF}$ transitions in time domain (a)-(c) and the corresponding power spectra (e)-(g) in neutral Mn. The sum of $3p-3d$ transitions and of all $\mathcal{HF}$ transitions are plotted in (d) and their spectra in (h).

of Mn and Mn^+ comprise $\{1s, 2s, 2p_{0,\pm1}, 3s, 3p_{0,\pm1}, 4s, 3d_{0,\pm1,\pm2}\}$, five pairs among them are members of $\mathcal{HF}$ transition set,

$$\begin{aligned} &3s \leftrightarrow 3p_0 \\ &3p_{0,\pm1} \leftrightarrow 3d_{0,\pm1} \\ &3p_0 \leftrightarrow 4s. \end{aligned} \tag{4.8}$$

While the rest couple either $\mathcal{HF}$ with $\mathcal{V}$ or $\mathcal{V}$ with $\mathcal{V}$,

$$\begin{aligned} &4s \leftrightarrow 4p_0 \\ &4p_{0,\pm1} \leftrightarrow 4d_{0,\pm1} \\ &3s \leftrightarrow 4p_0 \\ &3p_{0,\pm1} \leftrightarrow 4d_{0,\pm1} \end{aligned} \qquad \begin{aligned} &3p_0 \leftrightarrow 5s \\ &3d_{0,\pm1} \leftrightarrow 4p_{0,\pm1} \\ &4p_0 \leftrightarrow 5s. \end{aligned} \tag{4.9}$$

The subscript denotes the magnetic quantum number.

In the present section, we will first concentrate the analysis on $a_1(t)$ and its power spectrum. We have confirmed that the initial orbitals used in this analysis have a definite angular momentum. Thus according to Eq. (4.7d), the first term of (4.7a) vanishes, leaving only the second one which is the sum of the five transitions in list (4.8) above.

The temporal domain oscillation, i.e. $\alpha(\bar{\mu}, \bar{\nu}, t)$, as well as the corresponding power spectrum for the five $\mathcal{HF}$ transitions in Mn and Mn^+ are presented in Fig. 4.12 and Fig. 4.13, respectively. As seen from panel (f) of these figures, the three three $3p \leftrightarrow 3d$ transition spectra individually exhibit a prominent peak at 52.2 eV. The sum spectrum of these three $3p \leftrightarrow 3d$ transitions components and the sum of all five $\mathcal{HF}$ transitions are also plotted in Fig. 4.12(h) and 4.13(h). The enhanced peak at 52.2 eV in the $3p \leftrightarrow 3d$ transitions sum perfectly coincides that in the all-$\mathcal{HF}$ -transitions sum in Fig. 4.12(h) and 4.13(h). More importantly, one may also compare the shape of the peaks

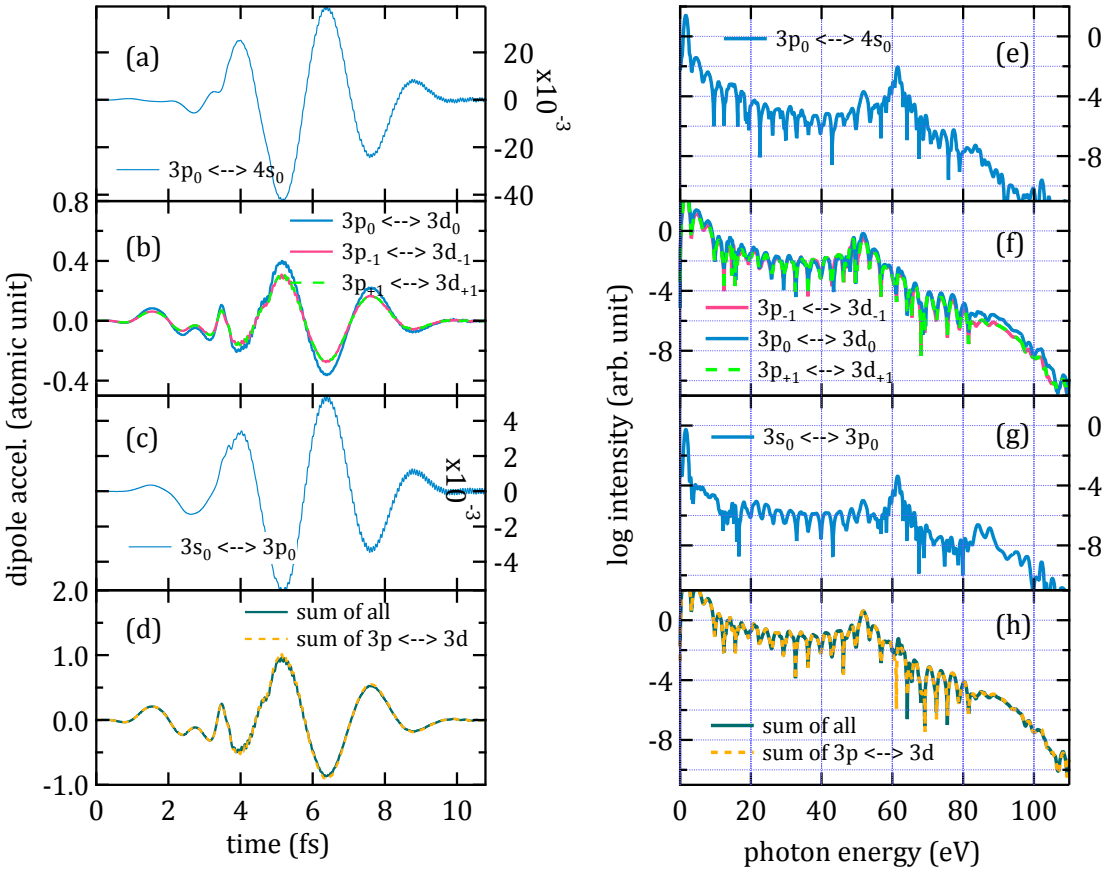

Figure 4.13: $\mathcal{HF}$ transitions in time domain (a)-(c) and the corresponding power spectra (e)-(g) in Mn^+. The sum of $3p-3d$ transitions and of all $\mathcal{HF}$ transitions are plotted in (d) and their spectra in (h).

at and around the resonant energy between all-$\mathcal{HF}$ -transition sum and the HH spectrum for each ionic species (the dark green spectrum in Fig. 4.9(a) and (b)), they are seen to be in a very good agreement as well. This signifies that the emission around the resonant energy is exclusively driven by the electronic dynamics occurring between $3p$ and $3d$ orbitals.

Upon a closer look at the individual $3p \leftrightarrow 3d$ transition spectra, each of them actually exhibits another peak at 48.1 eV, of similar magnitude as the resonant 52.2 eV peak in the $3p_0 \leftrightarrow 3d_0$ spectrum. However, upon summing the three transitions $3p \leftrightarrow 3d$, the 48.8 eV peak gets suppressed whereas the 52.2 eV one is enhanced, indicating that these $3p \leftrightarrow 3d$ transition components are only in phase at the resonant energy. In this sense, the enhancement may then be viewed as being the result of a constructive superposition among transition components between the pair of orbitals coupled in resonance. To demonstrate that the agreement between $3p \leftrightarrow 3d$ transitions and the total HH emission also prevails in time domain, a separate simulation was run using TD-CASSCF fz. $2p$ (Fig. 4.2(b)) and laser pulse shape as shown in Fig. 4.14(a) on the target system Mn^+. The spectrogram of the total $3p \leftrightarrow 3d$ transitions obtained by replacing $a(t)$ with $\sum_{m=0,\pm1} \alpha(3p_m, 3d_m, t)$ in Eq. (4.1) (Fig. 4.14(b)) shows a very good one-to-one correspondence in the emission times with the total HHG spectrogram (Fig. 4.14(c)).

Another noticeable feature from the spectra in Fig. 4.12 and Fig. 4.13 is the peak at 61.6 eV in $3p_0 \leftrightarrow 4s_0$ spectra ($3s_0 \leftrightarrow 3p_0$ spectra also exhibit this peak but at much lower intensity). This 61.6 eV peak in $3p_0 \leftrightarrow 4s_0$ spectrum is clearly responsible for the peak at the same energy in Mn spectra in Fig. 4.8(a). However, looking at the excitation spectra in Fig. 4.7(a), one sees that the strongest line at 61.6 eV is possessed by Mn^{2+}. Mn also has a smaller line at a slightly higher energy, but the corresponding oscillation in time is seen to be most dominant after the dication takes over the neutral (compare Fig. 4.12(a) with Fig. 4.11(a)). Therefore, one may attribute this 61.6 eV peak to the $3p_0 \leftrightarrow 4s_0$ transition line from the dication.

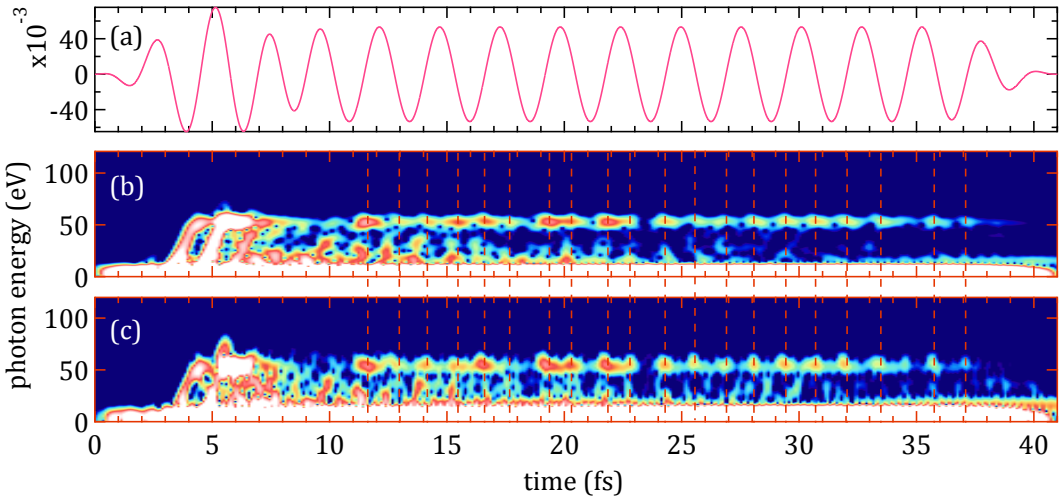

Figure 4.14: Resonant emission times in Mn^+: (a) The laser electric field with intensity in the leading sine-squared portion being 1×10^{14} W/cm^2 and that in the flat one 1×10^{14} W/cm^2. The center wavelength is 770 nm. (b) The time-frequency spectrogram of the total $3p \leftrightarrow 3d$ transitions. (c) The time-frequency spectrogram of the HHG.

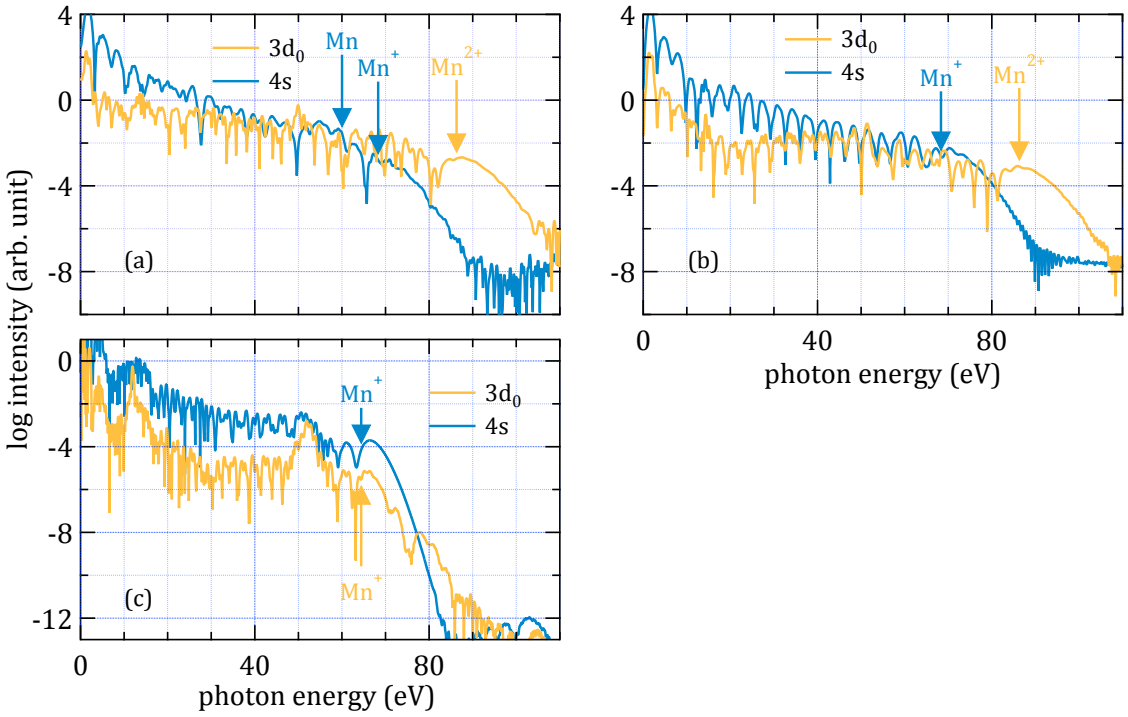

Figure 4.15: The spectra of $\beta(3d_0, t)$ and $\beta(4s, t)$ in (a) Mn and (b) Mn^+ using 3×10^{14} W/cm^2 intensity and 770 nm wavelength. Panel (c) shows the spectra of $\beta(3d_0, t)$ and $\beta(4s, t)$ in Mn^+ when the intenisty is much lower 5×10^{13} W/cm^2, with 1820 nm wavelength.

4.3.2 Bound-Virtual Orbital Dynamics

In this section, we will momentarily digress from the main topic of this dissertation in order to discuss another spectral feature resolvable by means of the decomposition of total acceleration into transitions. For this purpose, we shall examine the bound-virtual part, $a_2(t)$, of the total acceleration $a(t)$. It will be shown that using the spectrum of $\beta(\bar{\mu}, t)$ (Eq. (4.7e)), it is possible to discern the signature of ionic states that contribute to the total harmonic emission for a given starting ionic species. Using Input 4.2 plus orbital subspace decompositions of Fig. 4.2(d) , the

power spectra of $\beta(3d_0, t)$ and $\beta(4s, t)$ when the simulation starts from Mn are presented in Fig. 4.15(a). The same spectra obtained when the simulation starts from Mn^+ are shown in Fig. 4.15(b) where Input 4.3 plus Fig. 4.2(e) have been used. Whether in Fig. 4.15(a) or (b), it is seen that $\beta(3d_0, t)$ and $\beta(4s, t)$ spectra have clearly different cutoff energies even although they are calculated for the same starting ionic species. In particular, the cutoff of $\beta(4s, t)$ is close to the starting ionic species's cutoff (59.99 eV for Mn and 68.32 eV for Mn^+) while that of $\beta(3d_0, t)$ is close to the dication's cutoff (86.44 eV).

This observation leads to the idea that the spectra of $\beta(4s, t)$ and $\beta(3d_0, t)$ are dominated by the starting species and the dication, respectively. This behavior may be explained using the fact that for a given atomic species, it is the valence eletrons which are subjected to the highest probability of undergoing three-step process. Within Hartree-Fock picture, $4s$ orbital is the valence shell for both Mn and Mn^+ and $3d$ is the valence shell for the Mn^{2+}. Referring to how $\beta(\bar{\mu}, t)$ is defined in Eq. (4.7e), one may picture the underlying process such that recombinations from continuum states (contained in $\mathcal{V}$) to $\phi_{\bar{\mu}}$ orbital are all encoded in $\beta(\bar{\mu}, t)$. Hence, during the early portion of the laser where ionization is still negligible, most recombinations occur in the valence orbital of the starting species and the cutoff is associated with this species as well. As the laser amplitude is rising, the two electrons from Mn and one electron from Mn^+ are tunnel-ionized from $4s$ (see Fig. 4.16(e) and Fig. 4.17(e) below) making $3d$ the valence shell for the newly formed Mn^{2+}. Then the recombination process is repeated except that from this point on the three-step electron recombines into $3d_0$ orbital (the laser is polarized in z-direction and $3d_0$ orbitals have nonzero probability in this direction), hence the cutoff is close to that of Mn^{2+}.

To demonstrate that the difference in cutoff positions of $\beta(3d_0, t)$ and $\beta(4s, t)$ spectra exhibited in Fig. 4.15(a) and (b) is really due to ionization, we run a simulation on Mn^+ with a laser having substantially lower intensity of 5×10^{13} W/cm^2 and 1820 nm center wavelength (Input 4.4 and Fig. 4.2(b) fz. $2p$), and present the result in Fig. 4.15(c). As can be expected, the intensity used this time is too weak to induce significant ionization in Mn^+ from $4s$ orbital and consequently the cutoff of $\beta(3d_0, t)$ does not extend up to the cutoff for Mn^{2+}.

4.4 The Dynamics of Orbital Population in the Presence of Resonant Enhancement

In the preceding section, we have learned that the transition spectra between pairs of orbitals can provide us a deeper insight into the origin of the enhancement in terms of inter-orbital transitions and as a side-result, the signature of the contribution from higher ionic states can also be extracted from some of these spectra. Given these observations thus far, it should become clear by now that the resonant enhancement in HH spectra is strongly concomitant with orbital dynamics. With this in mind, in this section an analysis of dynamics taking place in the initial orbitals based on the orbitals' population will be presented.

Orbital population $n(\mu, t)$ is defined to be the diagonal matrix elements of 1RDM, i.e. $n(\mu, t) = D^{\mu}_{\mu}$ (see the definition immediately following Eq. (3.36)). One property of $n(\mu, t)$ is that it is always a positive semi-definite number less than two, $0 \leq n(\mu, t) \leq 2$, regardless of the choice of bases ϕ_μ. In the present analysis, we shall analyze the temporal evolution of the population of initial orbitals, $n(\bar{\mu}, t)$. Using Input 4.1 and orbital subspace decompositions of Fig. 4.2(a) fz. $2p$ for Mn, we calculate the time-dependent orbital population of $\mathcal{HF}$ initial orbitals and show them in Fig. 4.16(b)-(e). The population of frozen orbitals are not included here since their value always equals two.

As Fig. 4.16(b)-(e) reveals, the population of all orbitals except $4s$ returns approximately to their respective initial values. The population of $4s$ orbital, however, is depleted almost completely, something to be expected given that $4s$ is the least bound (see Table 4.1) and it has nonzero probability in the z direction. The binding strength of the orbitals can also be deduced from Fig. C.1 where it is seen that $4s$ has the farthest radial span among $\mathcal{HF}$ orbitals.

The virtual panel in Fig. 4.16(f) shows the total population of virtual orbitals in $\mathcal{V}$, it is calculated as

$$n_{\mathcal{V}}(t) = N - \sum_{\bar{\mu} \in \mathcal{HF}} n(\bar{\mu}, t). \tag{4.10}$$

Where N is the number of electrons. The total population of virtual orbitals exhibit a rise within

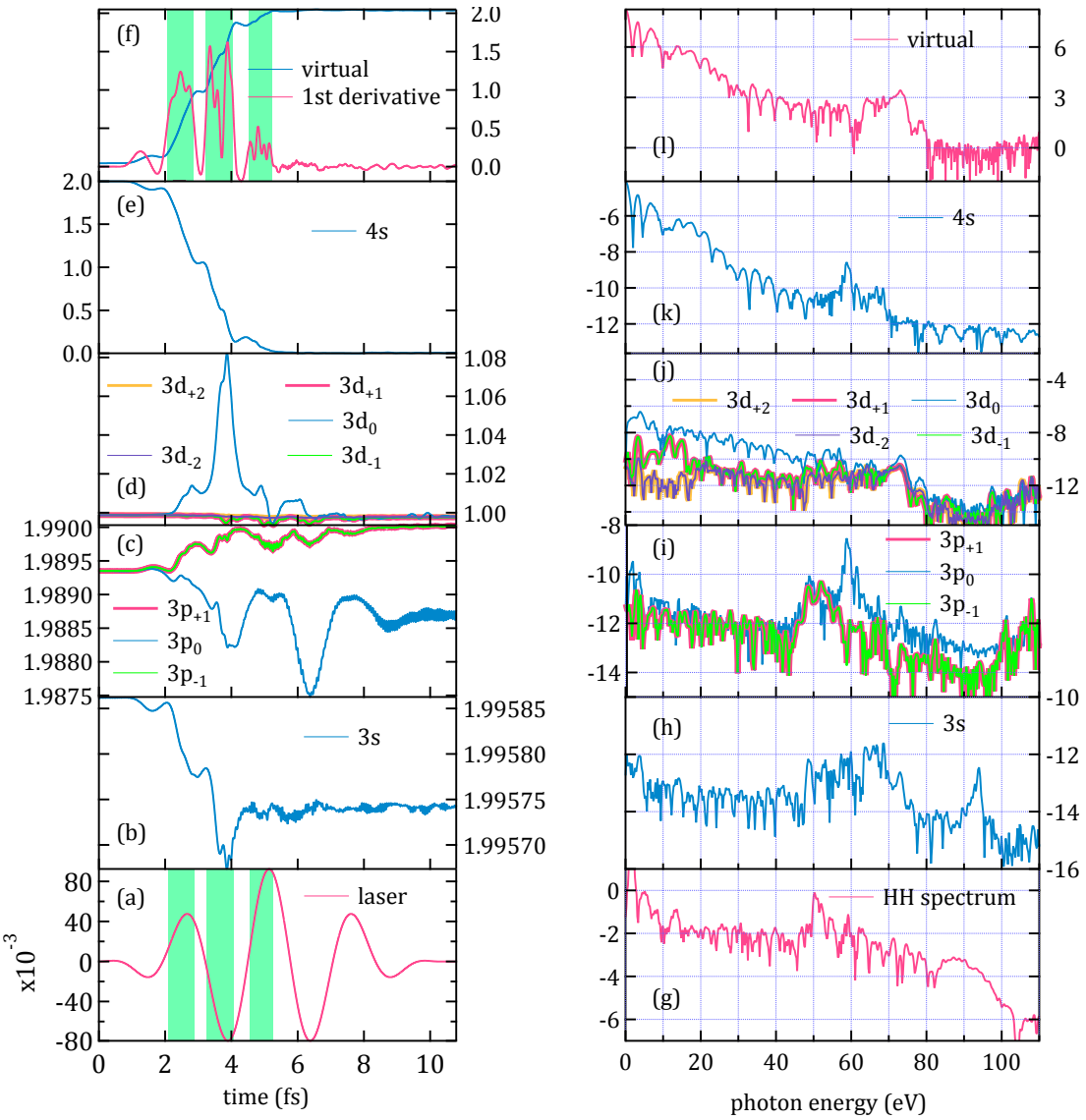

Figure 4.16: Orbital population dynamnics in neutral Mn. The temporal evolution of $\mathcal{HF}$ orbital populations are shown in (b)-(e) while (f) shows the total population of $\mathcal{V}$ orbitals and its first derivative. Panels (h)-(l) show the spectra of the first time derivative in the corresponding left-hand panel. The green shaded regions mark the times when ionized electrons will not go back to the core.

2.0 – 5.5 fs interval, the same time interval needed for 4*s* population to "settle". Upon a closer look, one sees that $n_{\mathcal{V}}(t)$ rises in a stepwise fashion, the slope is positive during three time windows: 2.1 – 2.8 fs, 3.2 – 4.1 fs, and 4.5 – 5.2 fs (indicated by the shaded areas). Based on a classical trajectory analysis, these time windows are around laser phases at which ionized electrons will not return to the parent core (compare the green shaded regions in Fig. 4.16(a) and (f)), in other words, the ionization dynamics are encoded within this time window. The first derivative of $n_{\mathcal{V}}(t)$ is plotted in the same panel as $n_{\mathcal{V}}(t)$ where one sees three groups of peak, each of these peak corresponds to a removal of electrons from the starting ionic species, i.e. neutral Mn. The first rising interval represented by the first peak in the derivative is small in magnitude because the laser amplitude at this time is still low. As the laser amplitude increases, more electrons are tunnel-ionized resulting in the highest second peak in the derivative. The laser is still increasing but much of the electrons in 4*s* have been removed, resulting in the third low peak. The total number of electron loss from 4*s* amounts to 1.99 indicating that at the end of the interaction we are left with Mn^{2+}.

We also perform a frequency domain analysis in Fig. 4.16(h)-(l) by calculating the Fourier transforms of the first derivative of orbital populations in Fig. 4.16(b)-(f). The spectra of 3*d* populations (Fig. 4.16(j)) exhibit a plateau-like structure reminiscent of that found in HH spectra with

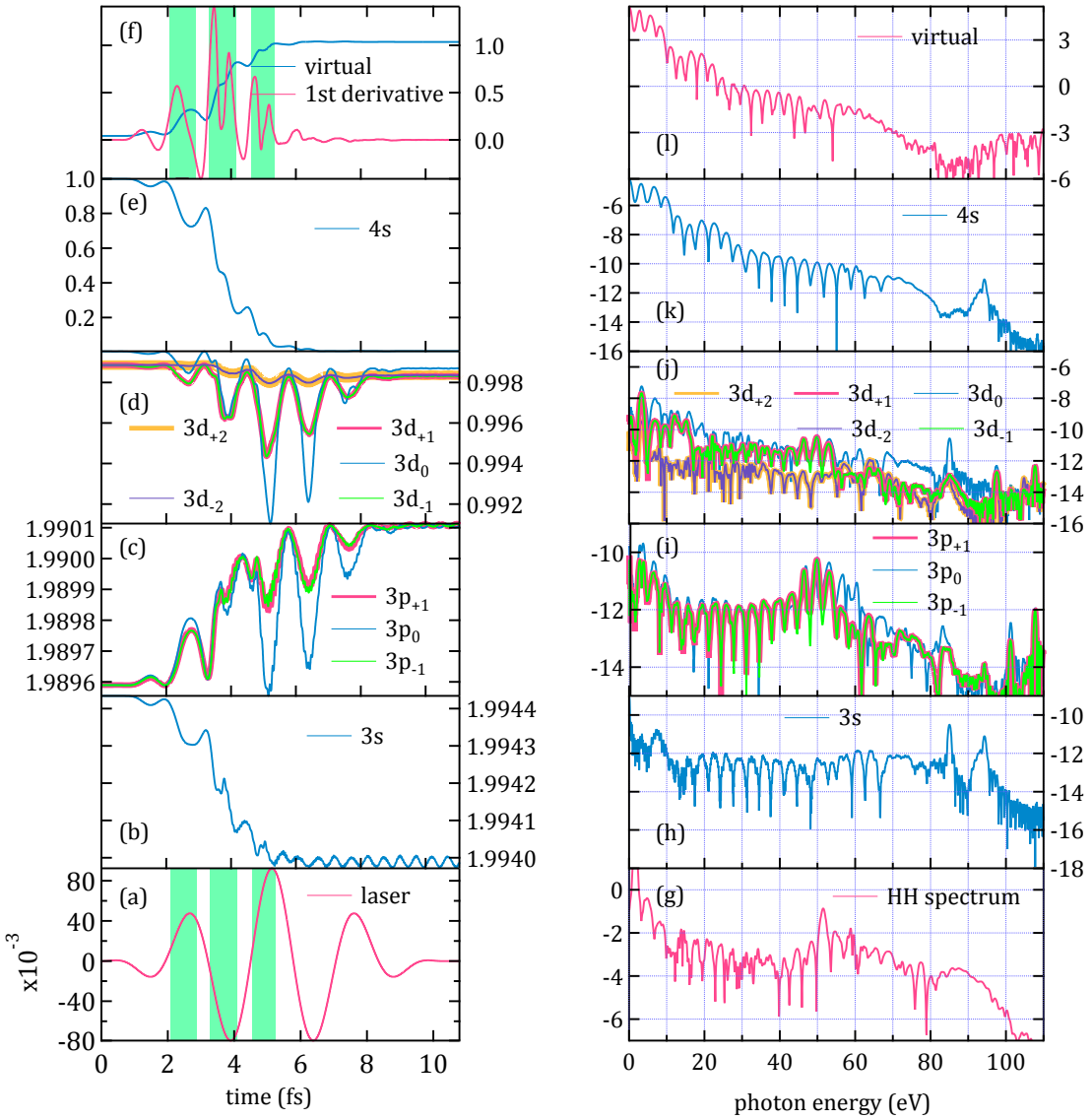

Figure 4.17: Orbital population dynamnics in Mn^+. The temporal evolution of $\mathcal{HF}$ orbital populations are shown in (b)-(e) while (f) shows the total population of $\mathcal{V}$ orbitals and its first derivative. Panels (h)-(l) show the spectra of the first time derivative in the corresponding left-hand panel. The green shaded regions mark the times when ionized electrons will not go back to the core.

$3d_0$ having the clearest plateau structure. The reason is, $3d_0$ orbital posses non-zero probability in the z-direction, the direction of laser field, and are therefore coupled strongly to the laser. The most interesting feature, however, is exhibited by $3p$ and $3d_{0,\pm1}$ orbital populations, their spectra are seen to have some distinguishable peaks in the vicinity of the resonant energy 51.5 eV. This implies that in time domain, the populations $n(3p_{0,\pm1}, t)$ and $n(3d_{0,\pm1}, t)$ are modulated at these frequencies. Comparing the spectra of $\partial_t n(3p_0, t)$ and of $\partial_t n(3p_{\pm1}, t)$, one can see the presence of 61.6 eV peak in the former, but not in the latter. Referring back to Fig. 4.12(e), this 61.6 eV peak can be attributed to the peak at the same energy in $\alpha(3p_0, 4s, t)$ spectrum. To stress, $3p_{\pm1}$ orbitals are not coupled by transitions having a strong line at this energy while the spectra of $\partial_t n(3p_{\pm1}, t)$ do not have this peak either. These observations allow us to draw a connection between the presence of strong features in the transition spectra ($\alpha(\bar{\mu}, \bar{\nu}, t)$) and the modulation at the same energies in the time-dependent population $n(\bar{\mu}, t)$ or $n(\bar{\nu}, t)$. The peak around 93 eV found in the spectrum of $\partial_t n(3s, t)$ (Fig. 4.16(h)) and of $\alpha(3s, 3p_0, t)$ (Fig. 4.12(g)) may serve as another evidence of this correlation between population of an orbital and transition involving that orbital.

A parallel analysis on the orbital dynamics in Mn^+ was also performed and is presented in Fig. 4.17. Some of the features in the population dynamics (Fig. 4.17(b)-(f)) are shared with Mn

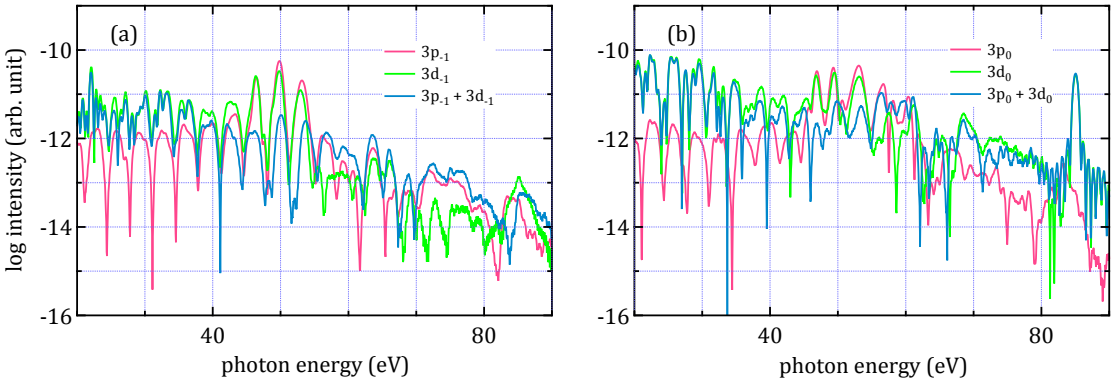

Figure 4.18: The spectra of $\partial_t(n(3p_m,t)+n(3d_m,t))$ when (a) $m=-1$ and (b) $m=0$.

case before, such as ionization dynamics imprinted in the slope of the rising section of $n_{\mathcal{V}}(t)$ (Fig. 4.17(f)) and the depletion of $4s$ orbital (Fig. 4.17(e)). Some enhanced peaks are also clearly present around the resonant energy 51.5 eV in the spectra of $\partial_t n(3p_{0,\pm1},t)$ (Fig. 4.17(i)) and $\partial_t n(3d_{0,\pm1},t)$ (Fig. 4.17(j)), to be compared with the 51.5 eV enhanced peak in the spectra of $\alpha(3p_{0,\pm1},3d_{0,\pm1},t)$ (Fig. 4.13(f)). Fig. 4.18(a) and (b) demonstrates what happens when a time-dependent population from Fig. 4.17 (expressed in terms of its derivative) $\partial_t n(3p_m,t)$ is summed with $\partial_t n(3d_m,t)$. In Fig. 4.18(a) for $m=-1$ and in Fig. 4.18(b) for $m=0$. The clearest feature seen in the summed spectra (blue) is the suppression of the three peaks which were associated with the 51.5 eV resonant enhancement. This tells us that the modulations at this energy in $n(3p_m,t)$ and $n(3d_m,t)$ are nearly out of phase one from another - whenever there is a peak in $n(3p_m,t)$ there will be a valley in $n(3d_m,t)$, a clear indication of an alternating population exchange between the two orbitals.

One more feature that is clearly exhibited by $3d$ orbitals and $3p$ orbitals is the half-period spaced dips in Fig. 4.17(d) and (e). These dips account for an oscillating polarization of the atom (that is, the displacement of the center of gravity of the electron cloud) that follows laser oscillation. Under no influence of external field, the atomic probability density should be spherical. When a distortion is imparted to the atom, the orbital population will respond in a way that results in a modification of the probability function such that it follows the distorting force[1].

4.5 Summary

In this chapter, we have demonstrated the success of TD-CASSCF and TD-ORMAS methods in reproducing resonant enhancement from Mn, Mn^+, and Mn^{2+} at 51.5 eV, which is close to the experimental value. A large transition line at the same energy in the excitation spectra of the three ionic species are also reproduced, strongly suggesting that this 51.5 eV enhancement in HH spectrum can be connected to a highly favorable transition at the same energy. By varying frozen orbital space, it is found that when $3p$ orbitals are frozen, the 51.5 eV enhancement disappears. The subsequent analyses are based on the dynamics ensuing in the initial orbitals in terms of orbital transitions and populations. Orbital transition study reveals that the spectra of $3p_{0,\pm1} \leftrightarrow 3d_{0,\pm1}$ also exhibit a distinguished peak at 51.5 eV and the coherent sum of these three transitions resulted in an enhancement of the 51.5 eV harmonic with harmonic peak shapes that are in good agreement with that in the HH spectra. This observation allows us to conclude that the 51.5 eV enhancement in Mn plasma to be the result of a constructive interference between $3p-3d$ transitions. Realizing the crucial involvement of orbitals in the enhancement process, an analysis based on orbital population are performed from which one understands that strong features in the transition spectra between a certain pair of orbitals imply a temporal modulation at the same energy in the population of the orbitals involved. This modulation in populations of the two orbitals being coupled are in synchrony such that a peak in one population implies a valley in the other population, i.e. a periodic population exchange. The employed orbital-based studies can also be used to study ionization dynamics during laser interaction. In particular, information

[1]We have run a simulation on the same system but with much lower laser intensity of 5×10^{13} W/cm^2 such that ionization is negligible. We observed that basically the population of all orbitals exhibit an oscillating structure at half-laser period and the dipole moment follows the laser almost perfectly.

about what the highest charge state is that contributes to the total HHG and the dynamics of electron removal from the starting ionic species can be extracted.

Chapter 5

Resonant High-Harmonic Generation from Cr and In Plasmas

As discovered experimentally, high-harmonic generation exhibiting resonantly enhanced structure covers a wide range of atomic numbers. Atoms having electrons twice as large as the system considered in Chapter 4, manganese ($Z = 25$), such as indium ($Z = 49$), stannum ($Z = 50$), and stibium ($Z = 51$) have also been reported to generate enhanced harmonics. In this chapter, HH simulation results using indium and chromium ($Z = 24$) are presented and analyzed. This chapter may also serve as a demonstration of the capability of TD-CASSCF to handle large atomic systems, with resonant enhancement as the main subject of analysis.

5.1 Resonant High-Harmonic Generation from Indium and Its Cations

In the first half of this chapter, resonant enhancement in HHG from indium and its cations simulated using TD-CASSCF is presented and discussed.

5.1.1 Simulation Conditions

The ground state electronic configurations of In, In^+, and In^{2+} are provided in Table 5.1. With ~ 50 number of electrons, In, In^+, and In^{2+} pose a real challenge for MCTDHF (that is, when all orbitals are treated active) to obtain the *ab initio* HH spectra when a sufficient number of additional orbitals (more than those present in the electronic configurations in Table 5.1) is desired. This is where the flexibility offered by TD-CASSCF in setting some orbitals to be frozen comes in handy. Therefore, orbital subspace decompositions displayed in Fig. 5.2 where at least 14 orbitals are frozen are employed for the HH calculations from these three ionic species. This necessitates the corresponding ground state to be obtained using orbital subspace decompositions as shown in Fig. 5.1. Unlike in Mn and Cr (in Section 5.2 below), we do not perform TD-ORMAS calculations

Table 5.1: Experimental ionization potential I_p, barrier-suppression intensity I_{BS}, and the ground-state configuration of In, In^+, and In^{2+}.

	In	In^+	In^{2+}
I_p[a]	5.79	18.87	28.03
I_{BS}[b]	4.5×10^{12}	5.1×10^{14}	2.5×10^{15}
GS[c]	$[Kr]4d^{10}5s^25p^1(^2P_{1/2})$	$[Kr]4d^{10}5s^2(^1S_0)$	$[Kr]4d^{10}5s(^2S_{1/2})$

[a] Experimental ionization potential in eV [108, p. 10.179].
[b] Barrier-suppression intensity in W/cm^2.
[c] Ground state configuration, In and In^+ in Ref. [109, p. 1766] and In^{2+} in Ref. [110].

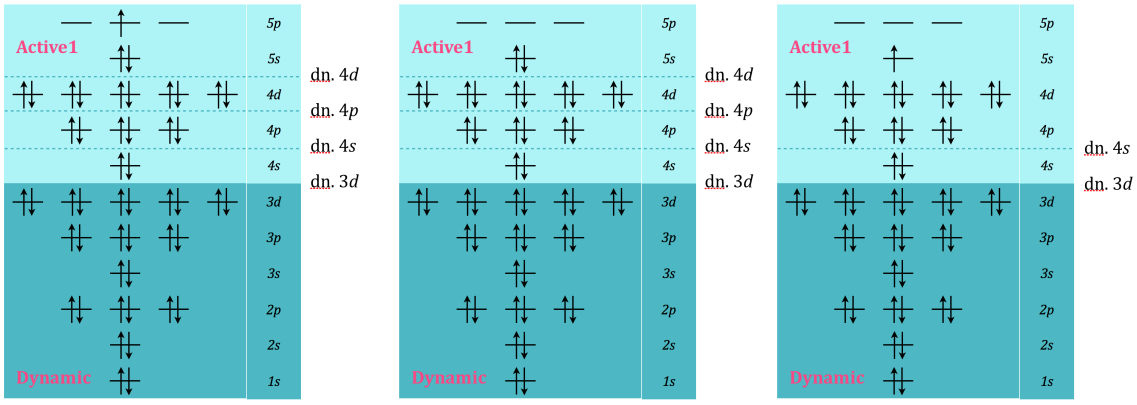

Figure 5.1: Orbital subspace decompositions used to calculate the ground states of In, In^+, and In^{2+} in the present chapter.

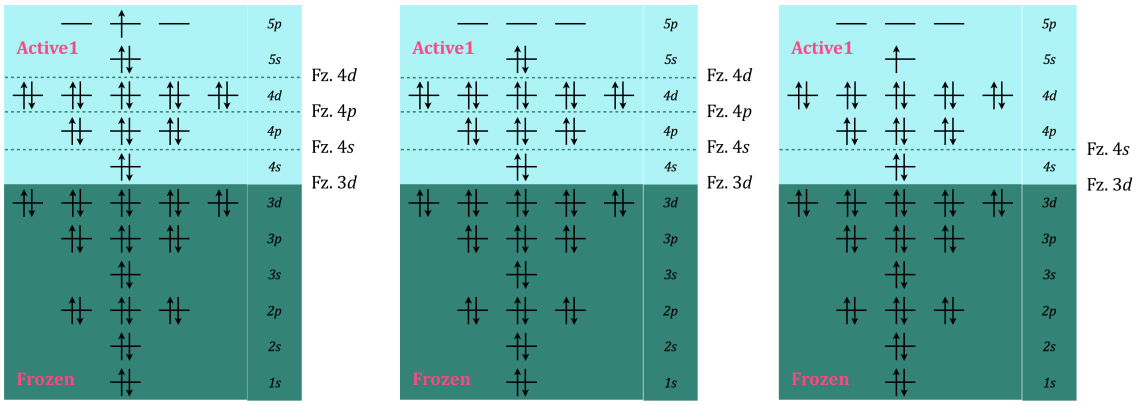

Figure 5.2: Orbital subspace decompositions used to perform HH simulations on In, In^+, and In^{2+} in the present chapter.

on In and its cations because with the number of vacant $5p$ spin-orbitals (see Fig. 5.1) these species have, TD-CASSCF is alreadcy sufficient to generate a moderate number of determinants (see Table 5.2).

The ground state energies, orbital energies, and number of determinants resulting from various orbital diagrams in Fig. 5.1 are presented in Table 5.2. From Table 5.2, one sees that the energy differences between $4s$ and $3d$ in In, In^+, and In^{2+} are 300 eV, way higher than the cutoff energies resulting from laser parameters chosen in the simulations in this section. This should justify our choice in never setting any orbitals below $4s$ in these ionic species to be active. We would like to note that the angular momentum of orbitals in neutral In ground state calculations is not definite. This behavior often appears when the electron occupation in the atom is something other than full or half-full, which is equivalent to the total angular momentum being unequal to zero (S state). Therefore, in orbital denomination for In in Table 5.2, the angular momentum part is to be understood as a quasi angular momentum. The radial grids employed for all ground state simulations except for dn. $4d$ on In, In^+, and In^{2+} are given in Table 5.4. For dn. $4d$ simulations, radial grids in Table 5.5 are used. The HH calculations performed on these ionic species are performed using simulation parameters in Input 5.1 - 5.5 and are summarized in Table 5.3. The difference of these inputs lies only on the time step n_{sp} because for a given ionic species, the more determinants are employed (e.g. as imposed by the various choice of frozen space) the denser timestep is required to yield a stable propagation.

Table 5.2: The number of determinants, ground state energies, and orbital energies of In, In^+, and In^{2+} obtained using various methods as mentioned in the text. Energy values inside parentheses indicate a relative value $\Delta E = E - E_{\mathrm{MCHF}}$, where E is its absolute value and E_{MCHF} is the corresponding MCHF energy for that ionic species. All energies are in Hartree.

Ion	In				In^+				In^{2+}	
Method	dn. $3d$	dn. $4s$	dn. $4p$	$4d$	dn. $3d$	dn. $4s$	dn. $4p$	$4d$	dn. $3d$	dn. $4s$
No. of dets	4012	2516	504	8	13696	7842	1110	6	32604	16876
GS energy	−5740.202963	(0.000048)	(0.000313)	(0.011969)	−5740.027691	(0.000133)	(0.000839)	(0.016909)	−5739.448916	(0.001288)
Orbital energies										
$1s$	−997.805104	(−0.000025)	(−0.000165)	(0.006480)	−998.076284	(−0.000052)	(−0.000268)	(0.007731)	−998.451820	(−0.000049)
$2s$	−149.394540	(−0.000024)	(−0.000159)	(0.000823)	−149.665056	(−0.000051)	(−0.000254)	(0.002364)	−847.274051	(−26.191516)
$2p_{-1}$	−139.170598	(−0.000024)	(−0.000161)	(0.000195)	−139.440772	(−0.000052)	(−0.000262)	(0.001676)	−847.274051	(−26.191516)
$2p_0$	−139.170093	(−0.000024)	(−0.000163)	(0.000145)	−139.440772	(−0.000052)	(−0.000262)	(0.001676)	−847.274051	(−26.191516)
$2p_{+1}$	−139.170598	(−0.000024)	(−0.000161)	(0.000195)	−139.440772	(−0.000052)	(−0.000262)	(0.001676)	−150.037099	(0.000792)
$3s$	−29.623246	(−0.000025)	(−0.000164)	(0.000252)	−29.893489	(−0.000052)	(−0.000268)	(0.001701)	−42.479205	(1.240702)
$3p_{-1}$	−25.373645	(−0.000025)	(−0.000160)	(0.000188)	−25.642630	(−0.000054)	(−0.000255)	(0.001567)	−42.479205	(1.240702)
$3p_0$	−25.371300	(−0.000024)	(−0.000172)	(−0.000007)	−25.642630	(−0.000054)	(−0.000255)	(0.001567)	−42.479205	(1.240702)
$3p_{+1}$	−25.373645	(−0.000025)	(−0.000160)	(0.000188)	−25.642630	(−0.000054)	(−0.000255)	(0.001567)	−30.263559	(−0.000023)
$3d_{-2}$	−17.589364	(−0.000025)	(−0.000165)	(0.000086)	−17.858000	(−0.000054)	(−0.000279)	(0.001431)	−18.230511	(0.000053)
$3d_{-1}$	−17.587386	(−0.000025)	(−0.000169)	(0.000047)	−17.858000	(−0.000054)	(−0.000279)	(0.001431)	−18.230511	(0.000053)
$3d_0$	−17.586702	(−0.000025)	(−0.000172)	(0.000039)	−17.858000	(−0.000054)	(−0.000279)	(0.001431)	−18.230511	(0.000053)
$3d_{+1}$	−17.587386	(−0.000025)	(−0.000169)	(0.000047)	−17.858000	(−0.000054)	(−0.000279)	(0.001431)	−18.230511	(0.000053)
$3d_{+2}$	−17.589364	(−0.000025)	(−0.000165)	(0.000086)	−17.858000	(−0.000054)	(−0.000279)	(0.001431)	−18.230511	(0.000053)
$4s$	−4.974774	(−0.000012)	(−0.000190)	(−0.000328)	−5.244761	(−0.000009)	(−0.000321)	(0.000677)	−5.637272	(0.023957)
$4p_{-1}$	−3.512587	(−0.000281)	(−0.003181)	(0.003480)	−3.781825	(−0.000822)	(−0.008148)	(0.006792)	−5.637272	(0.062630)
$4p_0$	−3.501267	(−0.000034)	(−0.000197)	(−0.000659)	−3.781825	(−0.000822)	(−0.008148)	(0.006792)	−5.637272	(0.062630)
$4p_{+1}$	−3.512587	(−0.000281)	(−0.003181)	(0.003480)	−3.781825	(−0.000822)	(−0.008148)	(0.006792)	−5.613296	(0.038654)
$4d_{-2}$	−1.066177	(−0.000024)	(−0.000191)	(−0.000423)	−1.330286	(−0.000052)	(−0.000354)	(0.000219)	−1.700696	(−0.000007)
$4d_{-1}$	−1.058547	(−0.000030)	(−0.000211)	(−0.000733)	−1.330286	(−0.000052)	(−0.000354)	(0.000219)	−1.700696	(−0.000007)
$4d_0$	−1.056137	(−0.000029)	(−0.000211)	(−0.000900)	−1.330286	(−0.000052)	(−0.000354)	(0.000219)	−1.700696	(−0.000007)
$4d_{+1}$	−1.058547	(−0.000030)	(−0.000211)	(−0.000733)	−1.330286	(−0.000052)	(−0.000354)	(0.000219)	−1.700696	(−0.000007)
$4d_{+2}$	−1.066177	(−0.000024)	(−0.000191)	(−0.000423)	−1.330286	(−0.000052)	(−0.000354)	(0.000219)	−1.700696	(−0.000007)

continued

Ion	In				In^+				In^{2+}	
Method	dn. $3d$	dn. $4s$	dn. $4p$	$4d$	dn. $3d$	dn. $4s$	dn. $4p$	$4d$	dn. $3d$	dn. $4s$
$5p_{-1}$	−0.705640	(0.001430)	(0.013333)	(0.083073)	−1.018057	(0.003842)	(0.031835)	(0.148599)	434.231743	(23.131634)
$5p_0$	−0.395051	(−0.000005)	(−0.000087)	(0.001410)	−1.018057	(0.003842)	(0.031835)	(0.148599)	434.231743	(23.131634)
$5p_{+1}$	−0.705640	(0.001430)	(0.013333)	(0.083073)	−1.018057	(0.003842)	(0.031835)	(0.148599)	434.231743	(23.131634)
$5s$	−0.196167	(0.000016)	(0.000034)	(0.000716)	−0.641481	(−0.000015)	(−0.000231)	(0.003016)	−0.942923	(0.000053)

Input 5.1	
L_{max}	43
p. shape	$\sin^2$
λ_0	795
I_0	2×10^{14}
φ_{CEP}	0°
p. length	4-cycle
n_{sp}	30000
Grid	Table 5.4 + 5.6
Absorb	irECS
r_{abs}	47.0
θ	15°

Input 5.2	
L_{max}	43
p. shape	$\sin^2$
λ_0	795
I_0	2×10^{14}
φ_{CEP}	0°
p. length	4-cycle
n_{sp}	45000
Grid	Table 5.4 + 5.6
Absorb	irECS
r_{abs}	47.0
θ	15°

Input 5.3	
L_{max}	43
p. shape	$\sin^2$
λ_0	795
I_0	2×10^{14}
φ_{CEP}	0°
p. length	4-cycle
n_{sp}	50000
Grid	Table 5.4 + 5.6
Absorb	irECS
r_{abs}	47.0
θ	15°

Input 5.4	
L_{max}	43
p. shape	$\sin^2$
λ_0	795
I_0	2×10^{14}
φ_{CEP}	0°
p. length	4-cycle
n_{sp}	60000
Grid	Table 5.4 + 5.6
Absorb	irECS
r_{abs}	47.0
θ	15°

Input 5.5	
L_{max}	43
p. shape	$\sin^2$
λ_0	795
I_0	2×10^{14}
φ_{CEP}	0°
p. length	4-cycle
n_{sp}	30000
Grid	Table 5.5 + 5.6
Absorb	irECS
r_{abs}	47.0
θ	15°

Table 5.3: .

Orb. subspace		is used with
Fig. 5.2(a)	fz. 4*d*	Input 5.5
	fz. 4*p*	Input 5.1
	fz. 4*s*	Input 5.3
	fz. 3*d*	Input 5.4
Fig. 5.2(b)	fz. 4*d*	Input 5.5
	fz. 4*p*	Input 5.2
	fz. 4*s*	Input 5.3
	fz. 3*d*	Input 5.4
Fig. 5.2(c)	fz. 4*s*	Input 5.3
	fz. 3*d*	Input 5.4

5.1.2 HH Spectra from Indium Plasma

Experimental observations of HHG using indium plasma source show that the enhancement occurs at around 20 eV (see Fig. 1.4(a) and Ref. [35]). With the help of TDCASSCF, we try to reproduce this observation from our simulations. Employing orbital subspace decompositions shown in Fig. 5.2 of the type fz. 3*d* and other simulation parameters in Input 5.4 for In, In^+, and In^{2+}, we obtain HH spectra as shown in Fig. 5.3 where a prominent peak is clearly apparent at 23.3 eV in the spectra from neutral and cation of indium. No peak at this energy observed from the HH spectrum of the dication.

As expected from the relative strength between the laser intensity for these simulations (2×10^{14} W/cm^2) and barrier suppression intensities for each ions (see Table 5.1), the charge state which dictates cutoff position in Fig. 5.3 is the cation. Nevertheless, HH signal extension even beyond the dication cutoff is still noticeable, this behavior will be explained later in Section 5.1.4.

The excitation spectra of In, In^+, and In^{2+} are depicted in Fig. 5.4. The neutral (purple) is seen not to have a transition peak with an appreciable strength around the enhanced peak 23.3 eV in its HHG spectrum. Whereas the dication has a prominent peak at 25.7 eV but none at 23.3 eV. This tells us that the enhanced peak at 23.3 eV in In and In^+ HH spectra (Fig. 5.3(a) and (b)) for a laser intensity of 2×10^{14} W/cm^2 is solely contributed by In^+.

In order to determine the lower orbitals responsible for the resonant emission at 23.3 eV, the same analysis as in Chapter 4 employing different frozen spaces is carried out and the results are summarized in Fig. 5.5. While in Fig. 5.5(c), there is no meaningful observation due to the absence of enhancement, in Fig. 5.5(a) and (b) one can clearly observe that the 23.3 eV peak dynamically changes as the frozen space is varied. Starting from the case of frozen 3*d* (solid dark green), both HH spectra from In and In^+ show a single peak at 23.3 eV. As 4*s* becomes frozen (dashed cyan), a second peak appears at 25.8 eV in In HH spectrum (Fig. 5.5(a) fz. 4*s*) whereas

Table 5.4

Interval	no. of FEs	n_{GP} per FE
0.0 – 1.0	1	25
1.0 – 2.0	1	25
2.0 – 4.0	1	25
4.0 – 7.0	1	25
7.0 – 11.0	1	25
11.0 – 43.0	8	25

Table 5.5

Interval	no. of FEs	n_{GP} per FE
0.0 – 0.5	1	25
0.5 – 1.0	1	25
1.0 – 2.0	1	25
2.0 – 4.0	1	25
4.0 – 7.0	1	25
7.0 – 11.0	1	25
11.0 – 43.0	8	25

Table 5.6

Interval	no. of FEs	n_{GP} per FE
GS grid Table 5.4 or Table 5.5		
43.0 – 47.0	1	25
47.0 – 55.0	2	25
55.0 – 59.0	1	25

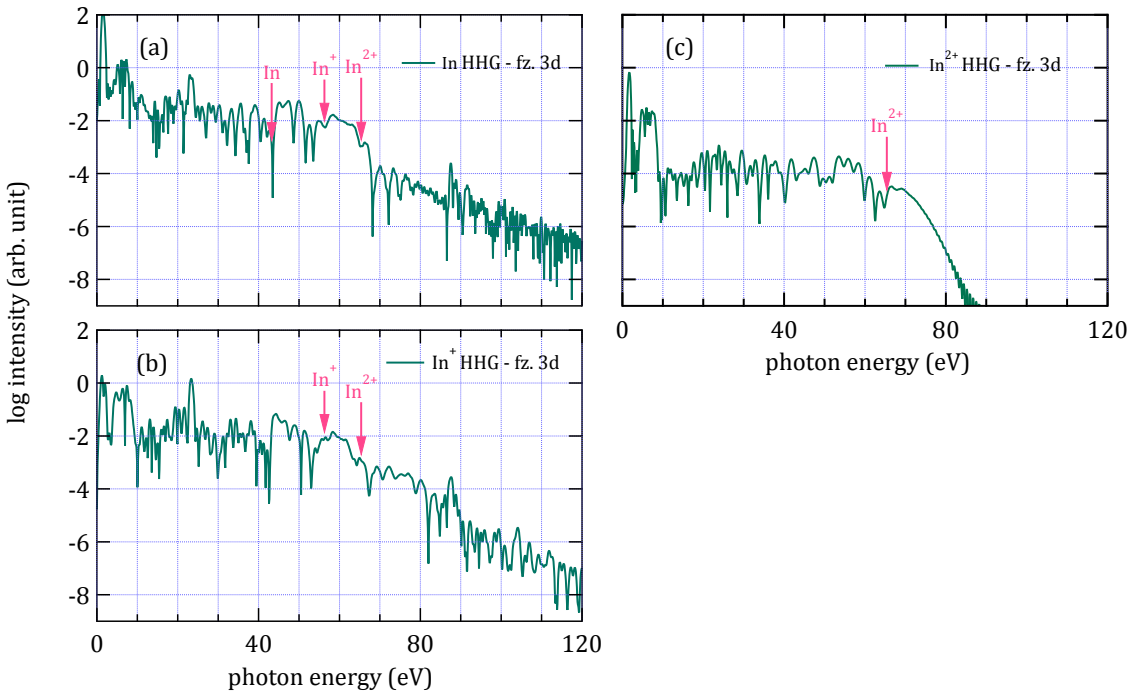

Figure 5.3: The HH spectra from (a) In, (b) In^+, and (c) In^{2+} using fz. 3*d* orbital subspace decomposition (see Fig. 5.2). The arrows mark cutoff position of the indicated ion.

the spectrum from In^+ does not exhibit an appreciable change. The second peak at 25.8 eV is still present in In HH spectrum when 4*p* are frozen (solid yellow). Finally, when 4*d* are frozen (solid red) the 23.3 eV peak disappears from In and In^+ spectra, the 25.8 eV peak is also absent from the former. This leads to the conclusion that the lower orbitals responsible for the enhancement of 23.3 eV harmonic peak are 4*d* orbitals. There is no fz. 4*p* spectrum for In^{2+} because the calculation resulted in an early emergence of big oscillations in the acceleration. Fz. 4*d* spectrum for this ion is not calculated either because no apparent enhancement is seen.

As before, we will also look at the time-frequency spectrograms of the HH spectra, this is presented in Fig. 5.6 where the upper row is for In while lower row for In^+, and the left column for fz. 3*d* while the right one for fz. 4*d* case. Some signal at around 23.3 eV is seen to appear in

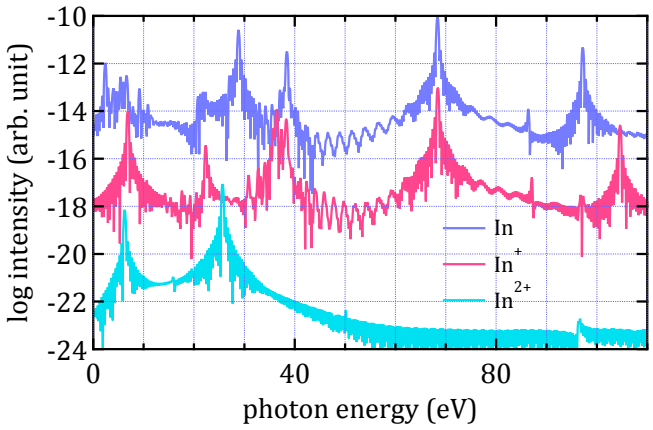

Figure 5.4: Excitation spectra of In, In^+, and In^{2+} obtained using fz. 3*d* orbital subspace decomposition (see Fig. 5.2).

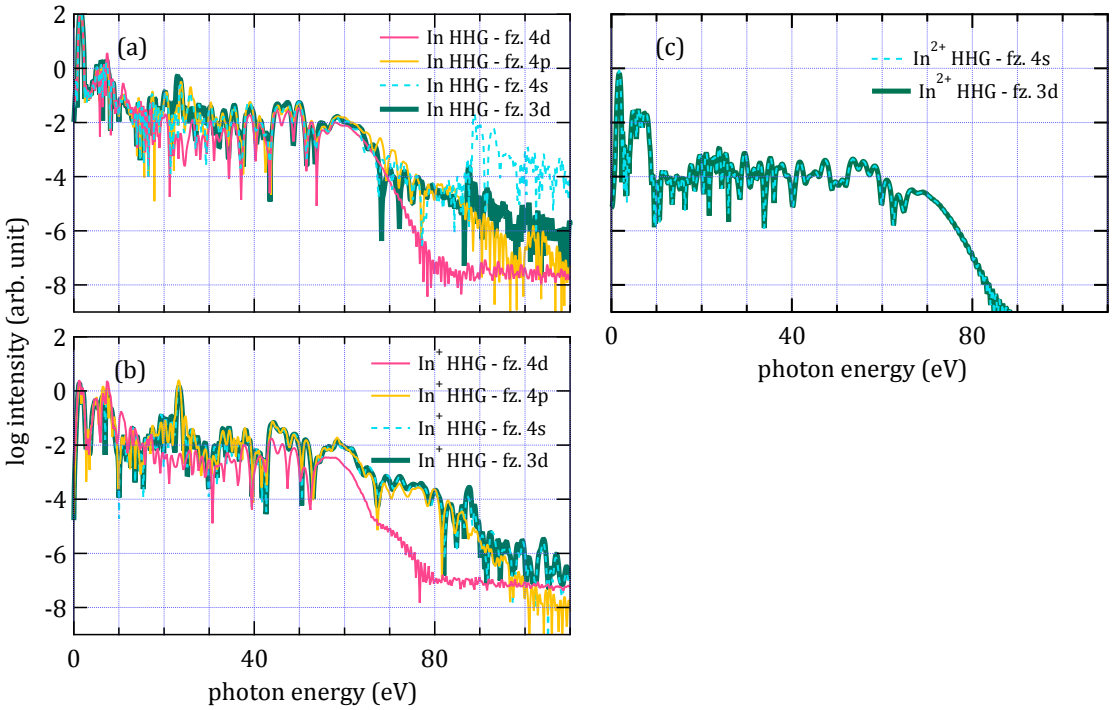

Figure 5.5: The spectra resulting from varying the frozen space (as indicated by the dashed lines in orbital diagrams in Fig. 5.2) in (a) In, (b) In^+, and (c) In^{2+}.

In spectrogram already within 3.5 – 5.0 fs, this is earlier than in In^+ which has the 23.3 eV peak appearing at about 4.8 fs. The bigger fraction of the 23.3 enhanced peak is also seen to be emitted when the laser starts to diminish. At the earlier moments, this emission is seen to be unsteady, for instance in Fig. 5.6(a), the 23.3 enhanced signal between 3.5 – 5.0 fs (one can tell that this signal contributes to the enhancement by comparing with Fig. 5.6(c) within the same interval) is reduced in intensity when the next bunch of returning electrons arrive, i.e. around 5.3 fs. The intensity of this peak rises again at around 7.6 fs when the long trajectory part of a returning bunch arrives. A similar behavior is also observed from Fig. 5.6(b) where an 23.3 eV enhancement signal is seen to build up around 6.3 – 6.8 but then diminishes and rises again at around 7.6 fs. Beyond this point where three-step process is less probable, the enhancement signal is more or less steady. This implies that the 23.3 eV resonant emission in In^+ triggered by a given returning electron bunch is out of phase with that from the next returning bunch.

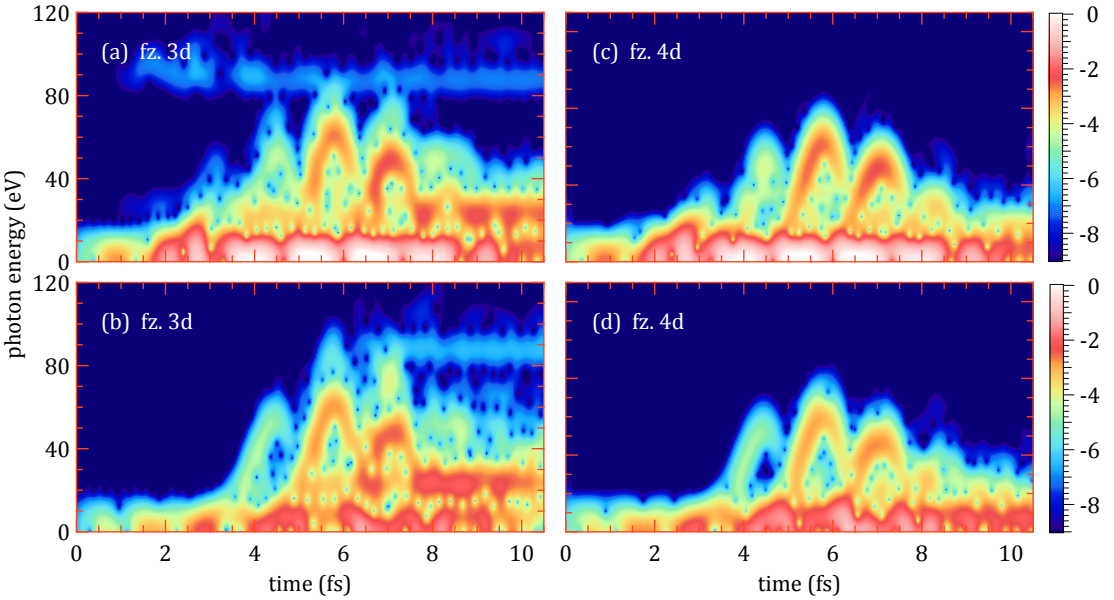

Figure 5.6: The time-frequency spectrograms obtained for In in upper row and for In^+ in lower row. The left column is obtained using fz. $3d$ and the right one using fz. $4d$ orbital decompositions.

5.1.3 Transition Analysis of High Harmonic Spectra

Decomposition of high-harmonic spectrum into orbital-orbital transitions makes up the heart of analyses presented in this disertation as it allows us to identify the dominating transitions to the HH emission. Therefore, as in Chapter 4, we also perform transition analysis on indium plasma HHG. The spectra of all possible orbital-orbital transitions out of orbital subspace decomposition fz. $3d$ in Fig. 5.2 are summarized in the left and right panels of Fig. 5.7 for In (using Input 5.4) and In^+(using Input 5.4), respectively.

It is evident that the spectra of $4d - 5p$ transition components in Fig. 5.7 exhibit a pronounced peak at 23.3 eV. This is an obvious sign that $4d - 5p$ transitions are the responsible ones which are in resonant with the 23.3 eV harmonic of the laser. Another transition in neutral In, namely $4s - 5p$, also exhibits a pronounced peak at the enhanced energy but this is a manifestation of the nondefinite orbitals angular momentum resulted from ground state calculation of neutral In (as mentioned in Section 5.1.1) making a portion of $4d - 5p$ transitions mixed in this transition. To confirm that $4d - 5p$ is really the responsible transition for the enhanced 23.3 eV harmonic, the components of this transition, $4d_m \leftrightarrow 5p_m$ with $m = 0, \pm 1$ are superposed and the result is shown in Fig. 5.8. The intensity at 23.3 eV of the total $4d - 5p$ transition (thick dark green) is seen to be stronger than that of the individual components, indicating that these components do interfere constructively at this energy, identical to the enhanced 50 eV peak in Mn plasma.

As in the case of Mn plasma, none of the existing theoretical studies on resonant HHG from indum plasma succeeded to verify the prevailing view that the resonance be associated to $4d - 5p$ transitions at the *ab initio* level. The current work therefore provides a complementary insight on the resonant HHG in indium plasma.

5.1.4 Non-Ionic Cutoff Extension - Multichannel Effect

One might have noticed the unusually long cutoff extension in the HH spectra of In (Fig. 5.3(a)) and In^+ (Fig. 5.3(b)). It is tempting to conclude that this extended signals come from In^{2+}, but we would to convince the reader that this is very unlikely for two reasons. First, looking at In^{2+} HH spectrum in Fig. 5.3(c), its cutoff region does not extend as far as the cutoff regions in Fig. 5.3(a) and (b) do. Second, this cutoff extension disappears when all orbitals below and including $4d$ are frozen (see Fig. 5.5) whereas freezing these orbitals should not prevent In^{2+} to be produced because its valence electron is in $5s$ orbital.

In order to determine the reason of this extension, the spectra of various $\beta(\bar{\mu}, t)$ where $\bar{\mu}$ comprises active orbitals in fz. $3d$ are plotted in Fig. 5.9(a)-(d). The vertical dashed lines mark the

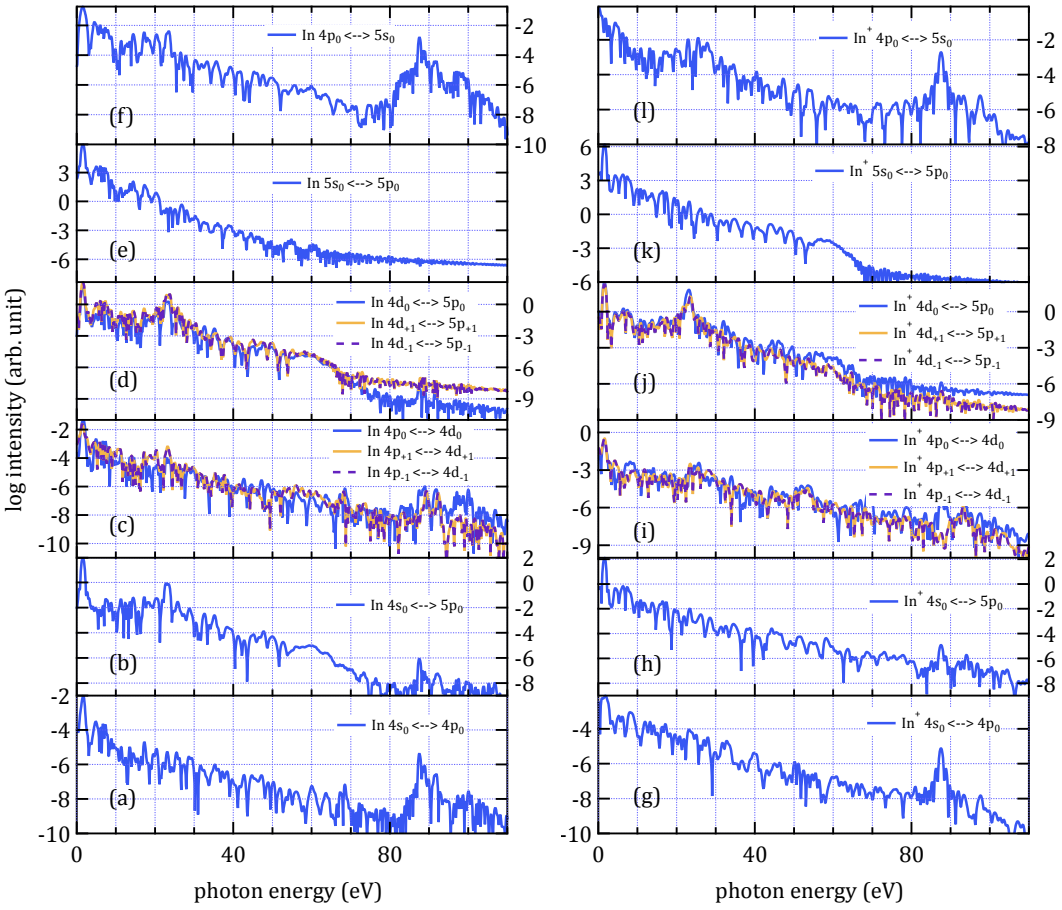

Figure 5.7: The spectra of all transitions possible with fz. $3d$ orbital subspace decomposition in In (left panels) and in In^+ (right panels).

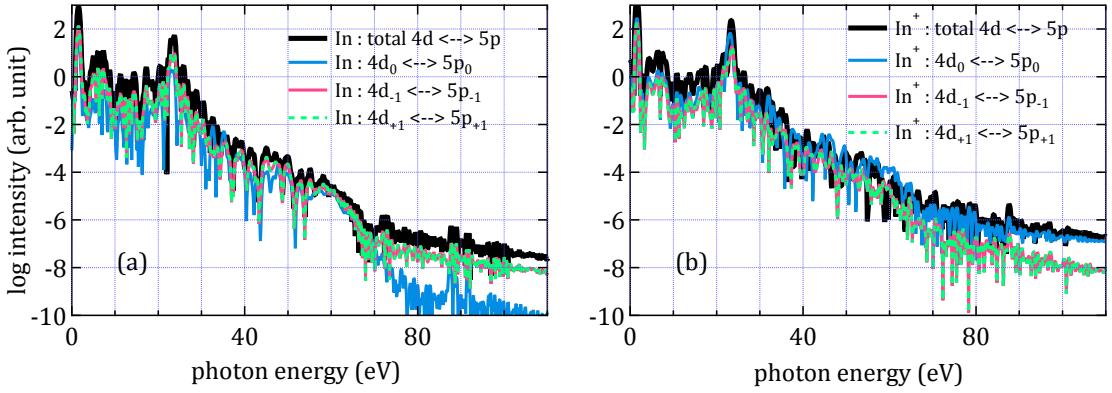

Figure 5.8: Spectra of $4d - 5p$ transitions and their coherent sum in (a) In and (b) In^+.

cutoff positions of several relevant ions of indium. In addition, cutoffs due to three-step process starting from $4d$ and $4p$ (which will be referred to as orbital cutoff) and due to *non-sequential double recombination* (NSDR) [111] are also shown. Orbital cutoffs are calculated as

$$E_c = \epsilon_\mu + 3.17U_p$$

with ϵ_μ is the binding energy of orbital μ given under dn. $3d$ columns of the corresponding ion in Table 5.2, while NSDR cutoff is calculated as

$$E_c = \mathrm{Ip}(\mathrm{In}^+) + \mathrm{Ip}(\mathrm{In}^{2+}) + 5.55U_p$$

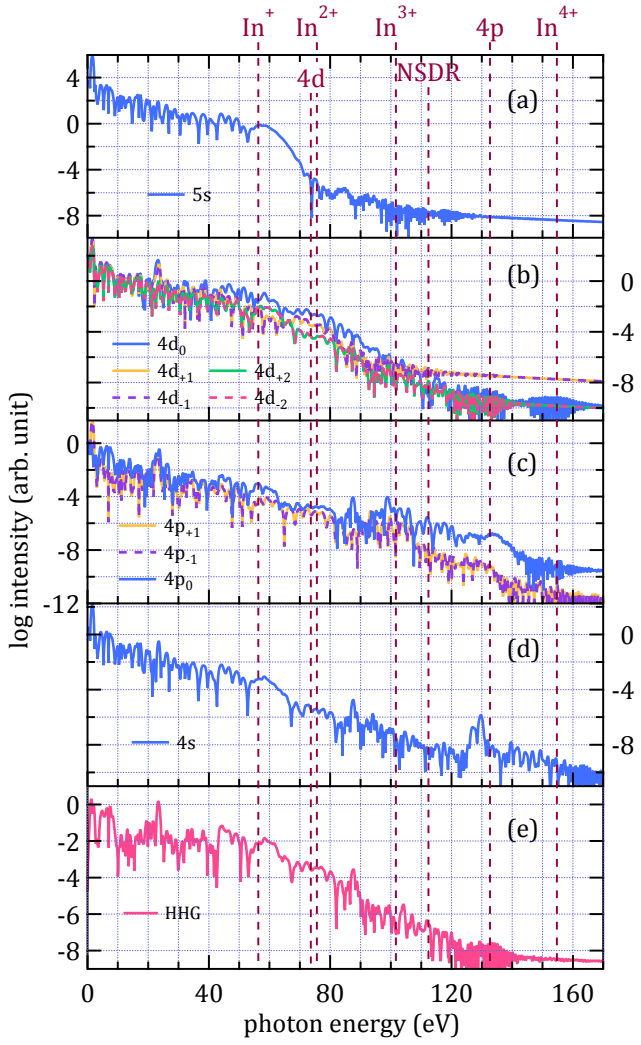

Figure 5.9: (a)-(d) The spectra of $\beta(\mu, t)$ where μ is the indicated orbital. (e) HH spectrum.

[111] with U_p = 11.8 eV for laser parameters used in this simulation (Input 5.4). By comparing the intensities of harmonic around 74 eV in these $\beta(\mu, t)$ spectra, one can see that the cutoff structure at this energy in HH spectrum (Fig. 5.9(e)) is mainly due to three-step process proceeding through $4d$ channel, i.e. an electron is tunnel-ionized from and returned to $4d$ orbitals. Whereas the final cutoff structure in HH spectrum at around 132 eV is seen to be coming from $4p_0$ channel. Other competing cutoff extension mechanisms such as those due to In^{3+} and In^{4+} are seen to be rather unimportant if not unimportant at all. For In^{3+} cutoff, since the valence orbitals of this species is $4d$, should its contribution be significant then it should be reflected in the cutoff of $4d$ channel (panel (b)) being close to In^{3+} cutoff (refer to Section 4.3.2 for the discussion of this sort of analysis). For In^{4+}, its cutoff is just out of the region of interest. Unfortunately, it is difficult to say anything about the extent to which NSDR is important from solely cutoff analysis. Nevertheless, from the fact that NSDR is a second order process in the number of returning electrons (the emitted energy is the sum of those of the individually returning electrons) while multichannel effects are essentially still a first order process, NSDR harmonic extension is possibly not as noticeable as the extension from other channel-HHG. In the theoretical work of Ref. [111] where NSDR was first reported, the analysis employed 2-electron atom, if the two electrons occupy the same spatial orbital then there is only one channel in the system and any possible cutoff extension must be from higher-order emission, in this case NSDR.

5.2 Resonant High-Harmonic Generation from Chromium and Its Cations

Chromium is similar to manganese presented in Chapter 4 with regards to the number of electrons ($N = 24$). Experimental HH spectra generated from chromium plasma exhibit enhancement at ~ 45 eV (see Table 1.1) [37, 39].

5.2.1 Simulation Conditions

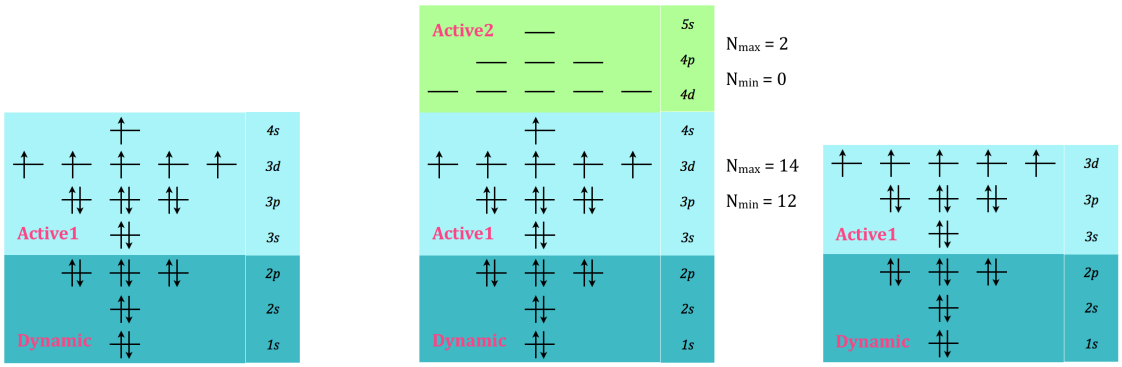

Figure 5.10: Orbital subspace decompositions used to calculate the ground states of Cr and Cr^+ in the present chapter.

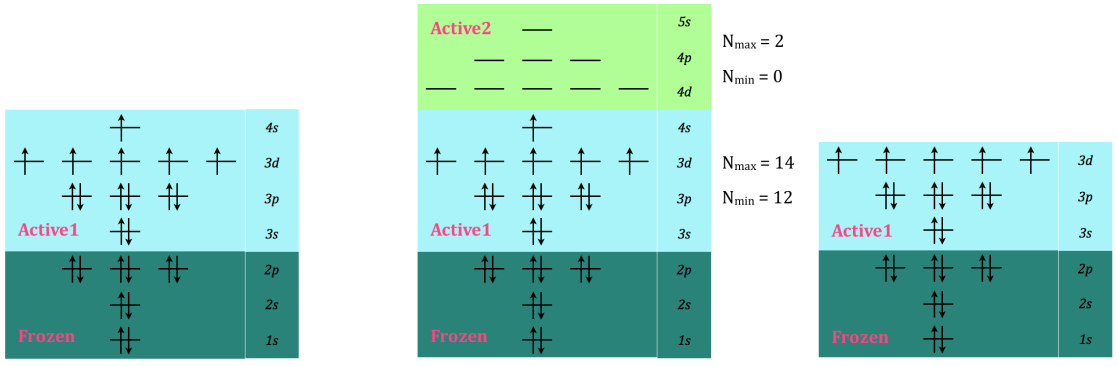

Figure 5.11: Orbital subspace decompositions used to perform HH simulations on Cr and Cr^+ in the present chapter.

The ground state electronic configuration, ionization potential, and barrier suppression intensity of Cr and Cr^+ are provided in Table 5.7. The ground state For ground state calculations presented in the current section, orbital subspace decompositions in Fig. 5.10(a) (TD-CASSCF) and (b) (TD-ORMAS) are employed for Cr and Fig. 5.10(c) (TD-CASSCF) for Cr^+. The corresponding HH simulations are performed using Fig. 5.11 subspace decompositions. As for the case of Mn in Section 4, any TD-ORMAS attempts for Cr^+, which is isoelectronic to Mn^{2+}, always fail in producing physically acceptable wavefunction. In this section, radial grids given Table 5.8 and 5.9 are used for ground state and for HH calculations, respectively. The laser parameters as well as the other simulation parameters for various HH simulations are given in Input 5.6 - 5.7.

5.2.2 HHG Spectra

The HH spectra from neutral Cr and Cr^+ are presented in Fig. 5.12, exhibiting yet another evidence of the capability of TD-CASSCF and TD-ORMAS to reproduce resonant enhancement

Table 5.7: Experimental ionization potential I_p, barrier-suppression intensity I_{BS}, and the ground-state configuration of Cr and Cr^+.

	Cr	Cr^+
I_p[a]	6.77	16.49
I_{BS}[b]	8.40×10^{12}	2.96×10^{14}
GS[c]	$[Ar]4s3d^5(^7S_3)$	$[Ar]3d^5(^6S_{5/2})$

[a] Experimental ionization potential in eV [109, p. 1664].
[b] Barrier-suppression intensity in W/cm^2.
[c] Ground state configuration [109, p. 1664].

Input 5.6	
L_{max}	44
p. shape	$\sin^2$
λ_0	1330
I_0	1×10^{14}
φ_{CEP}	0°
p. length	4-cycle
n_{sp}	20000
Grid	Table 5.9
Absorb	irECS
r_{abs}	122.0
θ	15°

Input 5.7	
L_{max}	44
p. shape	$\sin^2$
λ_0	1330
I_0	1×10^{14}
φ_{CEP}	0°
p. length	4-cycle
n_{sp}	17000
Grid	Table 5.9
Absorb	irECS
r_{abs}	122.0
θ	15°

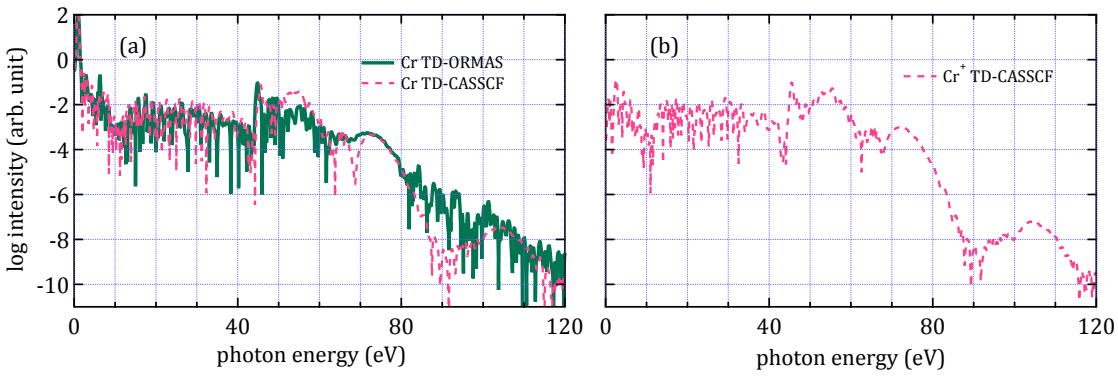

Figure 5.12: HH spectra from (a) Cr using Input 5.6 and (b) from Cr^+ using Input 5.7. In (a), Fig. 5.11(a) orbital decomposition is used for TD-CASSCF spectrum and Fig. 5.11(b) for TD-ORMAS spectrum. In (b), Fig. 5.11(c) is employed.

from transition metals. The enhancement occurs for the harmonic at 44.8 eV in Cr TD-ORMAS spectrum (solid green) and at 45.5 eV in Cr and Cr^+ TD-CASSCF (dashed red) spectra, which may be compared with experimental data in Fig. 1.5(a). The excitation spectra shown in Fig, 5.13 also confirms the presence of a giant transition amplitude at the resonant energy. In TD-CASSCF spectra (red dashed), there is an apparent energy interval 48 – 60 eV where the maximum harmonic intensity is almost as high as the resonant harmonic. This feature however is probably a numerical artifact linked to the insufficient number of orbitals (14 and 15 for these TD-CASSCF simulations) as it is significantly suppressed in Cr TD-ORMAS spectrum (solid dark green).

5.2.3 Transition Analysis of High-Harmonic Spectra

The spectra of $3p-3d$ transitions from Cr and Cr^+ are depicted in Fig. 5.14(a) and (b), respectively. As in the case of Mn in Chapter 4, it is $3p-3d$ transitions which are responsible for the enhancement

Table 5.8

Interval	no. of FEs	n_{GP} per FE
0.0 – 1.0	1	25
1.0 – 3.0	1	25
3.0 – 6.0	1	25
6.0 – 10.0	1	25
10.0 – 42.0	8	25

Table 5.9

Interval	no. of FEs	n_{GP} per FE
GS grid Table 5.8		
42.0 – 122.0	20	25
122.0 – 130.0	2	25
130.0 – 134.0	1	25

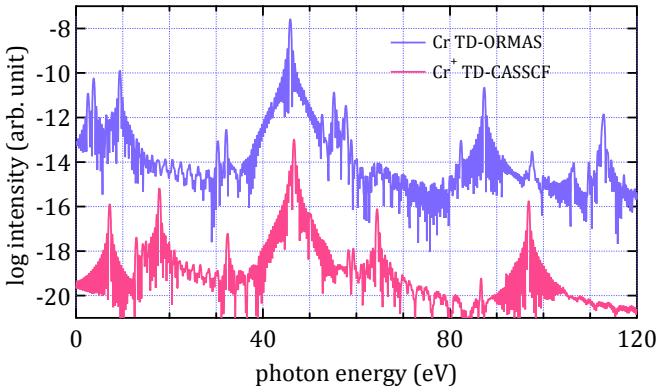

Figure 5.13: Excitation spectra of Cr and Cr^+. Cr spectrum uses Fig. 5.11(b) while Cr^+ spectrum uses Fig. 5.11(c)

at 44.8 eV in Cr and Cr^+ spectra. The coherent sum of these transitions shown as the black spectrum is also seen to have a stronger peak around the enhanced harmonic, confirming the constructive interference origin of resonant enhancement in HHG from plasma.

5.3 Summary

Complementing the results and analyses presented in Chapter 4 for one type of plasma, namely manganese plasma, this Chapter provides evidence of the applicability of TD-CASSCF to reproduce resonant enhancement for considerably larger systems, in particular indium ions whose number of electrons is twice as large as that in Mn. In these ions, the enhancement is found at 23.3 eV and, for the intensity of 2×10^{14} W/cm^2, is contributed mainly by In^+. The transitions coupled in resonance with the harmonics of the laser are the $4d - 5p$ transitions. New behaviors have also been identified from the analyses of indium HH spectra, this includes (1) the destructive interference between the resonantly enhanced emissions at 23.3 eV between those emitted during a given

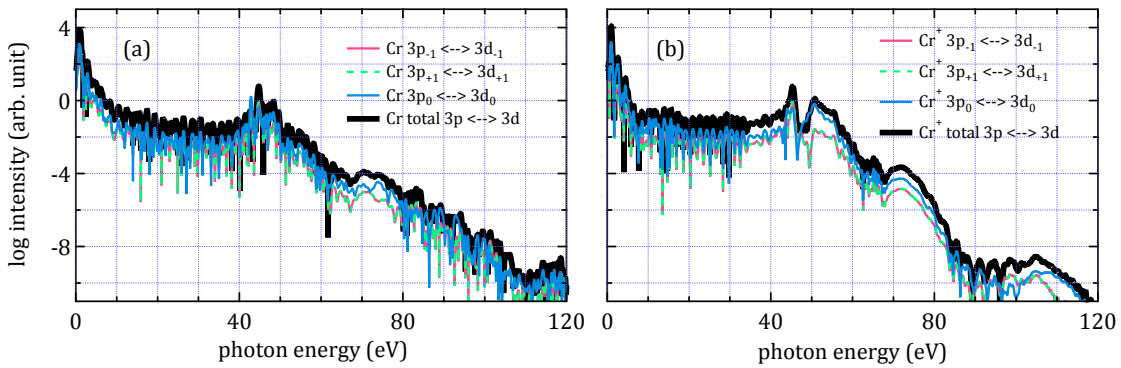

Figure 5.14: $3p - 3d$ transition spectra in (a) Cr (using Fig. 5.11(b) orbital decomposition and Input 5.6) and in (b) Cr^+ (using Fig. 5.11(c) orbital decomposition and Input 5.7).

half-cycle with those from the next half-cycle and (2) the cutoff extension due to three-step process starting from and ending in non-valence orbitals. In the last part of this chapter, several results from chromium ions are also presented. The enhancement occurs around 45 eV and the transitions responsible for the enhancement are the $3p - 3d$ transitions. Overall, this chapter demonstrates the applicability of TD-CASSCF and TD-ORMAS to reproduce resonant enhancement in various types of metal plasmas and to perform insightful analyses able to guide us to the attainment of the research objectives.

Chapter 6

Concluding Remarks

The underlying physics behind resonant enhancement in HHG is addressed from the theoretical point of view in this dissertation. The mathematical tools employed for solving the appropriate Schrödinger equation and performing the subsequent analyses are the TD-MCSCF methods. TD-MCSCF is an *ab initio* method based on variational principle that is used to handle time-dependent quantum phenomena. Using the generalization of TD-MCSCF, namely TD-CASSCF [63, 64] and TD-ORMAS [65], we have successfully reproduced resonant enhancement in manganese plasma (Mn, Mn^+, and Mn^{2+}), indium plasma (In, In^+, and In^{2+}), and chromium plasma (Cr and Cr^+) at an energy close to their experimental value ($\sim$ 50 eV, $\sim$ 20 eV, and $\sim$ 45 eV respectively) and subsequently, identified the responsible mechanism of the enhancement. This result, to the best of our knowledge, represents a pioneering conclusive work within the subject of resonant HHG from transition metals. Before the present work, there have been already a number theoretical efforts addressing the same problem. The key difference between our take on the problem at hand and those existing works lies in the nature of the central assumptions imposed in their mathematical tools. As opposed to our mathematical framework where all electrons are allowed to take part in the dynamics explicitly, those previous studies mostly rely on single active electron approach where the effect of the rest of the electrons are expressed in terms of an effective core potential. Intended to complement the shortcomings of these pioneering studies, we perform a theoretical study by employing methods that allow all electrons to interact with the laser.

6.1 The Close Relation Between Orbital Dynamics and Resonant Enhancement

As our investigation reveals, resonant HHG can be thought of as an exception to ordinary HHG in terms of the sensitivity of HHG with the inner structure of an atom. In ordinary HHG, the essential states are the ground and continuum states of the unperturbed atom. The underlying reason is that due to the strong pull from laser field, the ionized electron immediately leaves its parent core and spends sometimes in continuum. Upon return, it goes back to the ground state by emitting HH photon. This process is, at most, weakly sensitive with respect to the structure of discrete levels in the atom. This is in fact, the reason why SFA [23, 45] is successful in describing HH process from rare gas atoms.

As demonstrated in Section 4.2.2 and Section 4.3.1, resonant HHG is an exception to this longstanding qualitative understanding of HHG. In particular, in Section 4.2.2 it is found that freezing $3p$ orbitals in Mn, Mn^+, and Mn^{2+} results in the disappearance of 51.5 eV enhancement. Furthermore, the biggest differences in the spectra are isolated around the resonant energy, outside this region there are only negligible difference. This is a clear evidence of the importance of inner core dynamics in resonant HHG. Further investigation in terms of orbital transitions allows us to decompose the contribution of each individual dipole-allowed transitions to the total HH spectrum, this is done in Section 4.3.1. From this study it is found that in Mn and Mn^+, the resonant radiation at 51.5 eV is contributed mainly by transitions which couple $3p$ with $3d$ orbitals. In particular, comparing Fig. 4.12(f) with 4.12(h) and Fig. 4.13(f) with 4.13(h), one can see that the 51.5 eV peak in the total $3p - 3d$ spectrum is about ten times stronger than the peak at the same

energy in the individual $3p_m - 3d_m$ spectrum with $m = 0, \pm 1$. This suggests that the enhancement is the result of a constructive intereference between $3p_m - 3d_m$ transitions that are allowed by dipole selection rules. Identical analysis performed on In and Cr plasmas reveals that the 23.3 eV enhancement in the former is due to $4d - 5p$ constructive interference while in the latter, the 45 eV enhancement comes from $3p - 3d$ dynamics, the same as Mn case but at a different energy.

6.2 How Does The Resonant State Get Populated?

As pointed out in the preceding section, resonant HHG is special because it requires a participation of another discrete state (that is, the resonant state), beside the ground one during laser interaction and this second state must be allowed to interact through dipole interaction with the ground state. Since in the beginning the atom starts from its ground state, a natural question that arises would be how the resonant excited state gets its population in the first place. Moreover, considering that single active electron approaches work just fine for the most part when there is no enhancement (i.e. ordinary HHG), it is easy to suspect that this resonant state plays a central role in resonant HHG. To answer this question, we refer to the time-frequency spectrogram of Mn and Mn^+ shown in Fig. 4.10. This two-dimensional function provides a map of the emission time of each photon energy in the spectrum. One observes that there is a horizontal streak of signal at about $\sim$ 50 eV in Fig. 4.10(a) and (b), this is obviously the resonantly enhanced peak. These signals appear only after the second bunch of returning electrons where they are seen to have kinetic energies such that it is sufficient to emit $\sim$ 50 eV radiations upon returning to the ground state. For some of these electrons however, when the moment to emit photons through the ordinary way, namely by recombining to its initial state, comes, they got "suspended" in an excited state that lies $\sim$ 50 eV above the ground state. Electrons captured by this state then subsequently relaxate to a lower orbital. To make a connection with the remark in Section 6.1, the upper orbitals at which the returning electron makes a temporary visit are $3d$ orbitals, while the lower orbitals to which it relaxates by emitting the resonant radiation are $3p$ orbitals. This $\sim$ 50 eV signal in the time-frequency spectrograms is also seen to not completely respect return kinetic energy curves. This supports the idea that the final mechanism leading to the emission of resonantly enhanced radiation is mainly an outcome of bound-bound dynamics rather than continuum-bound ones.

6.3 Signature of Resonant Enhancement in The Time-Dependent Orbital Populations

The evolution of orbital populations in Mn and Mn^+ during laser interaction is presented in Section 4.4. Taking the Fourier transform of the first derivative of these time-dependent populations, one obtains a function of frequency for each orbital and from these frequency domain functions, it is revealed that the corresponding time-domain population is modulated at the same frequencies as any transitions involving that orbital. For example, there are two transitions in neutral Mn involving $3p_0$ that have prominent peaks in their spectra - $3p_0 \leftrightarrow 4s_0$ at 61.6 eV (Fig. 4.12(e)) and $3p_0 \leftrightarrow 3d_0$ at 51.5 eV (Fig. 4.12(f)). While at the same time, the spectrum of $\partial_t n(3p_0, t)$ has peaks at 51.5 eV and 61.6 eV (Fig. 4.16(i)), the spectrum of $\partial_t n(4s_0, t)$ at 61.6 eV (Fig. 4.16(k)), and the spectrum of $\partial_t n(3d_0, t)$ at 51.5 eV (Fig. 4.16(j)), indicating that the population of these orbitals is modulated at the indicated frequency. The important remark of this orbital population study is that, as implied from Fig. 4.18, the populations of the two orbitals being coupled by a strong transition line exhibit an alternating population exchange - a peak in $n(3p_m, t)$ at a given moment implies a valley in $n(3d_m, t)$ at the same time - with a periodicity corresponding to the resonant energy. Moreover, judging from the absence of the peaks around 51.5 eV in the total spectra of virtual orbitals $\partial_t n_{\mathcal{V}}(t)$ (Fig. 4.16(l) and Fig. 4.17(l)), this alternating population exchange is apparently confined between $3p$ and $3d$ orbitals only. Hence, it may support the idea pointed out in Section 6.1 about the final mechanism of the resonant emission process which excludes continuum states.

6.4 Prospects of The Research

Resonant HHG offers a new platform of both basic and applied researches within the scope of strong-field phenomena. In the instance of an atom and its first few cations having giant transition lines which do not coincide with each other, resonant HHG can serve as a means of study to understand ionization dynamic during HHG. From application point of view, it is not too far-fetched to envisage resonant HHG to be one of prospective methods of choice to generate an intense quasi-monochromatic coherent XUV radiation. These fields of researches will definitely benefit from a mature theoretical understanding of the physics that underlies resonant HHG.

Appendix A

Commutator Identities Involving Creation and Annihilation Operators

In second quantization, the (anti)symmetry and orthogonality properties of many-particle wavefunction are delegated to the the anti-commutator properties of creation and annihilation operators. Here we list some commutator and anti-commutator identities involving creation and annihilation operators *for fermions* which are used in various derivations in this dissertation.

$$\left\{\hat{a}_m^\dagger, \hat{a}_n^\dagger\right\} = 0 \tag{A.1}$$

$$\{\hat{a}_m, \hat{a}_n\} = 0 \tag{A.2}$$

$$\left\{\hat{a}_m^\dagger, \hat{a}_n\right\} = \delta_{mn} \tag{A.3}$$

$$\left[\hat{a}_m^\dagger, \hat{a}_n^\dagger \hat{a}_p\right] = -\delta_{mp}\hat{a}_n^\dagger \tag{A.4}$$

$$\left[\hat{a}_m, \hat{a}_n^\dagger \hat{a}_p\right] = \delta_{mn}\hat{a}_p \tag{A.5}$$

$$\left[\hat{a}_m^\dagger \hat{a}_n, \hat{a}_p^\dagger \hat{a}_q\right] = \delta_{np}\hat{a}_m^\dagger \hat{a}_q - \delta_{mq}\hat{a}_p^\dagger \hat{a}_n \tag{A.6}$$

$$\begin{aligned}\left[\hat{a}_m^\dagger \hat{a}_n, \hat{a}_p^\dagger \hat{a}_q \hat{a}_r^\dagger \hat{a}_s\right] = {} & \delta_{np}\hat{a}_m^\dagger \hat{a}_q \hat{a}_r^\dagger \hat{a}_s - \delta_{mq}\hat{a}_p^\dagger \hat{a}_n \hat{a}_r^\dagger \hat{a}_s + \delta_{nr}\hat{a}_p^\dagger \hat{a}_q \hat{a}_m^\dagger \hat{a}_s - \ldots \\ & \delta_{ms}\hat{a}_p^\dagger \hat{a}_q \hat{a}_r^\dagger \hat{a}_n\end{aligned} \tag{A.7}$$

Eq. (A.1)-(A.3) serve as the base equations for deriving the rest of the identities since in these three identities are encoded the anti-symmetry of many-fermion wavefunction and the orthogonality of one-fermion functions constituting the wavefunction with the former being a natural principle whereas the latter being analysis dependent.

Appendix B

Elements of Density Matrices

B.1 One-Electron Reduced Density Matrix (1RDM)

It is fairly straightforward to determine the vanishing matrix elements of D^{μ}_{ν}. Since $D^{\mu}_{\nu} = \langle\Psi|\hat{E}^{\nu}_{\mu}|\Psi\rangle$, D^{μ}_{ν} will be zero if $\hat{E}^{\nu}_{\mu}|\Psi\rangle$ is orthogonal to $|\Psi\rangle$, that is , if the former lies outside $\hat{\Pi}$. This occurs when the orbital rotation involves orbitals from different orbital subspaces. Owing to the Hermitian property of density matrix, one has the obvious consequence $D^{\mu}_{\nu} = \left(D^{\nu}_{\mu}\right)^{*}$.

B.2 Two-Electron Reduced Density Matrix (2RDM)

Any given element of 2RDM effectively depends on four indices. With three orbital subspaces (core, active, and virtual), one has 81 possible groups of 2RDM elements classified based on the involvement of the three subspaces. Fortunately, this number can be significantly reduced to 16 by removing groups where at least one of the indices belong to virtual subspace. The reason is when we consider

$$P^{\nu\gamma}_{\mu\lambda} = \sum_{s}\sum_{s'}\langle\hat{a}_{\lambda s'}\hat{a}_{\mu s}\Psi|\hat{a}_{\gamma s'}\hat{a}_{\nu s}\Psi\rangle, \tag{B.1}$$

we can immediately see if at least one of the four indices belongs to virtual subspace, when it is the turn for that annihilation operator to act on whatever vector to the right, $P^{\nu\gamma}_{\mu\lambda}$ will equal zero.

The zero and non-zero elements of 2RDM when the four indices are among core and active subspaces are summarized in Table B.1. The following expression of 2RDM element is used in reference to the 6-th column,

$$\begin{aligned} P^{\nu\gamma}_{\mu\lambda} &= \langle\hat{E}^{\nu}_{\mu}\Psi|\hat{E}^{\lambda}_{\gamma}\Psi\rangle - \delta_{\lambda\nu}\langle\Psi|\hat{E}^{\mu}_{\gamma}\Psi\rangle \\ &= \langle\hat{E}^{\nu}_{\mu}\Psi|\hat{E}^{\lambda}_{\gamma}\Psi\rangle - \delta_{\lambda\nu}\langle\hat{E}^{\gamma}_{\mu}\Psi|\Psi\rangle \end{aligned} \tag{B.2}$$

where we have used the definition of $\hat{E}^{\mu\lambda}_{\nu\gamma}$ in Eq. (3.8). 2RDM possesses the following symmetries among its elements

$$P^{\nu\gamma}_{\mu\lambda} = \left(P^{\lambda\mu}_{\gamma\nu}\right)^{*} \tag{B.3}$$

$$P^{\nu\gamma}_{\mu\lambda} = P^{\gamma\nu}_{\lambda\mu} \tag{B.4}$$

which derive from the Hermitian property of density matrix and the antisymmetry of the wave-function, respectively.

Taking a closer look at Table B.1, we may see that the vector $\left|\hat{E}^{\mu}_{\nu}\Psi\right\rangle$ is always zero if ϕ_{μ} is a core orbital while ϕ_{ν} is not. This is obvious from the fact that core orbitals are already at their full occupation. The inner product $\left\langle\hat{E}^{\nu}_{\mu}\Psi\middle|\hat{E}^{\lambda}_{\gamma}\Psi\right\rangle$ vanishes if either of the following three conditions are satisfied,

1. ϕ_{ν} (ϕ_{λ}) is a core orbital while ϕ_{μ} (ϕ_{λ}) is active,

Table B.1: A list of 2RDM elements $P^{\nu\gamma}_{\mu\lambda}$ in cases where the four indices are among core and active orbitals. The first ten elements are the vanishing ones with the last column listing the vanishing quantities involved in Eq. (B.2), hence explaining why the corresponding element vanishes. The last six elements are those that generally do not vanish with the last column containing the final expression of the corresponding element.

No.	μ	λ	ν	γ	Vanishing quantities (1-10) or final expression (11-16)[†‡]
1)	t	i	j	k	$\langle\hat{E}^{\nu}_{\mu}\Psi\vert = 0, \langle\hat{E}^{\gamma}_{\mu}\Psi\vert = 0$
2)	k	i	j	t	$= 1)^*$
3)	i	t	j	k	$\langle\hat{E}^{\nu}_{\mu}\Psi\vert\hat{E}^{\lambda}_{\gamma}\Psi\rangle = 0, \delta_{\lambda\nu} = 0$
4)	i	j	t	k	$= 3)^*$
5)	i	t	u	v	$\langle\hat{E}^{\nu}_{\mu}\Psi\vert\hat{E}^{\lambda}_{\gamma}\Psi\rangle = 0, \vert\hat{E}^{\mu}_{\gamma}\Psi\rangle = 0$
6)	v	t	u	i	$= 5)^*$
7)	t	i	u	v	$\vert\hat{E}^{\lambda}_{\gamma}\Psi\rangle = 0, \delta_{\lambda\nu} = 0$
8)	t	u	i	v	$= 7)^*$
9)	i	j	t	u	$\vert\hat{E}^{\lambda}_{\gamma}\Psi\rangle = 0, \vert\hat{E}^{\mu}_{\gamma}\Psi\rangle = 0, \delta_{\lambda\nu} = 0$
10)	t	u	i	v	$= 9)^*$
11)	i	u	t	j	$= 12)$
12)	u	i	j	t	$-\delta_{ij}D^{t}_{u}$
13)	i	t	j	u	$2\delta_{ij}D^{u}_{t}$
14)	u	j	t	i	$= 13)^*$
15)	i	j	k	l	$4\delta_{ik}\delta_{jl} - 2\delta_{il}\delta_{jk}$
16)	t	u	v	w	P^{tu}_{vw}

[†] = n)* means identical to the complex conjugate of the element in the n-th line.

[‡] = n) means identical to the element in the n-th line.

2. either bra or ket is in $\hat{\Pi}$ and the other in $\hat{Q}$, e.g. the third entry,

3. $(\lambda, \gamma) \in$ active $\times$ active and $(\nu, \mu) \in$ active $\times$ core or *vice versa*, e.g. the fifth entry.

The reasons for the first and second points are clear. As for the third one, in the case of TD-CASSCF this is just a special case of the second point. In TD-ORMAS, however, the wavefunction being rotated between active orbitals in general lies across $\hat{\Pi}$ and $\hat{Q}$, instead of just $\hat{\Pi}$. In this instance, $\langle\hat{E}^{\nu}_{\mu}\Psi\vert\hat{E}^{\lambda}_{\gamma}\Psi\rangle$ still vanishes because the wavefunction being excited from core to active contains determinants that are necessarily different from those of the active-active rotated wavefunction. With this observation in mind, we can see that Table B.1 also applies if we replace the wavefunctions in bra and ket with two different determinants $|I\rangle$ and $|J\rangle$ living in $\hat{\Pi}$ space with a little modification in the notation. The nonzero elements are

$$(P_{IJ})^{jt}_{ui} = -\delta_{ij}\,(D_{IJ})^{t}_{u} \tag{B.5a}$$
$$(P_{IJ})^{tj}_{iu} = -\delta_{ij}\,(D_{IJ})^{t}_{u} \tag{B.5b}$$
$$(P_{IJ})^{ju}_{it} = 2\delta_{ij}\,(D_{IJ})^{u}_{t} \tag{B.5c}$$
$$(P_{IJ})^{ti}_{uj} = 2\delta_{ij}\,(D_{IJ})^{t}_{u} \tag{B.5d}$$
$$(P_{IJ})^{kl}_{ij} = \delta_{IJ}\left(4\delta_{ik}\delta_{jl} - 2\delta_{il}\delta_{jk}\right) \tag{B.5e}$$
$$(P_{IJ})^{tu}_{vw} \tag{B.5f}$$

where $(D_{IJ})^{\mu}_{\nu} = \langle I|\hat{E}^{\nu}_{\mu}|J\rangle$. The same argument also applies for 1RDM, namely if we replace the wavefunctions in $\langle\Psi|\hat{E}^{\mu}_{\nu}|\Psi\rangle$ with two different determinants $|I\rangle$ and $|J\rangle$ living in $\hat{\Pi}$ space, then the nonzero elements are

$$(D_{IJ})^{i}_{j} = 2\delta_{ij}\delta_{IJ} \tag{B.6a}$$
$$(D_{IJ})^{t}_{u}\,. \tag{B.6b}$$

Appendix C

Radial Functions of The Ground State Orbitals

Referring to Eq. (3.61) and (3.65), we may rewrite the former for an initial orbital in the form

$$\phi_\mu(\mathbf{r}, t = 0) = \sum_{l=0}^{l_{\max}} Y_{lm}(\theta, \varphi) \frac{U_l^\mu(r)}{r} \tag{C.1}$$

where the radial function $U_l^\mu(r)$ associated with the l-th spherical harmonic of orbital $\phi_\mu(\mathbf{r}, 0)$ is defined to be

$$U_l^\mu(r) = \sum_{n=1}^{n_{\max}} c_{nl}^\mu(0) p_n(r). \tag{C.2}$$

In this chapter, the plots of $U_l^\mu(r)$ for $l = 0, 1, 2$ for each of the 24 orbitals in Mn and Mn^+ obtained from ground state calculations using orbital subspace decompositions in Fig. 4.1(d) and (e), respectively, are presented. These plots are, for instance, useful in explaining the population depletion experienced by various initial orbitals which are presented in Fig. 4.16 and 4.17.

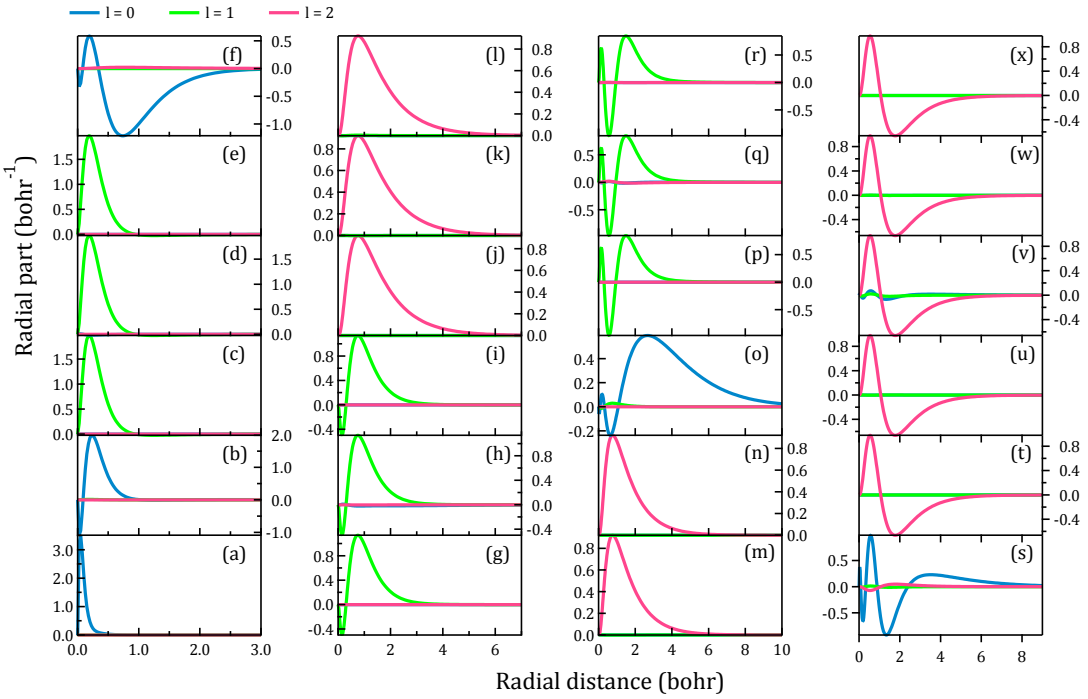

Figure C.1: Radial functions $U_l^\mu(r)$ of each neutral Mn ground state orbitals obtained using orbital subspace decomposition in Fig. 4.1(d) for μ = (a) $1s$, (b) $2s$, (c) $2p_{-1}$, (d) $2p_0$, (e) $2p_{+1}$, (f) $3s$, (g) $3p_{-1}$, (h) $3p_0$, (i) $3p_{+1}$, (j) $3d_{-2}$, (k) $3d_{-1}$, (l) $3d_0$, (m) $3d_{+1}$, (n) $3d_{+2}$, (o) $4s$, (p) $4p_{-1}$, (q) $4p_0$, (r) $4p_{+1}$, (s) $5s$, (t) $4d_{-2}$, (u) $4d_{-1}$, (v) $4d_0$, (w) $4d_{+1}$, and (x) $4d_{-2}$.

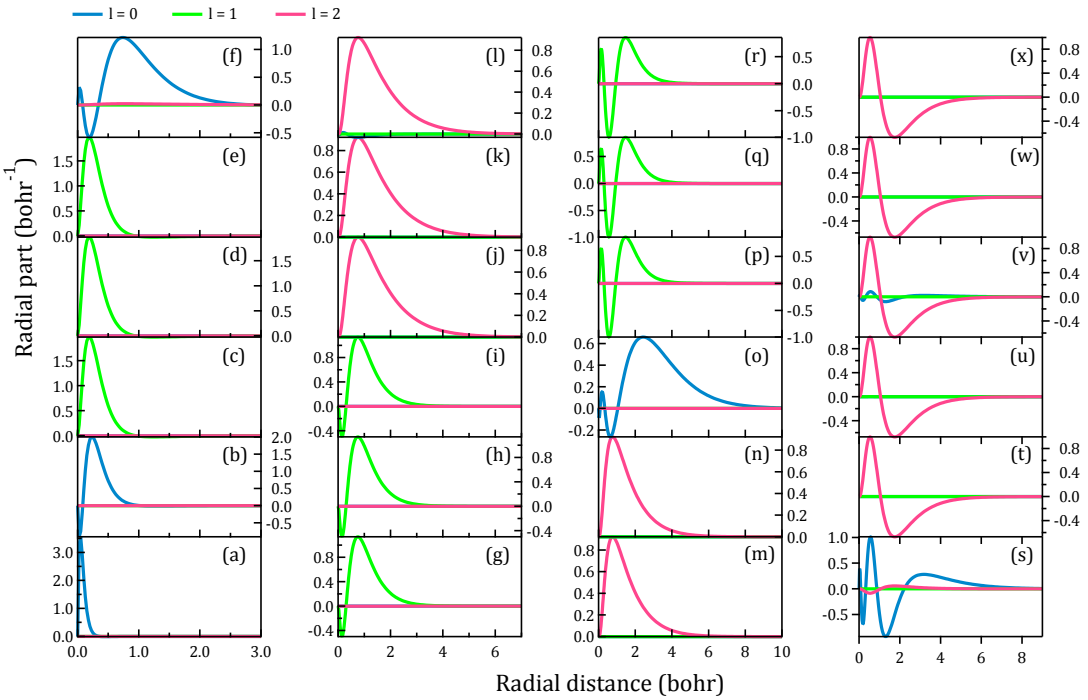

Figure C.2: Radial functions $U_l^\mu(r)$ of each Mn^+ ground state orbitals obtained using orbital subspace decomposition in Fig. 4.1(e) for μ = (a) $1s$, (b) $2s$, (c) $2p_{-1}$, (d) $2p_0$, (e) $2p_{+1}$, (f) $3s$, (g) $3p_{-1}$, (h) $3p_0$, (i) $3p_{+1}$, (j) $3d_{-2}$, (k) $3d_{-1}$, (l) $3d_0$, (m) $3d_{+1}$, (n) $3d_{+2}$, (o) $4s$, (p) $4p_{-1}$, (q) $4p_0$, (r) $4p_{+1}$, (s) $5s$, (t) $4d_{-2}$, (u) $4d_{-1}$, (v) $4d_0$, (w) $4d_{+1}$, and (x) $4d_{-2}$.

Bibliography

[1] D. Strickland and G. Mourou, "Compression of amplified chirped optical pulses", Opt. Commun. **56**, 219 (1985).

[2] P. Maine, D. Strickland, P. Bado, M. Pessot, and G. Mourou, "Generation of ultrahigh peak power pulses by chirped pulse amplification", IEEE J. Quantum Elect. **24**, 398 (1988).

[3] M. D. Perry and G. Mourou, "Terawatt to Petawatt Subpicosecond Lasers", Science **264**, 917 (1994).

[4] G. Mourou, "The Exawatt laser: from relativistic to ultra relativistic optics", in 2007 European Conference on Lasers and Electro-Optics and the International Quantum Electronics Conference (June 2007), pp. 1–2.

[5] T. Tajima, B. C. Barish, C. P. Barty, S. Bulanov, P. Chen, J. Feldhaus, J. Hajdu, C. H. Keitel, J. Kieffer, D. Ko, W. Leemans, D. Normand, L. Palumbo, K. Rzazewski, A. Sergeev, Z. Sheng, F. Takasaki, and M. Teshima, "Science of Extreme Light Infrastructure", AIP Conf. Proc. **1228**, 11 (2010).

[6] T. Tajima, D. Habs, and G. A. Mourou, "Highest intensities, shortest pulses", Optik & Photonik **5**, 24 (2010).

[7] G. A. Mourou, G. Korn, W. Sandner, and J. L. Collier, "ELI-Extreme Light Infrastructure: Science and Technology with Ultra-Intense Lasers, Whitebook", THOSS Media GmbH (2011).

[8] "Extreme light", Nat. Mater. **15**, 1 EP (2015).

[9] P. Agostini and L. F. DiMauro, "The physics of attosecond light pulses", Rep. Prog. Phys. **67**, 1563 (2004).

[10] F. Krausz and M. Ivanov, "Attosecond physics", Rev. Mod. Phys. **81**, 163 (2009).

[11] M. Protopapas, C. H. Keitel, and P. L. Knight, "Atomic physics with super-high intensity lasers", Rep. Prog. Phys. **60**, 389 (1997).

[12] E. Takahashi, Y. Nabekawa, T. Otsuka, M. Obara, and K. Midorikawa, "Generation of highly coherent submicrojoule soft x rays by high-order harmonics", Phys. Rev. A **66**, 021802 (2002).

[13] E. Takahashi, Y. Nabekawa, and K. Midorikawa, "Generation of 10μJ coherent extreme-ultraviolet light by use of high-order harmonics", Opt. Lett. **27**, 1920 (2002).

[14] P. Rudawski, C. M. Heyl, F. Brizuela, J. Schwenke, A. Persson, E. Mansten, R. Rakowski, L. Rading, F. Campi, B. Kim, P. Johnsson, and A. L'Huillier, "A high-flux high-order harmonic source", Rev. Sci. Instrum. **84**, 073103 (2013).

[15] W. Boutu, M. Ducousso, J. Hergott, and H. Merdji, in *Optical Technologies for Extreme-Ultraviolet and Soft X-ray Coherent Sources*, edited by F. Canova and L. Poletto (Springer, Berlin, 2015), p. 63.

[16] A. McPherson, G. Gibson, H. Jara, U. Johann, T. S. Luk, I. A. McIntyre, K. Boyer, and C. K. Rhodes, "Studies of multiphoton production of vacuum-ultraviolet radiation in the rare gases", J. Opt. Soc. Am. B **4**, 595 (1987).

[17] A. Shiner, C. Trallero-Herrero, N. Kajumba, B. Schmidt, J. Bertrand, K. T. Kim, H.-C. Bandulet, D. Comtois, J.-C. Kieffer, D. Rayner, P. Corkum, F. Légaré, and D. Villeneuve, "High harmonic cutoff energy scaling and laser intensity measurement with a 1.8 μm laser source", J. Mod. Optic. **60**, 1458 (2013).

[18] B. Shan and Z. Chang, "Dramatic extension of the high-order harmonic cutoff by using a long-wavelength driving field", Phys. Rev. A **65**, 011804 (2001).

[19] M. V. Frolov, N. L. Manakov, and A. F. Starace, "Wavelength Scaling of High-Harmonic Yield: Threshold Phenomena and Bound State Symmetry Dependence", Phys. Rev. Lett. **100**, 173001 (2008).

[20] A. D. Shiner, C. Trallero-Herrero, N. Kajumba, H.-C. Bandulet, D. Comtois, F. Légaré, M. Giguère, J.-C. Kieffer, P. B. Corkum, and D. M. Villeneuve, "Wavelength Scaling of High Harmonic Generation Efficiency", Phys. Rev. Lett. **103**, 073902 (2009).

[21] J. Tate, T. Auguste, H. G. Muller, P. Salières, P. Agostini, and L. F. DiMauro, "Scaling of Wave-Packet Dynamics in an Intense Midinfrared Field", Phys. Rev. Lett. **98**, 013901 (2007).

[22] K. Schiessl, K. L. Ishikawa, E. Persson, and J. Burgdörfer, "Quantum Path Interference in the Wavelength Dependence of High-Harmonic Generation", Phys. Rev. Lett. **99**, 253903 (2007).

[23] M. Lewenstein, P. Balcou, M. Y. Ivanov, A. L'Huillier, and P. B. Corkum, "Theory of high-harmonic generation by low-frequency laser fields", Phys. Rev. A **49**, 2117 (1994).

[24] K. L. Ishikawa, E. J. Takahashi, and K. Midorikawa, "Wavelength dependence of high-order harmonic generation with independently controlled ionization and ponderomotive energy", Phys. Rev. A **80**, 011807 (2009).

[25] K. Ba Dinh, P. Hannaford, and L. Van Dao, "Intensity dependent spectral features in high harmonic generation", J. Appl. Phys. **113**, 063102 (2013).

[26] P. B. Corkum, "Plasma perspective on strong field multiphoton ionization", Phys. Rev. Lett. **71**, 1994 (1993).

[27] K. C. Kulander, K. J. Schafer, and J. L. Krause, in *Super-Intense Laser-Atom Physics*, edited by A. L'Huillier, B. Piraux, and K. Rzazewski (Springer, New York, 1993), p. 95.

[28] K. J. Schafer, B. Yang, L. F. DiMauro, and K. C. Kulander, "Above threshold ionization beyond the high harmonic cutoff", Phys. Rev. Lett. **70**, 1599 (1993).

[29] O. Smirnova and M. Ivanov, in *Attosecond and XUV Physics: Ultrafast Dynamics and Spectroscopy*, edited by T. Schultz and M. Vrakking (Wiley-VCH, Weinheim, 2013).

[30] D. Baykusheva, S. Brennecke, M. Lein, and H. J. Wörner, "Signatures of Electronic Structure in Bicircular High-Harmonic Spectroscopy", Phys. Rev. Lett. **119**, 203201 (2017).

[31] M. F. Ciappina, J. A. Pérez-Hernández, A. S. Landsman, T. Zimmermann, M. Lewenstein, L. Roso, and F. Krausz, "Carrier-Wave Rabi-Flopping Signatures in High-Order Harmonic Generation for Alkali Atoms", Phys. Rev. Lett. **114**, 143902 (2015).

[32] L. Gui-Hua, X. Hong-Qiang, Y. Jin-Ping, C. Wei, C. Ya, L. Xiao-Jun, C. Jing, and X. Xin-Hua, "Signature of multi-channel interference in high-order harmonic generation from N_2 driven by intense mid-infrared pulses", Acta Phys. Sin-Ch. Ed. **65**, 224208, 224208 (2016).

[33] M. C. H. Wong, A.-T. Le, A. F. Alharbi, A. E. Boguslavskiy, R. R. Lucchese, J.-P. Brichta, C. D. Lin, and V. R. Bhardwaj, "High Harmonic Spectroscopy of the Cooper Minimum in Molecules", Phys. Rev. Lett. **110**, 033006 (2013).

[34] T. D. Scarborough, T. T. Gorman, F. Mauger, P. Sándor, S. Khatri, M. B. Gaarde, K. J. Schafer, P. Agostini, and L. F. DiMauro, "Full Characterization of a Molecular Cooper Minimum Using High-Harmonic Spectroscopy", Appl. Sci. **8** (2018).

[35] R. A. Ganeev, M. Suzuki, M. Baba, H. Kuroda, and T. Ozaki, "Strong resonance enhancement of a single harmonic generated in the extreme ultraviolet range", Opt. Lett. **31**, 1699 (2006).

[36] M. Suzuki, M. Baba, R. Ganeev, H. Kuroda, and T. Ozaki, "Anomalous enhancement of a single high-order harmonic by using a laser-ablation tin plume at 47 nm", Opt. Lett. **31**, 3306 (2006).

[37] R. A. Ganeev, L. B. E. Bom, J.-C. Kieffer, and T. Ozaki, "Systematic investigation of resonance-induced single-harmonic enhancement in the extreme-ultraviolet range", Phys. Rev. A **75**, 063806 (2007).

[38] R. A. Ganeev, T. Witting, C. Hutchison, F. Frank, M. Tudorovskaya, M. Lein, W. A. Okell, A. Zaïr, J. P. Marangos, and J. W. G. Tisch, "Isolated sub-fs XUV pulse generation in Mn plasma ablation", Opt. Express **20**, 25239 (2012).

[39] R. A. Ganeev, P. A. Naik, H. Singhal, J. A. Chakera, and P. D. Gupta, "Strong enhancement and extinction of single harmonic intensity in the mid- and end-plateau regions of the high harmonics generated in weakly excited laser plasmas", Opt. Lett. **32**, 65 (2007).

[40] R. A. Ganeev, J. A. Chakera, P. A. Naik, H. Singhal, R. A. Khan, and P. D. Gupta, "Resonance enhancement of single even harmonic of laser radiation in tin-containing plasma using intensity variation of two-color pump", J. Opt. Soc. Am. B **28**, 1055 (2011).

[41] R. A. Ganeev, V. V. Strelkov, C. Hutchison, A. Zair, D. Kilbane, M. A. Khokhlova, and J. P. Marangos, "Experimental and theoretical studies of two-color-pump resonance-induced enhancement of odd and even harmonics from a tin plasma", Phys. Rev. A **85**, 023832 (2012).

[42] A. Shiner, B. Schmidt, C. Trallero-Herrero, H. J. Wörner, S. Patchkovskii, P. B. Corkum, J. Kieffer, F. Légaré, and D. Villeneuve, "Probing collective multi-electron dynamics in xenon with high-harmonic spectroscopy", Nat. Phys. **7**, 464 (2011).

[43] J. T. Costello, J.-P. Mosnier, E. T. Kennedy, P. K. Carroll, and G. O'Sullivan, "X-UV Absorption Spectroscopy with Laser-Produced Plasmas: A Review", Phys. Scripta **T34**, 77 (1991).

[44] S. Haessler, V. Strelkov, L. B. E. Bom, M. Khokhlova, O. Gobert, J.-F. Hergott, F. Lepetit, M. Perdrix, T. Ozaki, and P. Salières, "Phase distortions of attosecond pulses produced by resonance-enhanced high harmonic generation", New J. Phys. **15**, 013051 (2013).

[45] A. L'Huillier, M. Lewenstein, P. Salières, P. Balcou, M. Y. Ivanov, J. Larsson, and C. G. Wahlström, "High-order Harmonic-generation cutoff", Phys. Rev. A **48**, R3433 (1993).

[46] O. Smirnova, Y. Mairesse, S. Patchkovskii, N. Dudovich, D. Villeneuve, P. Corkum, and M. Y. Ivanov, "High harmonic interferometry of multi-electron dynamics in molecules", Nature **460**, 972 (2009).

[47] D. B. Milošević, "High-energy stimulated emission from plasma ablation pumped by resonant high-order harmonic generation", J. Phys. B **40**, 3367 (2007).

[48] D. B. Milošević, "Theoretical analysis of high-order harmonic generation from a coherent superposition of states", J. Opt. Soc. Am. B **23**, 308 (2006).

[49] V. V. Strelkov, M. A. Khokhlova, and N. Y. Shubin, "High-order harmonic generation and Fano resonances", Phys. Rev. A **89**, 053833 (2014).

[50] M. Tudorovskaya and M. Lein, "High-order harmonic generation in the presence of a resonance", Phys. Rev. A **84**, 013430 (2011).

[51] M. V. Frolov, N. L. Manakov, and A. F. Starace, "Potential barrier effects in high-order harmonic generation by transition-metal ions", Phys. Rev. A **82**, 023424 (2010).

[52] V. Strelkov, "Role of Autoionizing State in Resonant High-Order Harmonic Generation and Attosecond Pulse Production", Phys. Rev. Lett. **104**, 123901 (2010).

[53] I. A. Ivanov and A. S. Kheifets, "Resonant enhancement of generation of harmonics", Phys. Rev. A **78**, 053406 (2008).

[54] C. F. de Morisson Faria, R. Kopold, W. Becker, and J. M. Rost, "Resonant enhancements of high-order harmonic generation", Phys. Rev. A **65**, 023404 (2002).

[55] P. V. Redkin and R. A. Ganeev, "Simulation of resonant high-order harmonic generation in a three-dimensional fullerenelike system by means of a multiconfigurational time-dependent Hartree-Fock approach", Phys. Rev. A **81**, 063825 (2010).

[56] S. Pabst and R. Santra, "Strong-Field Many-Body Physics and the Giant Enhancement in the High-Harmonic Spectrum of Xenon", Phys. Rev. Lett. **111**, 233005 (2013).

[57] H.-D. Meyer, U. Manthe, and L. Cederbaum, "The multi-configurational time-dependent Hartree approach", Chem. Phys. Lett. **165**, 73 (1990).

[58] M. Beck, A. Jäckle, G. Worth, and H.-D. Meyer, "The multiconfiguration time-dependent Hartree (MCTDH) method: a highly efficient algorithm for propagating wavepackets", Phys. Rep. **324**, 1 (2000).

[59] L. Greenman, P. J. Ho, S. Pabst, E. Kamarchik, D. A. Mazziotti, and R. Santra, "Implementation of the time-dependent configuration-interaction singles method for atomic strong-field processes", Phys. Rev. A **82**, 023406 (2010).

[60] J. Zanghellini, M. Kitzler, C. Fabian, T. Brabec, and A. Scrinzi, "An MCTDHF Approach to Multielectron Dynamics in Laser Fields", Laser Phys. **13**, 1064 (2002).

[61] T. Kato and H. Kono, "Time-dependent multiconfiguration theory for electronic dynamics of molecules in an intense laser field", Chem. Phys. Lett. **392**, 533 (2004).

[62] J. Caillat, J. Zanghellini, M. Kitzler, O. Koch, W. Kreuzer, and A. Scrinzi, "Correlated multielectron systems in strong laser fields: A multiconfiguration time-dependent Hartree-Fock approach", Phys. Rev. A **71**, 012712 (2005).

[63] T. Sato and K. L. Ishikawa, "Time-dependent complete-active-space self-consistent-field method for multielectron dynamics in intense laser fields", Phys. Rev. A **88**, 023402 (2013).

[64] T. Sato, K. L. Ishikawa, I. B řezinová, F. Lackner, S. Nagele, and J. Burgdörfer, "Time-dependent complete-active-space self-consistent-field method for atoms: Application to high-order harmonic generation", Phys. Rev. A **94**, 023405 (2016).

[65] T. Sato and K. L. Ishikawa, "Time-dependent multiconfiguration self-consistent-field method based on the occupation-restricted multiple-active-space model for multielectron dynamics in intense laser fields", Phys. Rev. A **91**, 023417 (2015).

[66] H. Miyagi and L. B. Madsen, "Time-dependent restricted-active-space self-consistent-field theory for laser-driven many-electron dynamics", Phys. Rev. A **87**, 062511 (2013).

[67] I. Tikhomirov, T. Sato, and K. L. Ishikawa, "High-Harmonic Generation Enhanced by Dynamical Electron Correlation", Phys. Rev. Lett. **118**, 203202 (2017).

[68] Y. Li, T. Sato, and K. L. Ishikawa, "High-order harmonic generation enhanced by laser-induced electron recollision", Phys. Rev. A **99**, 043401 (2019).

[69] I. S. Wahyutama, T. Sato, and K. L. Ishikawa, "Time-dependent multiconfiguration self-consistent-field study on resonantly enhanced high-order harmonic generation from transition-metal elements", Phys. Rev. A **99**, 063420 (2019).

[70] M. Fareed, V. Strelkov, N. Thiré, S. Mondal, B. Schmidt, F. Légaré, and T. Ozaki, "High-order harmonic generation from the dressed autoionizing states", Nat. Commun. **8**, 16061 (2017).

[71] D. B. Milošević, "Resonant high-order harmonic generation from plasma ablation: Laser intensity dependence of the harmonic intensity and phase", Phys. Rev. A **81**, 023802 (2010).

[72] D. B. Milošević and W. Becker, "Role of long quantum orbits in high-order harmonic generation", Phys. Rev. A **66**, 063417 (2002).

[73] P. Salières, B. Carré, L. Le Déroff, F. Grasbon, G. G. Paulus, H. Walther, R. Kopold, W. Becker, D. B. Milošević, A. Sanpera, and M. Lewenstein, "Feynman's Path-Integral Approach for Intense-Laser-Atom Interactions", Science **292**, 902 (2001).

[74] D. B. Milošević, D. Bauer, and W. Becker, "Quantum-orbit theory of high-order atomic processes in intense laser fields", J. Mod. Optic. **53**, 125 (2006).

[75] M. Feit, J. Fleck, and A. Steiger, "Solution of the Schrödinger equation by a spectral method", J. Comput. Phys. **47**, 412 (1982).

[76] J. A. Fleck, J. R. Morris, and M. D. Feit, "Time-dependent propagation of high energy laser beams through the atmosphere", Appl. Phys. **10**, 129 (1976).

[77] C. C. Chiril ă, I. Dreissigacker, E. V. van der Zwan, and M. Lein, "Emission times in high-order harmonic generation", Phys. Rev. A **81**, 033412 (2010).

[78] M. V. Frolov, N. L. Manakov, T. S. Sarantseva, M. Y. Emelin, M. Y. Ryabikin, and A. F. Starace, "Analytic Description of the High-Energy Plateau in Harmonic Generation by Atoms: Can the Harmonic Power Increase with Increasing Laser Wavelengths?", Phys. Rev. Lett. **102**, 243901 (2009).

[79] H. Kjeldsen, "Photoionization cross section data", (unpublished).

[80] R. A. Ganeev, M. Suzuki, M. Baba, and H. Kuroda, "High-order harmonic generation from laser plasma produced by pulses of different duration", Phys. Rev. A **76**, 023805 (2007).

[81] D. Nikolić, T. W. Gorczyca, and N. R. Badnell, "Resonance asymmetry and external field effects in the photorecombination of Ti^{4+}", Phys. Rev. A **79**, 012703 (2009).

[82] D. Nikolić, T. W. Gorczyca, and N. R. Badnell, "Quantifying the strength and asymmetry of giant resonances in the photorecombination of Sc^{3+} and the photoionization of Sc^{2+}", Phys. Rev. A **81**, 030501 (2010).

[83] D. J. Griffiths and D. F. Schroeter, *Introduction to Quantum Mechanics*, 3rd ed. (Cambridge University Press, 2018).

[84] K. L. Ishikawa and T. Sato, "A Review on Ab Initio Approaches for Multielectron Dynamics", IEEE J. Sel. Top. Quant. **21**, 1 (2015).

[85] T. Helgaker, P. Jorgensen, and J. Olsen, *Molecular electronic-structure theory* (John Wiley & Sons, 2014).

[86] P.-G. Reinhard, "A comment on time-dependent variational-principles", Z. Phys. A **280**, 281 (1977).

[87] P.-O. Löwdin and P. Mukherjee, "Some comments on the time-dependent variation principle", Chem. Phys. Lett. **14**, 1 (1972).

[88] R. Moccia, "Time-dependent variational principle", Int. J. Quantum Chem. **7**, 779 (1973).

[89] E. J. Heller, "Time dependent variational approach to semiclassical dynamics", J. Chem. Phys. **64**, 63 (1976).

[90] R. Weinstock, *Calculus of Variations with Applications to Physics and Engineering* (Dover Publications, 1974).

[91] A. Szabo and N. Ostlund, *Modern Quantum Chemistry: Introduction to Advanced Electronic Structure Theory*, Dover Books on Chemistry (Dover Publications, 1996).

[92] K. Ruedenberg, M. W. Schmidt, M. M. Gilbert, and S. Elbert, "Are atoms intrinsic to molecular electronic wavefunctions? I. The FORS model", Chem. Phys. **71**, 41 (1982).

[93] B. O. Roos, P. R. Taylor, and P. E. Siegbahn, "A complete active space SCF method (CASSCF) using a density matrix formulated super-CI approach", Chem. Phys. **48**, 157 (1980).

[94] B. O. Roos, "The Complete Active Space Self-Consistent Field Method and its Applications in Electronic Structure Calculations", in *Advances in Chemical Physics* (John Wiley & Sons, Ltd, 2007), pp. 399–445.

[95] M. W. Schmidt and M. S. Gordon, "The Construction and Interpretation of MCSCF Wavefunctions", Annu. Rev. Phys. Chem. **49**, 233 (1998).

[96] J. Ivanic, "Direct configuration interaction and multiconfigurational self-consistent-field method for multiple active spaces with variable occupations. I. Method", J. Chem. Phys. **119**, 9364 (2003).

[97] J. Ivanic, "Direct configuration interaction and multiconfigurational self-consistent-field method for multiple active spaces with variable occupations. II. Application to oxoMn(salen) and N2O4", J. Chem. Phys. **119**, 9377 (2003).

[98] T. N. Rescigno and C. W. McCurdy, "Numerical grid methods for quantum-mechanical scattering problems", Phys. Rev. A **62**, 032706 (2000).

[99] B. I. Schneider, L. A. Collins, and S. X. Hu, "Parallel solver for the time-dependent linear and nonlinear Schrödinger equation", Phys. Rev. E **73**, 036708 (2006).

[100] C. W. McCurdy, M. Baertschy, and T. N. Rescigno, "Solving the three-body Coulomb breakup problem using exterior complex scaling", J. Phys. B **37**, R137 (2004).

[101] B. I. Schneider, J. Feist, S. Nagele, R. Pazourek, S. X. Hu, L. A. Collins, and J. Burgdörfer, in *Quantum Dynamic Imaging*, edited by A. D. Bandrauk and M. Ivanov (Springer, New York, 2011), p. 149.

[102] J. Shen, T. Tang, and L.-L. Wang, *Spectral methods: algorithms, analysis and applications*, Vol. 41 (Springer Science & Business Media, 2011).

[103] C. Corliss and J. Sugar, "Energy levels of manganese, Mn I through Mn XXV", J. Phys. Chem. Ref. Data **6**, 1253 (1977).

[104] Y. Orimo, T. Sato, A. Scrinzi, and K. L. Ishikawa, "Implementation of the infinite-range exterior complex scaling to the time-dependent complete-active-space self-consistent-field method", Phys. Rev. A **97**, 023423 (2018).

[105] A. Scrinzi, "Infinite-range exterior complex scaling as a perfect absorber in time-dependent problems", Phys. Rev. A **81**, 053845 (2010).

[106] J. W. Cooper, C. W. Clark, C. R. Cromer, T. B. Lucatorto, B. F. Sonntag, E. T. Kennedy, and J. T. Costello, "Marked differences in the 3p photoabsorption between the Cr and Mn^+ isoelectronic pair: Reasons for the unique structure observed in Cr", Phys. Rev. A **39**, 6074 (1989).

[107] P. M. Abanador, F. Mauger, K. Lopata, M. B. Gaarde, and K. J. Schafer, "Wavelength and intensity dependence of recollision-enhanced multielectron effects in high-order harmonic generation", Phys. Rev. A **97**, 043414 (2018).

[108] D. R. Lide, *CRC handbook of chemistry and physics*, 85th ed. (CRC press, 2004).

[109] J. E. Sansonetti and W. C. Martin, "Handbook of Basic Atomic Spectroscopic Data", J. Phys. Chem. Ref. Data **34**, 1559 (2005).

[110] K. S. Bhatia, "Spectrum of doubly ionised indium", J. Phys B **11**, 2421 (1978).

[111] P. Koval, F. Wilken, D. Bauer, and C. H. Keitel, "Nonsequential Double Recombination in Intense Laser Fields", Phys. Rev. Lett. **98**, 043904 (2007).

Acknowledgement

All praise is due to God alone, the Lord of mankind who set the universe in its entirety, from the most enormous to the most subtle of all existence, in motion. The exalted is He, the originator of all causes and the establisher of all laws of nature, a tiny bit of which this worldy endeavor, with all the might, is trying to uncover. The successful achievement of this doctoral degree is but a favor and mercy of God to His powerless creation. Indeed, it is He the sole provider and sustainer of all the dwellers in heaven and on earth.

As all-encompassing as God is, He established the affairs of every single one of His creations to be contingent on the other ones, and in this regard the one person to whom I sincerely feel indebted above all for the successful completion of this pivotal stage in my life would be my supervisor at the University of Tokyo, Prof. Kenichi Ishikawa. It is, at the very beginning, thanks to Prof. Ishikawa's willingness to accept me and acknowledge my potential to conduct doctoral research in his lab. It is probably also due to him that I was granted the University of Tokyo Fellowship, the most prestigious scholarship for international students at this university, at the time of enrollment to my PhD, without which an Indonesian national like me would find it very difficult to afford the high living cost in Tokyo. Always striving to maintain high quality research outputs in all forms but also cares about the general state of affairs of his employees, he is definitely someone to look up to if someone were to aim for an academic decency.

The first few weeks of my life in Tokyo would not be that comfortable without the help from Mr. Takumi Nameki, a master student at Ishikawa and Sato lab assigned to assist me with my integration in Tokyo. The lab secretary, Mrs. Yumi Kumaoka, has helped me too many times on many things administration and logistic-related, from handling travel reimbursement to printing conference posters.

I did a good first year of my PhD as a research trainee at RIKEN Wako, Saitama. The generosity of Dr. Katsumi Midorikawa, the head of the group where I was at RIKEN, allowed me to gain first hand experimental knowledge and experience in ultrafast and attosecond science under direct supervision of Dr. Tomoya Okino and Dr. Yasuo Nabekawa. Although it effectively lasted for about nine months, I learned a lot about a detection technique using velocity map imaging machine and about how one can study the dynamic of dissociative ionization using this technique. Among the tasks assigned to me, the unforgettable one was when I had to reproduce kinetic energy release map of a recoilling H^+ ion in one of their published papers. It is such a precious experience because it gave me opportunity to gain confidence in developing a theoretical model to describe experimental data and to apply my learned Fortran language fundamentals for a not-so-small programming project, an experience that proved useful for my research ventures that awaited me when I transferred back to the lab at Todai Hongo campus.

Following the end of my status as a RIKEN trainee, I was assigned the task to carry out a theoretical study on resonant high-harmonic generation at Ishikawa and Sato lab using TD-CASSCF and TD-ORMAS, the two *ab initio* methods which have been developed in this lab. For this, my big thanks goes to no one other than Prof. Takeshi Sato, an expert in *ab initio* methods, has a very helpful personality and is always ready to lend a hand when problems surfaced, I cannot ask for more. Thanks to his guidance in using his program such that I managed to lead a smooth start in this new project. Never have the discussions with him been unfruitful, either it rectified my understanding of the problem in question or it inspired me to come up with new ideas. He taught me the concept of the program's source code which eventually allowed me to tweak the

codes here and there on my own, something that gave birth to the calculation of transition and orbital occupation analyses.

Two desks away from me in the lab room is Dr. Himadri Pathak. He is knowledgeable not only in his field of expertise but also in many common aspects of life, which makes him a perfect conversation partner in breaks or when my mind just want a momentary escape from research activities. I am also thankful to him for introducing me to Indian cuisine at that all-you-can-eat restaurant. As a matter of fact, at the time of this writing I still find it difficult to repay that particular favor of his as I have yet to find any Indonesian restaurant where I can have remotely close gustatory pleasure as I did in that restaurant he invited me to. There is also Dr. Yang Li, another postdoc, with whom I enjoyed talking, in particular about the interesting and surprising facts about his country. Mr. Ryoji Anzaki, a PhD fellow, has helped me on many things too. Well-versed in theoretical phsyics and also well-informed about various sides of Japanese culture and history, he is a fun guy to talk to. Naturally, I am also grateful for the help and contribution in any forms from the other lab members and for support from Special Graduate Program in Resilience Engineering for the completion of this PhD research.

Dr. Margarita Khokhlova, a visiting postdoc from Imperial College of London, came over to Ishikawa and Sato lab about a month toward my final defense and surprisingly also used to do research under the same topic as me, resonant high-harmonic generation. Although our meeting is regrettably brief, I am thankful for her inputs on my work and her sharing of experience about this research field.

Inasmuch as PhD life can be very demanding and dangerously desolating, as a coping mechanism I therefore take photography as a hobby and in this regard, I would like to thank all people who have been in the frame of my shots. In particular, I would like to offer my thanks to whoever urban planners and architects who contributed to make the city of Tokyo so full of engaging street and urban scenes, to the point where I (and probably other street and urban photographers) would consider Tokyo as a jungle for street photographers. This city is such a wonderful and comfy dwelling place definitely worth of a second visit.

Last but not least, I am truly grateful to family back home for their support, especially at times of distress. My parents often times gave me advice on how to approach common life matters and as for my little brother, whom I never stop cherishing, the occasionally withering research passion of mine is often rekindled just by looking at his playfulness and mischief. Overall, I enjoyed my time as a college student and as a human being in these past three years and truly, it was a memorable one. I want to thank again all of those mentioned above as well as those who are not for painting beautiful colors in my life in general.

August 2019
Imam S. Wahyutama